FABRICATION AND MATERIALS FOR MAGNETO-PHOTONIC ASSEMBLIES FOR HIGH-GAIN ANTENNA APPLICATIONS AT GHZ FREQUENCIES

DISSERTATION

Presented in Partial Fulfillment for the Requirements for
the Degree Doctor of Philosophy in the
Graduate School of The Ohio State University

By
Lanlin Zhang, M.S.

* * * * *

The Ohio State University
2008

Dissertation Committee:
Professor Hendrik Verweij, Adviser
Professor Morgan Y. Liu
Professor Nitin Padture
Professor John L. Volakis
Professor Wolfgang Windl

Approved by

Adviser

Graduate Program in
Materials Science and Engineering

ABSTRACT

Recent magnetic photonic assembly (MPA) designs for high-gain antennas contain arrays of low-loss, anisotropic dielectrics and ferrimagnetic materials. Anisotropic dielectrics (AD) are fabricated from laminates, which consist of two ceramics with largely different permittivity and low dielectric losses at GHz frequencies. High gain has been demonstrated in a prototype antenna with 2 sets of 3 mutually rotated AD layers. These layers were made from laminates of commercially available α-Al_2O_3 and Nd-doped barium titanate. Equivalent permittivity tensors and loss tangents (tan δ~1.9×10^{-3}) were characterized using a resonant cavity based approach, coupled with a finite-element method (FEM) full-wave solver. To enable further minimization of dielectric loss (tan δ), dense high-purity α-Al_2O_3 and TiO_2 were prepared starting from colloidally stabilizing the powders in aqueous HNO_3 or NH_3. After colloidal filtration and sintering, α-Al_2O_3 with >97.9% density was achieved at a sintering temperature of 1300ºC, and TiO_2 with >99.5% density was obtained at 1000ºC. These low sintering temperatures are ascribed to excellent compact homogeneity. TiO_2 was obtained with tan δ of 1.4×10^{-4} at 6.4 GHz at room temperature. This relatively low value is attributed to the homogeneous dense microstructure with 2.2 μm grain size. Al^{3+} was doped into TiO_2 using a modified infiltration method to compensate for the effect of Ti^{4+} reduction. A homogeneous microstructure and doping concentration were also observed in the doped dense TiO_2. Substituted $Y_3Fe_5O_{12}$ (YIG) garnet was chosen as the ferrimagnetic (F) component, due to its pronounced Faraday rotation effect and potentially low magnetic and dielectric loss. Phase pure garnet was prepared by using the citric-gel method. The magnetic properties were studied for Ca,V,Zr-substituted YIG (CVZG) and as-prepared particle morphology. Compacts of CVZG submicron particles were found to possess a low loss at GHz frequencies, and will be applied in future MPAs structures.

Dedicated to

My mother and father

ACKNOWLEDGMENTS

I am deeply grateful for so many people who have offered their guidance and support during my doctoral work.

First of all, my deepest acknowledgement goes to my advisor, Prof. Hendrik Verweij, for his commitment, patience and supervision. He encouraged me to develop independent research skills, analytic capabilities and writing skills, and also guided me through difficult times to pursuit my Ph.D. dream.

I would like to thank Prof. John L. Volakis in ElectroScience Laboratory, OSU, for giving me such a wonderful cooperation opportunity to explore this novel and challenging research project. Many thanks to Dr. Kubilay Sertel, Gokhan Mumcu and Salih Yarga in ElectroScience Laboratory for their help on measurement of dielectric and magnetic properties.

I am grateful for all the group members past and present, especially Krenar Shqau, Jingyu Shi, Di Yu, Matthew Mottern, Frank Zalar, Matthew O'Malley, Elvin Beach, Melissa Schillo and William Chiu, for contributing to a stimulating academic environment and creating a cozy home-away-from-home for me.

My gratitude also goes to the U.S. Air Force Office of Scientific Research and the Ohio State University Office of Research Large Interdisciplinary Grant Program, for their generous financial support, without which this work could not have been performed.

Lastly, I would like to thank my dearest mother and father, who have always been by my side, loving me and raising me up to more than I can be.

VITA

October 14, 1981.....Born - Nanjing, P.R. China

2003.....B.S., Materials Science,

.....Fudan University, Shanghai, China.

2007.....M.S., Materials Science and Engineering,

.....The Ohio State University, Columbus, OH.

2003 – Present.....Graduate research assistant,

.....The Ohio State University, Columbus, OH.

PUBLICATIONS

1. L. Zhang, K. Sertel and H. Verweij, "Calcium, vanadium, zirconium-substituted yttrium iron garnet for microwave applications", in preparation.

2. L. Zhang, and H. Verweij, "Homogeneous Al doping in titanium dioxide using gel-assisted infiltration," in preparation.

3. L. Zhang, K. Shqau, G. Mumcu, K. Sertel, J.L. Volakis, and H. Verweij, "Viable route for dense TiO_2 with low microwave dielectric loss," *J. Am. Ceram. Soc.*, submitted.

4. L. Zhang, K. Shqau, G. Mumcu, K. Sertel, J.L. Volakis and H. Verweij, "Preparation of low-loss titanium dioxide for microwave frequency applications," *Proc. MS&T*, Pittsburgh, PA, October 2008.

5. L. Zhang, G. Mumcu, S. Yarga, K. Sertel, J.L. Volakis, and H. Verweij, "Fabrication and characterization of anisotropic dielectrics for low-loss microwave applications," *J. Mater. Sci.*, **43** [5] 1505-1509 (2008).

6. L. Zhang, G. Mumcu, K. Sertel, J.L. Volakis, and H. Verweij, "Fabrication of photonic assemblies for high-gain antennas," *Proc. MS&T*, Detroit, MI, September 2007.

7. L. Zhang and H. Verweij, "Ceramic processing for multi-material devices with complex geometry," *Proc. IEEE AP-S International Symposium*, Honolulu, HI, June 2007.

8. L. Zhang, G. Mumcu, K. Sertel, J.L. Volakis, and H. Verweij, "High-gain magnetic photonic assembly antennas for GHz frequencies," *Proc. TMS*, Orlando, FL, February 2007.

FIELDS OF STUDY

Major Field: Materials Science and Engineering

TABLE OF CONTENTS

Page

LIST OF TABLES

LIST OF FIGURES

LIST OF SYMBOLS

χ_e	Dielectric susceptibility.
χ_m	Magnetic susceptibility.
ε_0	Permittivity of free space.
ε_r	Relative permittivity (dielectric constant).
ε_r'	Real part of complex relative permittivity.
ε_r''	Imaginary part of complex relative permittivity.
ϕ_p	Porosity.
γ_g	Gyromagnetic ratio.
λ	Wavelength.
μ_0	Permeability of free space.
μ_B	Bohr magneton.
μ_r	Relative permeability.
μ_r'	Real part of complex relative permeability.
μ_r''	Imaginary part of complex relative permeability.
θ_F	Faraday rotation angle.
ρ_a	Apparent density.
ρ_r	Relative density.
ρ_t	Theoretical density.
ω	Angular frequency.
ζ	Zeta-potential.
$\varnothing_g$	Grain size.
$\varnothing_p$	Particle size.
AD	Anisotropic dielectrics.
BET	Brunauer-Emmett-Teller surface area measurement.
CA	Citric acid.
CVZG	Calcium vanadium zirconium garnet.
EG	Ethylene glycol.
EM	Electromagnetic (wave or energy).
F	Ferrimagnetic layers in MPA structures.
FEM	Finite element method.
FR	Faraday rotation.
MPA	Magnetic photonic assembly.
MW	Microwave.
PA	Photonic assembly.
SEM	Scanning electron microscopy.

tan δ	Dielectric loss tangent.
TEC	Thermal expansion coefficient.
TEM	Transmission electron microscopy.
XRD	X-ray diffraction.
YIG	$Y_3Fe_5O_{12}$ garnet.
YIP	$YFeO_3$ perovskite.
B	Magnetic induction.
D	Electric displacement vector.
E	Electrical field.
f	Frequency.
H	Magnetic field.
M	Magnetization.
M_s	Saturation magnetization.
P	Electric polarization.
Q	Dielectric quality factor.
T_C	Curie temperature.

CHAPTER 1

INTRODUCTION

Metamaterials and engineered artificial media hold the promise to enhance the antenna performance for microwave (MW) applications. Low loss dielectric and magnetic materials, in particular, are of great interest for wireless communication.

1.1 Materials in MW antenna applications

Microwaves are electromagnetic (EM) waves with frequencies (f) of 0.3-300 GHz, in which bands are assigned as listed in table 1.1. Antenna applications have been explored to realize high-gains of MW signals and miniaturization of devices. Dielectrics have been used in MW devices, such as resonators to enhance signals and filters to remove noise. There are three main requirements for application of dielectrics at MW frequencies [1-3]

- high permittivity (or dielectric constant, ε_r) to enable device minimization, since the wavelength inside the structure is $\propto (\varepsilon_r)^{-\frac{1}{2}}$,
- low dielectric loss tangent (tan δ) to minimize energy dissipation,
- temperature stability to avoid signal drift due to operation heat.

Magnetic materials have also been incorporated for their permeability properties and non-reciprocal interactions with MW signals [4-6]. Here we narrow magnetic materials down to ferrimagnetic oxides (or ferrites [6]), because ferrites, unlike ferromagnetic metals, are insulators and allow total penetration of MW. By changing chemical compositions and microstructures, the magnetic properties of ferrites can be tailored for specific applica-

tions, such as circulators and phase shifters. The general requirements for ferrites in MW applications include [7]

- low magnetic and dielectric loss to ensure the quality of MW signals,
- operation away from resonance to avoid dramatic energy loss,
- temperature stability to avoid signal drift due to operation heat.

Band	Frequency	Wavelength	Applications [8]
UHF	0.3-1 GHz	1.0-0.3 m	Military search radar, UHF broadcast TV, mobile radio
L	1-2 GHz	30.0-15.0 cm	Air traffic control transponder, space telemetry
S	2-4 GHz	15.0-7.5 cm	Troposcatter, microwave heating, airport search radar, microwave point-to-point relay
C	4-8 GHz	7.50-3.75 cm	Satellite communication downlink and uplink, studio transmitter link, microwave relay
X	8-12 GHz	3.75-2.50 cm	Airborne fire control radar
Ku	12-18 GHz	2.50-1.67 cm	Telephone relay
K	18-27 GHz	1.67-1.11 cm	Future satellite communication downlink, police radar
Ka	27-40 GHz	11.1-7.5 mm	Future satellite communication uplink
V	40-75 GHz	7.5-4.0 mm	-
W	75-110 GHz	4.0-2.7 mm	Missile seeker radar
mm	110-300 GHz	2.7-1.0 mm	-

Table 1.1: Microwave frequency band designations, after [9].

Recent investigations and simulations further explored innovative MW applications of dielectrics and ferrites, by combining these two components in optimized designs to maximize antenna gains. Two such examples are ground plane antennas in L-S band and

magnetic photonic assemblies (MPAs) in X band. MPAs are expected to dramatically enhance wireless communications, from personal cellular phones to space satellites. They utilize the frozen propagation modes in the periodic structures, to significantly increase field amplitudes within the structure [10-12]. The work described in this thesis has contributed to demonstrating an MPA design as shown in figure 1.1. It is consisted of 10-40 unit cells, each made of two anisotropic dielectric (AD) layers and one ferrimagnetic (F) layer [12]. This design is expected to provide a 5-fold increase of MW field amplitude at 10 GHz.

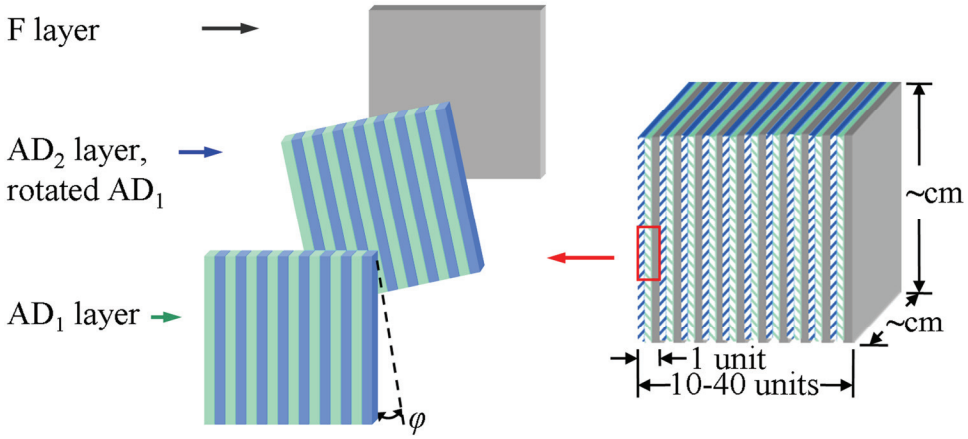

Figure 1.1: Application example: MPAs consisting of anisotropic dielectric and ferrimagnetic layers for high-gain antennas at GHz frequencies.

In addition to the general requirements, AD and F materials must satisfy the following design parameters to ensure high gains:

- in-plane dielectric anisotropy in AD layers >2,
- dielectric loss tangent (tan δ) of AD layers preferably $\leq 10^{-4}$,
- a relative rotation angle φ between AD_1 and AD_2 layers, depending on the actual anisotropy, to maximize the antenna gain,
- Faraday rotation (FR) [4-6] of ~10°/mm in F layers,
- low dielectric and low magnetic losses in F layers,

- lateral dimensions of AD and F layers in cm-scale dimensions.

1.2 State-of-art and approach

1.2.1 AD layers

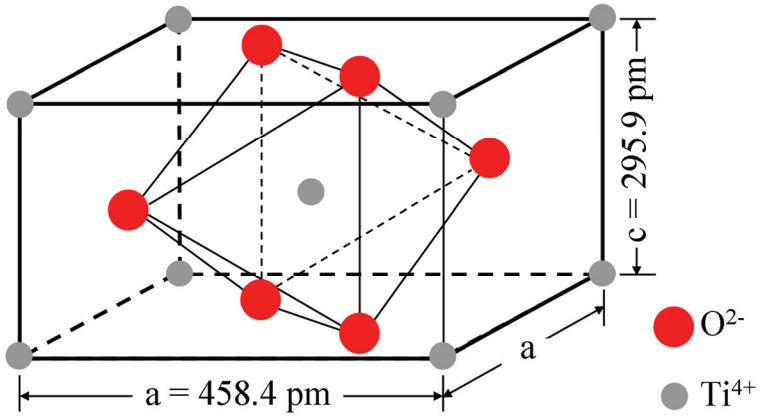

Figure 1.2: Crystal structure of TiO_2 (rutile), after [1].

Natural anisotropic dielectrics are available in mm or smaller dimensions, such as single crystal TiO_2 rutile as shown in figure 1.2. Its intrinsic anisotropy is described with relative permittivity (dielectric constant) $\varepsilon_{ra} = 85$ and $\varepsilon_{rc} = 165$ at GHz frequencies [13]. However its high cost prohibits practical use, especially in the required cm scales. This large lateral dimension is required so that the antenna aperture, presented to the incoming wave, is sufficient. On the other hand effective mean field AD materials can be made from epitaxial thin films, periodically grated substrates [14] and laminar structures [15,16]. Grating or epitaxial growth is not suitable because of long-time fabrication. AD laminates are hence preferred, for their flexibility in permittivity and dimensions, and relatively efficient fabrication. The anisotropy in AD laminates is achieved by laminating two dielectrics with largely differently relative permittivity ε_r, i.e. low ε_{rl} and high ε_{rh}. The effective permittivity is $\left(\varepsilon_{rl}^{-1} + \varepsilon_{rh}^{-1}\right)^{-1}$ parallel to the lamination direction, and

$\frac{(\varepsilon_{rl} + \varepsilon_{rh})}{2}$ perpendicular to the direction. Lamination is performed by using organic or inorganic, external or internal (reaction-formed) adhesives. The thin AD layers can be carefully machined, parallel to the laminating direction, from the AD laminates, as illustrated in figure 1.3.

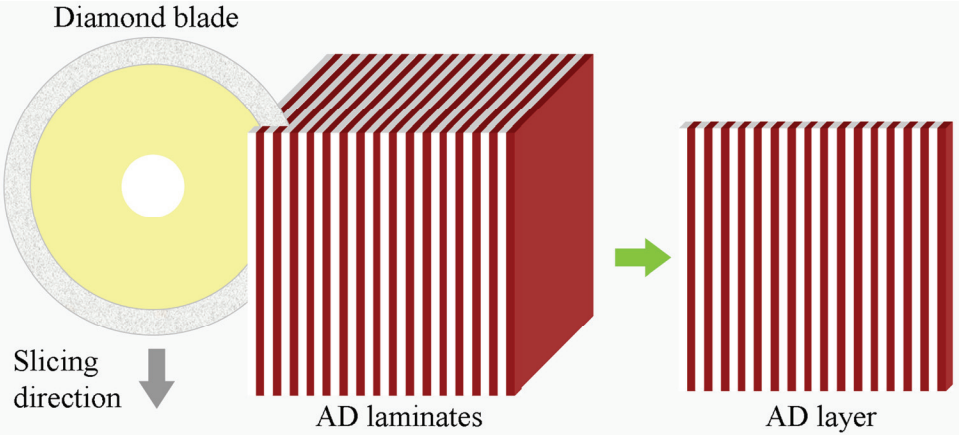

Figure 1.3: Illustration of fabricating one AD layer from laminates. The white and red colors represent two dielectrics with largely different ε_r.

It is easily seen that a higher $(\varepsilon_{rh} - \varepsilon_{rl})$ leads to a higher dielectric anisotropy. However, the selection of dielectrics with ε_{rl} and ε_{rh} is limited by the GHz application frequency and the required low loss. Dielectric loss (tan δ) is theoretically predicted and experimentally observed to increase proportionally with frequency (f) at MW frequencies. The dielectric quality factor Q is equal to $\frac{1}{\tan\delta}$; and for this reason, the product of ($Q \cdot f$) is used when comparing different dielectrics. In general, both Q and ($Q \cdot f$) decrease as ε_r increases, as indicated in figure 1.4 and 1.5. Therefore dielectrics with high ε_r are expected to have a higher loss than dielectrics with low ε_r, and eventually result in an overall high loss in AD laminates. To make sure that tan $\delta \leq 10^{-4}$, the ε_{rl} dielectric should be at the left-upper corner of figure 1.4, and the ε_{rh} at the right-upper corner. Al_2O_3 and TiO_2 were selected ac-

cordingly as the two components in AD laminates because of their favorable dielectric properties and simple chemical compositions. More specifically, it is α-Al_2O_3 and rutile TiO_2 that were used because they are the stable phases of these two compositions respectively. This choice has been confirmed by experimental data on polycrystalline α-Al_2O_3 ($\varepsilon_r = 10$, $\tan\delta = 2\times10^{-5}$ [17]) and polycrystalline rutile TiO_2 ($\varepsilon_r = 115$*, $\tan\delta = 6\times10^{-5}$ [18]).

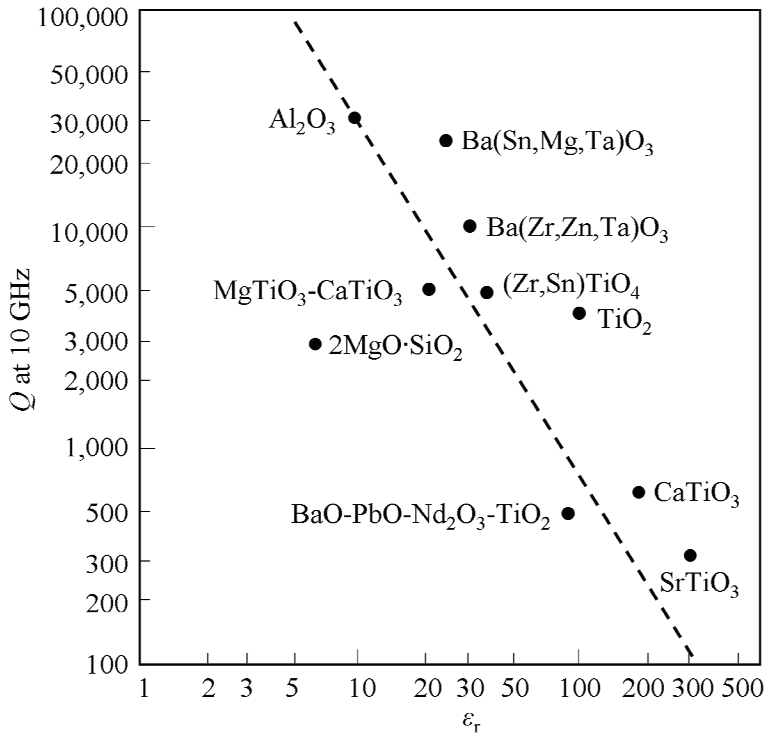

Figure 1.4: Relationship of ε_r vs Q for various dielectrics, after [19].

* Measured in this study.

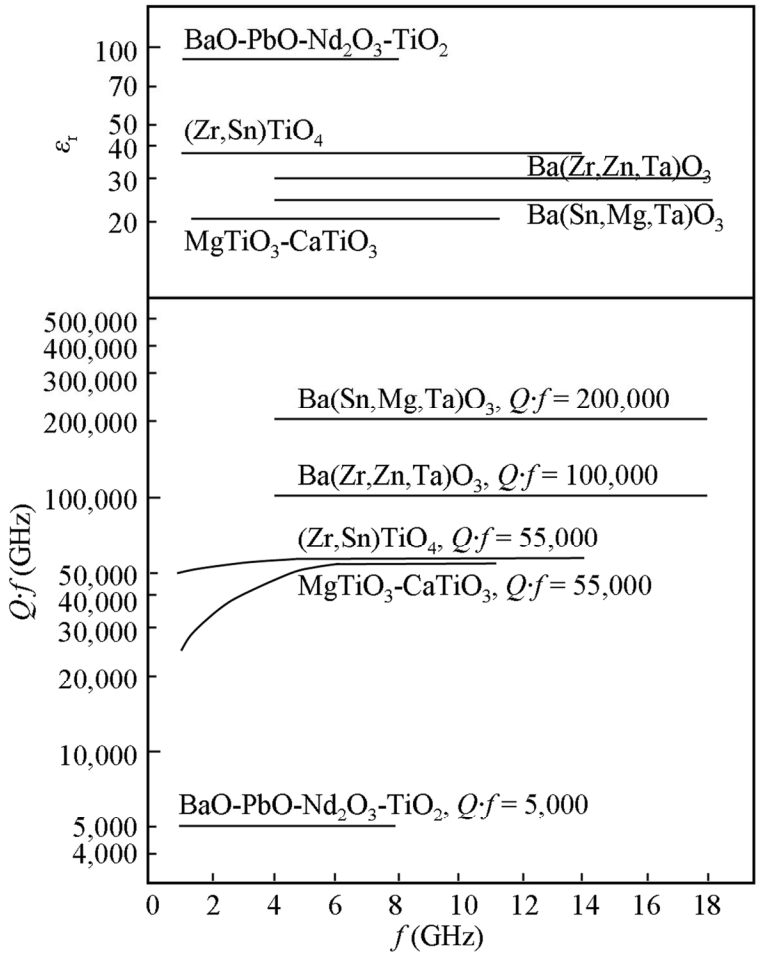

Figure 1.5: Frequency dependence of ε_r and (Q·f) for various dielectrics, after [20].

Dielectric properties of α-Al_2O_3 and TiO_2 are influenced by a number of factors, such as crystal structures, chemical compositions, impurities and, mostly overlooked, processing conditions and microstructural homogeneity. Detailed experiments were carried out in this study to optimize microstructures and minimize the loss. Sufficient temperature stability of α-Al_2O_3 and TiO_2 can be achieved by doping, which however is not of very high priority for the current MPAs, and hence will not be discussed here.

1.2.2 F layers

Faraday rotation (FR) as provided by F layers is a nonreciprocal magnetic phenomenon. When an EM wave propagates parallel to an external static magnetic field, its polariza-

tion direction is rotated during propagating through a diamagnetic, paramagnetic or ferrimagnetic (ferrite) medium. Compared to diamagnetic and paramagnetic materials, ferrites have much higher FR in a small external field and are therefore proposed for the MPAs [21]. Three types of ferrites have been widely used in MW applications, namely spinels, hexaferrites and garnets [6]. The differences in their crystal structures lead to unique magnetic properties and therefore MW applications. Garnets, which generally have the lowest loss of the ferrite family, are most likely to meet the low-loss requirements of the F layers. Cation substitutions are commonly carried out to achieve the special magnetic properties required by devices, as well as improving sintering behavior. However, optimized processing is rarely found in studies of substituted garnets. Commonly used solid-state co-firing is generally considered less effective in realizing homogeneous compositions and microstructures. As a result, poorly-defined chemical compositions and microstructural defects may offset the target improvement in properties by substitutions, and lead to unreliable characterization results.

Therefore, the preparation of F layers involved the selection of appropriate substitutions and fabrication methods. In the present study, multiple-substituted Ca,V,Zr-$Y_3Fe_5O_{12}$ garnets (CVZG) have been investigated to verify their reported low loss of $\tan\delta \leq 2\times10^{-4}$, low linewidth of $\Delta H \leq 1.2$ KA/m (15 Oe), and a high Curie temperature (T_C) around 235ºC [22-30]. Instead of co-firing, a citric-gel (Pechini [31]) method was chosen, being the preferred method for producing homogeneous multicomponent oxides. Aqueous citric acid (CA) and ethylene glycol (EG) form a gel upon evaporation of water, with a relatively rigid organic network in which cations are homogeneously dispersed and stabilized. The system homogeneity leads to much lower calcination temperatures and smaller particle sizes, than those in solid-state co-firing. The mechanical and electromagnetic properties of ferrites are largely affected by the sintering process, which depends on the applied time-temperature-atmosphere program. For example, garnets must be sintered in air or oxygen to ensure that all ions are in the highest oxidation state to avoid excessive dielectric losses at MW frequencies. Optimization of F material also takes into consideration any phase segregation, composition stoichiometry, particle size and morphology, and compact density. As a result, special attentions must be paid to:

- careful selection of precursor chemicals to avoid irremovable anions, such as Cl^-,
- possible decrease of the sintering temperature by doping,
- development of ceramic consolidation routes that target a high compact density, a fine grain size, and a homogeneous microstructure,
- fabrication of pore-free microstructures to avoid dissipation by adsorbed molecules like H_2O.

In summary, this study presents methods for fabrication and materials for microwave antennas, using MPAs for the purpose of demonstration. Chapter 2 briefly introduces dielectric theory in MW applications; Chapter 3 and Chapter 4 focus on fabrication of effective anisotropic dielectric materials. Ferrimagnetism and MW ferrite applications will be discussed in Chapter 5, followed by experiments on CVZG preparation and properties in Chapter 6. Based on the current results, Chapter 7 discusses future work needed to accommodate more advanced and complex antenna designs.

CHAPTER 2

DIELECTRIC THEORY

In this chapter, an introduction will be given for the relation between dielectric and materials properties, considering both intrinsic and extrinsic factors.

2.1 Dielectrics in a static field

In an electric field, a dielectric will respond with a limited rearrangement of charges so that the average centers of the positive and negative charges no longer overlap. Consequently the dielectric acquires an overall dipole moment, or: becomes polarized. The effect of polarization can be demonstrated in a parallel-plate capacitor filled with a dielectric, as shown in figure 2.1.

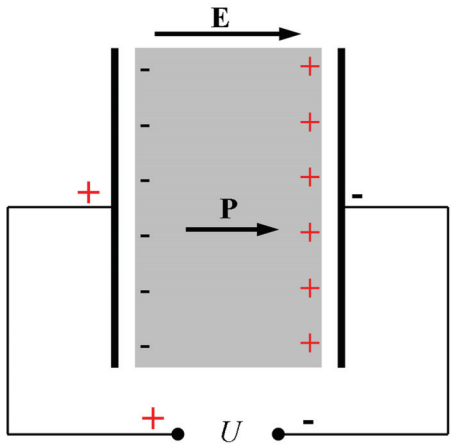

Figure 2.1: A parallel-plate capacitor filled with a dielectric.

In a static field of **E**, the electric displacement vector **D** and the polarization **P** (dipole moment per unit volume) in the dielectric are related as

$$\mathbf{D} = \varepsilon_0 \mathbf{E} + \mathbf{P} \tag{2.1}$$

where ε_0 is the permittivity of free space. For a linear dielectric material

$$\mathbf{P} = \chi_e \varepsilon_0 \mathbf{E} \tag{2.2}$$

where χ_e is the electric susceptibility. Therefore, equation (2.1) can be written as

$$\mathbf{D} = (1 + \chi_e)\varepsilon_0 \mathbf{E} = \varepsilon_r \varepsilon_0 \mathbf{E} = \varepsilon \mathbf{E} \tag{2.3}$$

where the permittivity of a dielectric is defined as

$$\varepsilon = \varepsilon_0 (1 + \chi_e) \tag{2.4}$$

and the relative permittivity, often called the dielectric constant, is

$$\varepsilon_r = \frac{\varepsilon}{\varepsilon_0} = 1 + \chi_e \tag{2.5}$$

2.2 Dielectrics in a MW field

Consider an alternating electric field of $U = U_0 \exp(j\omega t)$ is applied to a dielectric-filled capacitor as shown in figure 2.2(a). ω is the angular frequency of the applied field. For an ideal dielectric, the current in the circuit is

$$i = C\dot{U} = Cj\omega U_0 \exp(j\omega t) = j\omega CU \tag{2.6}$$

where $C = C_0\, \varepsilon_r$ is the capacitance and C_0 is the capacitance of an empty capacitor. Therefore, the current in an ideal capacitor leads U by 90º, resulting in a zero average power loss from the voltage source. In the case of a capacitor with a lossy dielectric, represented by a resistive shortcut, a complex relative permittivity $\varepsilon_r^* = \varepsilon_r' - j\varepsilon_r''$ is formulated, where ε_r' and ε_r'' are the real and imaginary parts of the relative permittivity respectively. For this case the current is

$$i = j\omega \varepsilon_r^* C_0 U = \omega \varepsilon_r'' C_0 U + j\omega \varepsilon_r' C_0 U = i_{loss} + j i_{cap} \tag{2.7}$$

As shown in figure 2.2(b), i_{loss} in phase with U, causes the energy dissipation, and i_{cap}, 90º ahead of U, does not lead to energy loss.

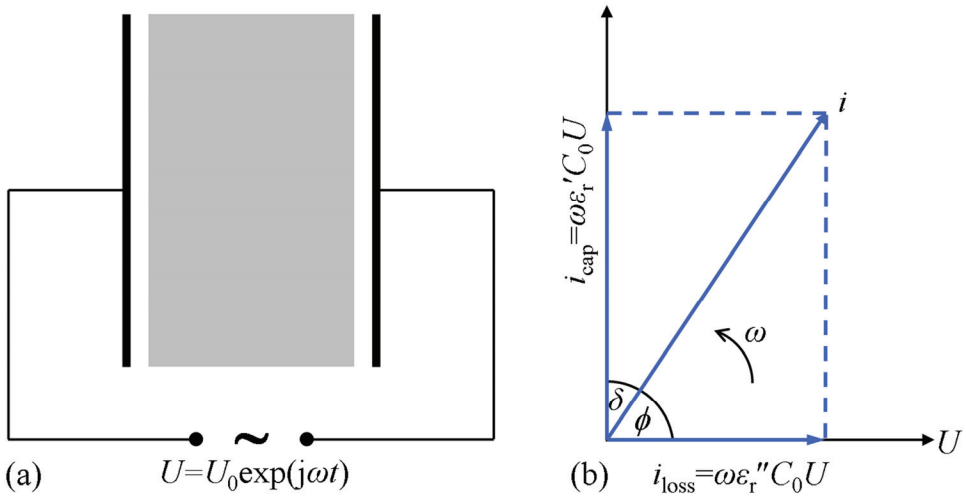

Figure 2.2: (a) A parallel-plate capacitor filled with a dielectric under an alternating electric field. (b) Phasor diagram for a real capacitor with "loss" current i_{loss}.

The dissipation factor, also called the dielectric loss tangent, is defined as

$$\tan\delta = \frac{\varepsilon_r''}{\varepsilon_r'} \tag{2.8}$$

which is the fraction of the product of i_{cap} and voltage, dissipated as heat. Experimentally $\tan\delta$ is determined by measuring the quality factor Q (i.e. $\frac{1}{\tan\delta}$) from a dielectric resonator

$$Q \approx \frac{f_0}{\Delta f} \tag{2.9}$$

where f_0 is the resonant frequency and Δf is the bandwidth measured at 3 dB (about half of the maximum height) of the resonance peak.

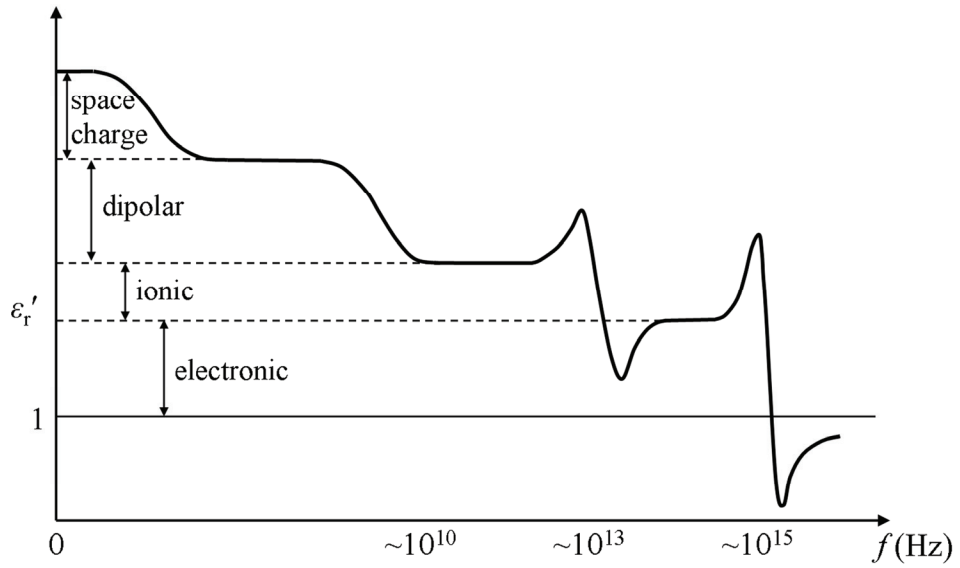

Figure 2.3: Variation of ε_r' with frequency after [1,32].

From microscopic point of view, the total polarization may be consisted as consisting of (a) electronic polarization from the displacement of electron clouds relative to a nucleus, (b) ionic polarization from the displacement of positively charged ions relative to negatively charged ions, (c) molecular polarization from re-orientation of permanent dipolar molecules, (d) space charge polarization from accumulation of charge at potential barriers, such as grain boundary or phase boundary [1,32]. Those polarization processes occur over a certain frequency range, and cease above certain frequencies where the specific displacement of charges can no longer follow the applied EM frequency, as shown in figure 2.3. In the MW region of 1-100 GHz, the primary polarization mechanisms are ionic and electronic. Both the electronic and ionic polarizations have inertia, which can be described as bound to the equilibrium position by a restoring force proportional to the displacement. In a practical dielectric, where energy dissipation occurs, a damping force is introduced in the equation of motion [1]. In a sinusoidal field of $E = E_0\exp(\mathrm{j}\omega t)$, the equation of the electron motion is

$$m_e\ddot{x} + m_e\gamma_e\dot{x} + m_e\omega_{e0}^2 x = q_e E_0 \exp(\mathrm{j}\omega t) \tag{2.10}$$

where x is the displacement, γ_e is a damping factor, m_e, ω_{e0}, q_e are the mass, natural resonance frequency and charge of the electron. By solving equation (2.10), the displacement becomes

$$x(t) = \frac{q_e E_0 \exp(j\omega t)}{m_e(\omega_{e0}^2 - \omega^2 + j\gamma_e\omega)} \tag{2.11}$$

In a dielectric having N_e effective electronic dipoles per volume, the complex polarization is given by

$$P_e = N_e q_e x(t) = \frac{N_e q_e^2 E_0 \exp(j\omega t)}{m_e(\omega_{e0}^2 - \omega^2 + j\gamma_e\omega)} \tag{2.12}$$

Similarly the ionic polarization is

$$P_i = \frac{N_i q_i^2 E_0 \exp(j\omega t)}{m_i(\omega_{i0}^2 - \omega^2 + j\gamma_i\omega)} \tag{2.13}$$

where N_i is effective ionic dipoles per volume, γ_i is the ionic damping factor, m_i, ω_{i0}, q_i are the mass, natural resonance frequency and charge of the ion. The electronic polarization occurs up to optical frequency of $\sim 10^{15}$ Hz, which means this polarization process has a response time of $\sim 10^{-15}$ s and hence is instantaneously stationary at MW frequencies. Therefore its contribution to the complex permittivity is constant at MW frequencies, and can be expressed as

$$\varepsilon_{r\infty} = 1 + \frac{P_e}{\varepsilon_0 E} \tag{2.14}$$

by combining equation (2.2), (2.5) and (2.12). At much lower frequencies when both electronic and ionic polarization can be considered instantaneously stationary, the permittivity is

$$\varepsilon_{r0} = 1 + \frac{P_i}{\varepsilon_0 E} + \frac{P_e}{\varepsilon_0 E} = \varepsilon_{r\infty} + \frac{P_i}{\varepsilon_0 E} \tag{2.15}$$

At MW frequencies when the contribution from the ionic polarization is no longer constant, the permittivity is given by the dielectric dispersion equation [33],

$$\varepsilon_{r\omega} - \varepsilon_{r\infty} = \frac{\omega_{i0}^2(\varepsilon_{r0} - \varepsilon_{r\infty})}{\omega_{i0}^2 - \omega^2 + j\gamma_i\omega} \tag{2.16}$$

The real and imaginary parts of $\varepsilon_{r\omega}$ are respectively

$$\varepsilon'_{r\omega} = \varepsilon'_{r\infty} + \frac{\omega_{i0}^2(\omega_{i0}^2 - \omega^2)(\varepsilon'_{r0} - \varepsilon'_{r\infty})}{(\omega_{i0}^2 - \omega^2)^2 + \gamma_i^2\omega^2} \tag{2.17}$$

$$\varepsilon''_{r\omega} = \frac{\gamma_i\,\omega_{i0}^2\omega(\varepsilon'_{r0} - \varepsilon'_{r\infty})}{(\omega_{i0}^2 - \omega^2)^2 + \gamma_i^2\omega^2} \tag{2.18}$$

Taking into account that $\omega_{i0} \gg \omega$ and $(\varepsilon'_{r0} - \varepsilon'_{r\infty}) = \text{constant}$ in the MW field results in

$$\varepsilon'_{r\omega} \approx \varepsilon'_{r\infty} + (\varepsilon'_{r0} - \varepsilon'_{r\infty}) = \varepsilon'_{r0} \tag{2.19}$$

$$\varepsilon''_{r\omega} \approx \frac{\gamma_i\,\omega(\varepsilon'_{r0} - \varepsilon'_{r\infty})}{\omega_{i0}^2} \propto \omega \tag{2.20}$$

Here combination of (2.19) and (2.20) shows that tan δ proportionally increases with the applied frequency

$$\tan\delta \propto \omega \tag{2.21}$$

and accordingly

$$Q = \frac{1}{\tan\delta} \propto \frac{1}{\omega} \tag{2.22}$$

$$Q \cdot f = \frac{1}{\tan\delta} \cdot \frac{\omega}{2\pi} = \text{constant} \tag{2.23}$$

The relation in (2.23) is used to extrapolate dielectric losses at high frequencies from low frequency measurements [34].

2.3 Dielectric losses

Dielectric losses are categorized into intrinsic and extrinsic losses, of which the intrinsic loss in a perfect dielectric defines the lower loss limit, and the extrinsic loss dominates the observed loss values.

2.3.1 Intrinsic dielectric loss

A theoretical explanation of intrinsic loss is provided in [35] by studying interactions of the phonon system in dielectrics with the photons in the MW field. A crystal, consisting of n atoms and N primitive cells, has $3nN$ degree of freedom. There are $3N$ acoustic modes, in which all atoms in a unit cell oscillate (nearly) in phase. In the remaining $3N(n\text{-}1)$ optical modes, sublattices of anions or cations oscillate in phase but the sublattices themselves are out of phase [32]. It should be mentioned that the (ordinary) dielectrics considered in this study have a Debye temperature Θ, much lower than T, so that optical modes are active. Resonant interaction occurs when the EM field oscillates at the same frequency as an optical mode. However at MW frequencies, there exist no phonons with a frequency and wave-vector ($k = \frac{2\pi}{\lambda}$, where λ is the wavelength) that are the same as those of the MW field. Therefore only anharmonic (non-resonant) interactions can contribute to the intrinsic MW loss. This intrinsic loss depends on the crystal structure and chemical compositions, as well as its temperature and frequency dependence. There are three main mechanisms for the intrinsic loss: three-quantum (phonon+photon) loss, four-quantum loss and quasi-Debye loss.

The three-quantum mechanism is photon absorption process involving two phonons, which satisfies energy and quasi-momentum conservation laws

$$\begin{aligned} &\Omega_{j1}(\mathbf{k}_1) \pm \Omega_{j2}(\mathbf{k}_2) = \omega, \\ &\mathbf{k}_1 \pm \mathbf{k}_2 = 0 \end{aligned} \tag{2.24}$$

where $\Omega_j(\mathbf{k})$ is a set of phonon modes with a wave-vector $\mathbf{k}$, and ω is the frequency of the field applied to the dielectric. The plus and minus signs correspond to decay and coalescence processes respectively. Three-quantum mechanism suggests ε_r'' due to these processes is proportional to T. The four-quantum mechanism is a photon process involving three phonons, also satisfying energy and quasi-momentum conservation laws

$$\begin{aligned} &\Omega_{j1}(\mathbf{k}_1) \pm \Omega_{j2}(\mathbf{k}_2) \pm \Omega_{j3}(\mathbf{k}_3) = \omega, \\ &\mathbf{k}_1 \pm \mathbf{k}_2 \pm \mathbf{k}_3 = \mathbf{b} \end{aligned} \tag{2.25}$$

where **b** is a reciprocal lattice vector. Contributions from the four-quantum mechanism to ε_r'' are suggested to be of a similar extent to those from three-quantum process. For crystal structures with center symmetry, $\varepsilon_{r\omega}'' \propto \omega T^2$ when $T \gg \Theta$. For crystal structures without center symmetry, the four-quantum loss can be ignored. Quasi-Debye losses are caused by perturbations of the phonon spectrum by the MW field. This contribution to the loss is expressed as

$$\varepsilon_{r\omega}'' \propto \frac{\omega\tau_p}{1+(\omega\tau_p)^2} \cdot \frac{T^4}{\Theta^3} \tag{2.26}$$

when $T \gg \Theta$. τ_p is a characteristic phonon relaxation time of the dielectric. This contribution only occurs in crystals without center symmetry.

2.3.2 Extrinsic dielectric loss

Compared with the intrinsic losses, extrinsic dielectric losses are dominant in real dielectrics. At MW frequencies, experimentally observed losses are often of 3-4 orders of magnitude higher than the theoretical intrinsic loss. The ensuing dramatic increase in $\tan\delta$ has been observed in various dielectrics, including Al_2O_3 and TiO_2 [36]. The extrinsic losses originate from imperfections in compositions, structures and microstructures.

An example of imperfect composition (or chemical nonstoichiometry) is found in reduced TiO_2. The dielectric loss increases due to electron hopping between cations of the same type on equivalent lattice sites, such as $Ti^{3+} \leftrightarrow Ti^{4+}$. The occurrence of this mechanism depends on the sintering temperature, atmosphere and cooling procedures during the thermal treatment, as well as impurities and dopants. Impurity ions, if they form solid solution in the host dielectric, may result in a variety of bond lengths in the unit cells, and thus enhance anharmonic dampening of phonon modes [37]. Impurities, which can not dissolve in the host dielectric, may form clusters or second phase that can have a high intrinsic loss or form scattering centers for the MW. The presence of a second phase is most common in multi-component dielectrics (with two or more cations, such as $BaTiO_3$) than simple dielectrics (with one cation, such as TiO_2). This can be ascribed to the possi-

ble phases, in addition to the target phase. Long-range site-ordering observed in complex oxides, like $Ba(Zn_{1/3}Ta_{2/3})O_3$, is also found to influence the dielectric loss [38,39]. Therefore the motivation for selecting α-Al_2O_3 and TiO_2 for the AD materials, as discussed in Chapter 1.2, is also based on their simple chemical composition, which results in less phase segregation and, because of that, better batch-to-batch consistency.

More attentions have been paid to the influence of microstructure on the dielectric properties, for example grain size, grain boundaries, porosity, and inhomogeneity [40-42]. Porosity is generally mentioned as a source of increased dielectric loss [40]. On the other hand there is still much more controversy in the literature about other factors that contribute to dielectric losses. These appear to vary for different dielectrics and even for the same dielectric prepared by different processing methods. Processing details can affect microstructures dramatically, through variations of the compacting method, additives, sintering temperature and dwell time. In order to lower dielectric loss, a homogeneous structure is favorable. Such a structure is achieved by starting with a homogeneous green body of high density, followed by well-controlled debindering (if any), sintering, and, if necessary, annealing.

CHAPTER 3

PHOTONIC ASSEMBLIES I: VERIFICATION OF DESIGN PRINCIPLE

In order to validate the design principle discussed in Chapter 1.2, an actual ceramic laminate was fabricated and measured for its dielectric anisotropy. Initially, the two constituent materials were commercially available polycrystalline α-Al_2O_3 and Nd-doped barium titanate substrates. Here, Nd-doped barium titanate substrates were used because dense TiO_2 substrates are unavailable, and their dielectric properties ($\varepsilon_r = 80$, $\tan\delta \sim 3\times10^{-4}$) approach those of TiO_2. Lamination by co-sintering is not very well possible for α-Al_2O_3 and Nd-doped barium titanate substrates due to their different thermal expansion coefficients (TEC). Therefore an additional, low temperature adhesive was applied during lamination. In this chapter, we will discuss the adhesive-assisted lamination and fabrication of AD materials and thin AD layers, as well as their application in photonic assemblies (PAs) [43].

3.1 Experiment procedure

Dense α-Al_2O_3 (purity 99.6%, $\varepsilon_r = 10$) and Nd-doped barium titanate (TD82, $\varepsilon_r = 80$) substrates were obtained from CoorsTek Inc., with dimensions of 50 mm × 50 mm × 0.5 mm and both surfaces lapped. They were diamond-machined, and alternatively piled to 8- and 15-layer AD stacks with dimensions of 25.0 mm × 7.5 mm × 4.0 mm as shown in figure 3.1. The lamination adhesives studied included organic double-tape 3M-9942, plastic adhesive 3M-4475, cyanoacrylate Loctite®-401, single-component epoxy Loc-

tite®-3982 and two-component epoxy M-bond 610. The adhesives were applied according to the manufacture instructions. To evaluate the adhesive influence on dielectric properties, α-Al_2O_3|TD82 stacks with no adhesive were also prepared by wrapping stacks with a 0.2 mm thin plastic thread. In concordance with the single crystal rutile structure, an equivalent crystallographic "a axis" was defined parallel to the original isotropic substrate surface planes, and a "c axis" perpendicular to those planes. As a result, the 8- and 15-layer stacks had their equivalent crystallographic axes oriented differently with respect to their geometric dimensions, as shown in figure 3.1. 1 mm thin AD layers were machined from AD laminates of 28 α-Al_2O_3 layers and 28 TD82 layers, using diamond cutting and grinding by Louwers Glass and Ceramic Technologies, the Netherlands. Two rutile crystals were obtained from MTI Corp., with 3 mm × 1.6 mm × 10 mm (*x*-*y*-*z*) dimensions. The crystallographic c axis of the 1st and 2nd rutile sample was along the *y* and *x* dimension, respectively.

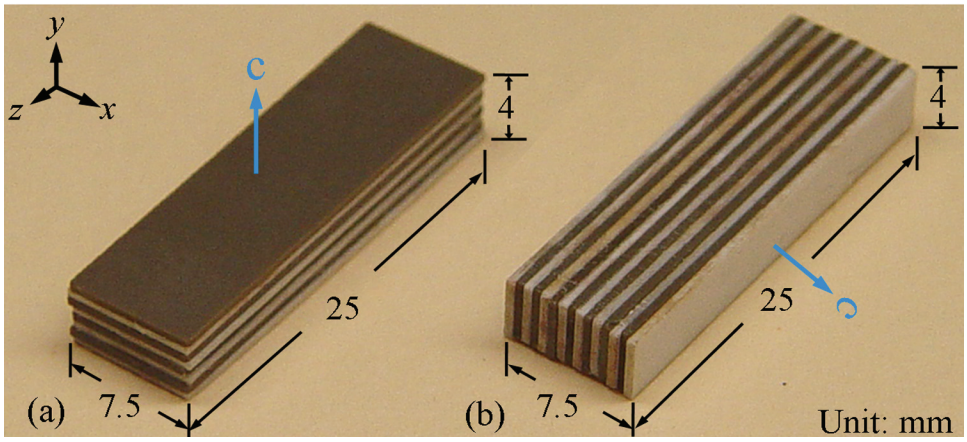

Figure 3.1: (a) 8- and (b) 15-layer stacks for dielectric measurements. The light and dark layers are α-Al_2O_3 and TD82 respectively. The effective crystallographic "c axis" is indicated, and the dielectric tensors are in equation (3.1)

$$\text{(a) } \varepsilon_r = \begin{pmatrix} 45 & 0 & 0 \\ 0 & 17.8 & 0 \\ 0 & 0 & 45 \end{pmatrix} \qquad \text{(b) } \varepsilon_r = \begin{pmatrix} 17.8 & 0 & 0 \\ 0 & 45 & 0 \\ 0 & 0 & 45 \end{pmatrix} \tag{3.1}$$

A resonant cavity measurement was used to characterize the complex dielectric constant ($\varepsilon_r^* = \varepsilon_r' - j\varepsilon_r''$) and dielectric loss [44]. The dimensions of the copper cavity (24 mm × 12.8 mm × 80 mm) were chosen so that specific resonant field distributions can be generated with most of the resonant energy concentrated within the sample. The cavity dimensions, as shown in figure 3.2, were 8 times those of the rutile samples, and 3.2 times those of the α-Al_2O_3|TD82 laminates. For the modes excited within the cavity, two different probe locations were determined by considering the hot spots of the electric field at the cavity walls. Two copper covers were manufactured, of which one cover with the probe (feed I) at the center, whereas the other cover having the probe (feed II) off the center.

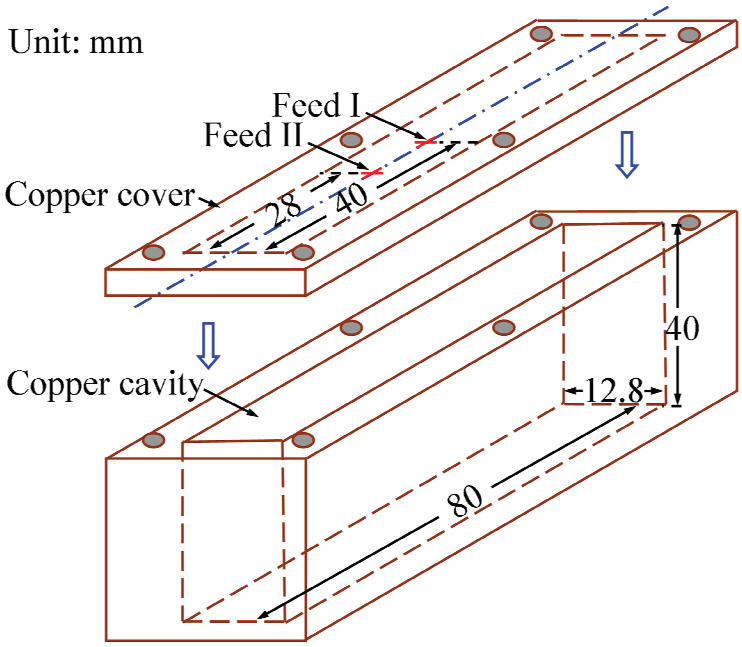

Figure 3.2: Sketch of the copper cavity.

The rutile samples, with their (anisotropy) orientation equivalent to that of the laminates, were placed in the center of the cavity to minimize energy dissipation in the walls, hence the loss due to the cavity itself. An Agilent E8362B network analyzer was used to de-

termine the resonance frequencies from power reflection coefficient (S_{11}) measurements [45]. The setup was designed so that the first order resonant modes had electric fields oriented along the largest geometric dimension. This allows for a one-dimensional search to characterize ε'_{ra} (real part of the dielectric constant along the a axis) independently using the 1st rutile sample. The measured resonance frequency was systematically matched to the computed one by varying ε'_{ra} in a finite-element-method (FEM, developed by ElectroScience Laboratory, The Ohio State University). Similarly, the 2nd rutile sample was used to determine ε'_{rc} (real part of the dielectric constant along the c axis). Modes that did not concentrate inside the sample were excluded from this consideration. ε'_{ra} (rutile) = 85 and ε'_{rc} (rutile) = 165 were applied as initial parameters in the FEM simulation. The dielectric loss tangent was estimated using [13]

$$Q_u^{-1} = p_{es}^a \tan\delta_a + p_{es}^c \tan\delta_c + \frac{R_s}{G} \tag{3.2}$$

where the unloaded Q_u (ratio of stored energy to dissipated energy per cycle) of the cavity system is calculated from S_{11} [45]. tan δ_a and tan δ_c are the loss factors along the a- and c- axis respectively, and R_s is the surface resistivity of the copper cavity. The electric filling ratios, p_{es}^a and p_{es}^c along the a- and c- axis were computed via FEM using the corrected values for ε'_{ra} and ε'_{rc}. The geometric factor G describes the amount of electric energy concentrated within the samples with respect to the overall energy inside the cavity. For the first modes in the rutile crystals, G factors were ~ 10^4, hence tan δ can be determined with an accuracy of 3×10^{-7} (or 3×10^{-5} if the wall loss was not accounted for [46]).

Characterization of the α-Al_2O_3|TD82 laminates was carried out similarly. For these samples, the G factor was calculated to be ~ 10^3, allowing for the determination of tan δ with an accuracy of 1×10^{-4}. To validate the effective medium model and the dielectric anisotropy of the laminates, the field distributions simulated using the tensors in equation (3.1) were compared with those from a full wave model using ε'_r (α-Al_2O_3) = 10 and

ε_r' (TD82) = 80. Dielectric properties of individual α-Al_2O_3 and TD82 substrates were measured using an Agilent E4991A 1 MHz-3 GHz RF Impedance/Material Analyzer.

3.2 Dielectric properties of α-Al_2O_3|TD82 laminates

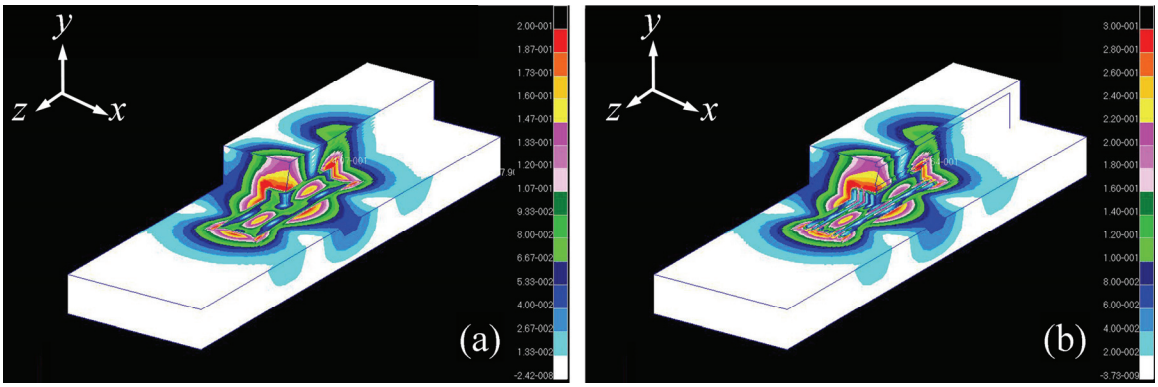

Figure 3.3: Field distributions of the resonant mode with the 15-layer stack, simulated using: (a) effective medium and (b) full wave model. Both calculations were carried out for a frequency of 7.64 GHz.

The field distributions obtained from the tensors and full wave model were nearly identical, as shown in figure 3.3, for an example of the 15-layer sample in figure 3.1(b). The measured resonance frequencies of the 8- and 15-layer laminates were different, in agreement with their anisotropic dielectric nature. The measurement results for the α-Al_2O_3|TD82 laminates as well as the homogeneous rutile crystals are summarized in table 3.1. Theoretical minimum losses in an ideal rutile structure are tan $\delta_a = 7\times10^{-10}$ and tan $\delta_c = 4\times10^{-10}$ caused by phonon scattering of the MW field [35], as discussed in Chapter 2.3. A real single crystal has higher losses due to defects in the crystal, such as impurities and vacancies. Additional energy dissipation in the commercial substrates and adhesive-free α-Al_2O_3|TD82 stacks is ascribed to porosity, microcracks, random crystallite orientation [17,18,36,42], polar species adsorbed on the oxide surfaces [15], oxygen deficiency in TD82, and EM wave reflections at the α-Al_2O_3 and TD82 contact surfaces.

Material	tan δ (frequency)	Adhesive thickness (μm)	Sustainability to machining
Rutile single crystal	tan $\delta_a = 1.39\times10^{-4}$, tan $\delta_c = 1.09\times10^{-4}$ (9.78 GHz)	--	--
α-Al_2O_3 substrate	2.8×10^{-4} (3.37 GHz)	--	Yes
TD82 substrate	3.7×10^{-4} (2.13 GHz)	--	Yes
Laminates w/o adhesive	0.9×10^{-3} (7.57 GHz)	--	--
Laminates w/ 3M-4475	1.9×10^{-3} (7.61 GHz)	--	No
Laminates w/ 3M-9942	2.6×10^{-3} (7.67 GHz)	~60	No
Laminates w/ Loctite®-401	2.9×10^{-3} (7.70 GHz)	~17	Yes
Laminates w/ Loctite®-3982	1.1×10^{-3} (7.57 GHz)	~2.6-4.5	No
Laminates w/ M-bond 610	1.9×10^{-3} (7.59 GHz)	~5-7	Yes

Table 3.1: Estimated tan δ in the α-Al_2O_3|TD82 laminates, comparing with that of rutile single crystal.

The α-Al_2O_3|TD82 laminates with adhesives had tan δ values 1.2-3.2 times that of the adhesive-free laminates mainly because of energy dissipation in the additional organic adhesives. The increased losses were closely related to the adhesive curing process and likely proportional to the overall adhesive volume. The highest loss was observed in laminates prepared with Loctite®-401, which is humidity-cured and consequently may have trapped water causing additional losses. On the contrary, the heat curing mechanism of Loctite®-3982 epoxy may have helped the removal of residual water, resulting in a low tan δ. The adhesive layers were examined using SEM as shown in figure 3.4 and

their thickness is listed in table 3.1. The laminates, prepared with fully liquid adhesives, i.e. 3M-4475 and Loctite®-3982, showed lower losses if superfluous adhesives were squeezed out during lamination. This confirmed that adhesives should be used as little as possible to minimize the loss. Loctite®-3982 with a low viscosity and Newtonian behavior formed thin adhesive layers of 2.6…4.5 µm under pressure, resulting in the lowest losses. The adhesive thickness is explained by <6 µm deviations of the local surface from the average flat substrate surface.

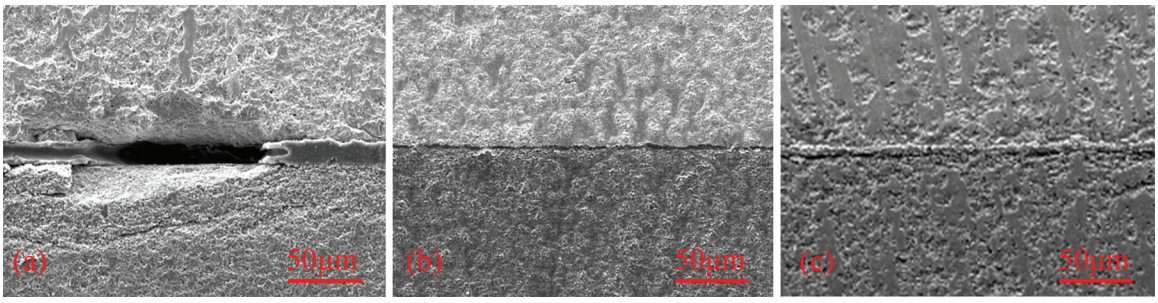

Figure 3.4: SEM images of adhesive layers (a) Loctite®-401 (with an unfilled gap), (b) Loctite®-3982 and (c) M-Bond 610.

3.3 AD layers and PAs for antenna application

AD layers of 1 mm thickness, as required by the MPA design, were obtained by diamond machining the adhesive-treated α-Al_2O_3|TD82 laminates. The laminates prepared with 3M-4475, 3M-9942 or Loctite®-3982, could not be machined into large intact layers possibly because of their poor water resistance (as water is the cooling medium for standard diamond machining). Considering the low-loss requirements and machinability, prototype AD layers were prepared from α-Al_2O_3|TD82 laminates with M-bond 610. A photonic assembly (PA) of such 12 AD layers is shown in figure 3.5. AD layers with 15º and 60º in-plane rotation respectively, defined with respect to the geometric plane sides, were fabricated with dimensions of 19.1 mm × 19.1 mm ×1.0 mm. Figure 3.6 shows another simplified PA of 3 unit cells, with each cell consisting of two 28.0 mm × 29.0 mm ×1 mm layers (AD_1 and AD_2) and 0.25 mm air gap. Since AD_1 and

AD_2 layers were both with 0º in-plane rotation, a relative geometric rotation, as discussed in Chapter 1.1, between AD_1 and AD_2 is needed to obtain a maximum gain. The optimum rotation angle was determined to be 55º, estimated from FEM simulated gain patterns and confirmed by experimental patterns. Figure 3.7 shows the simulated and measured far-field gain patterns of the antenna assembly when fed by a slot-coupled microstrip line (not shown). These constitute the first measurements of the prototype PAs antenna, based on the extraordinary propagation modes supported by degenerate band edge crystals [12]. Mismatches between the measured and simulated patterns can be attributed to the dielectric losses in the feed structure and AD layers, as well as the sample holder used in anechoic chamber measurements. It should be noticed that the dielectric loss in AD layers is limited by that of the individual substrates: 2.8×10^{-4} in α-Al_2O_3 and 3.7×10^{-4} in TD82. Therefore, this method of fabricating AD materials from the commercial ceramic substrates can be used to validate the design principles, but is not suitable for obtaining $\tan\delta \leq 10^{-4}$ as required for the target high-gain MPAs antennas. The following chapter will address our effort in decreasing dielectric loss by advanced ceramic processing.

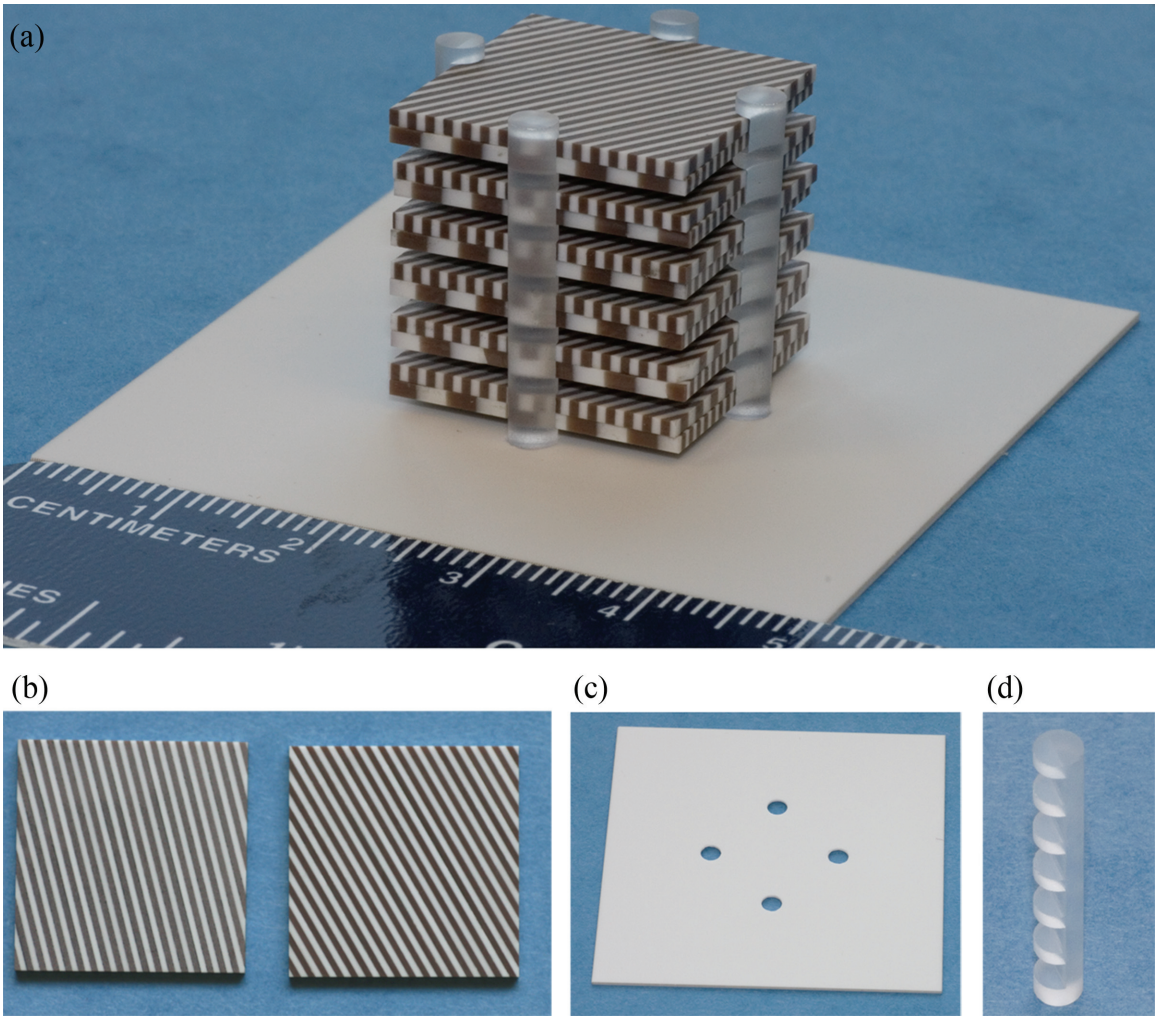

Figure 3.5: (a) 12-layer PA supported by vitreous silica scaffolds mounted in a dense α-Al_2O_3 substrate. (b) Two AD layers with 15º and 60º in-plane rotations respectively. (c) Dense α-Al_2O_3 substrate with holes drilled for mounting the vitreous silica scaffolds. (d) Supporting vitreous silica scaffold.

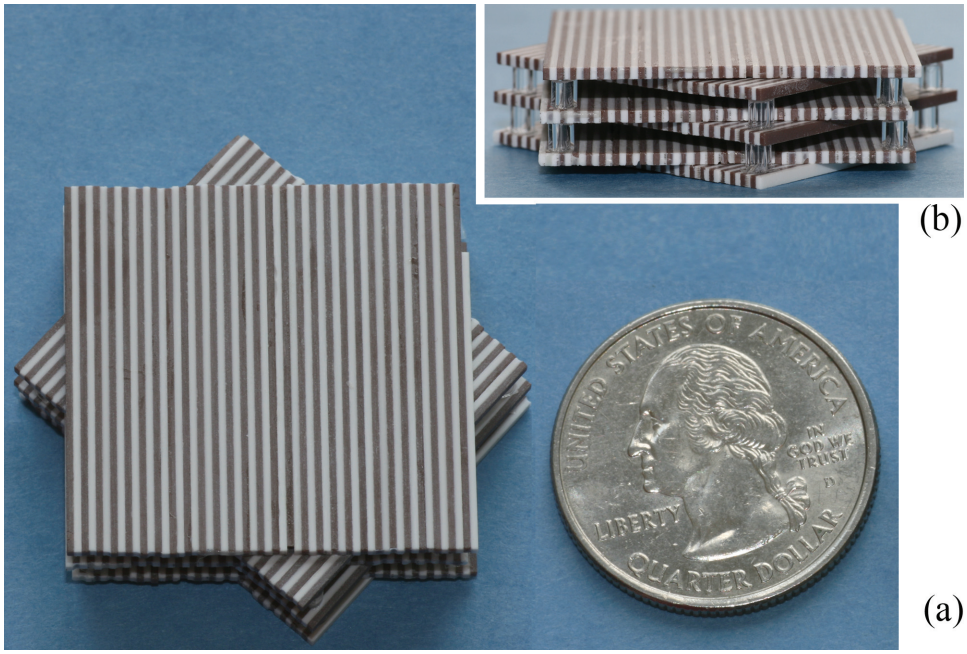

Figure 3.6: 6-layer PA consisting of 3 repeating units: (a) top view and (b) side view. The transparent spacers are 1.25 mm high quartz tubes.

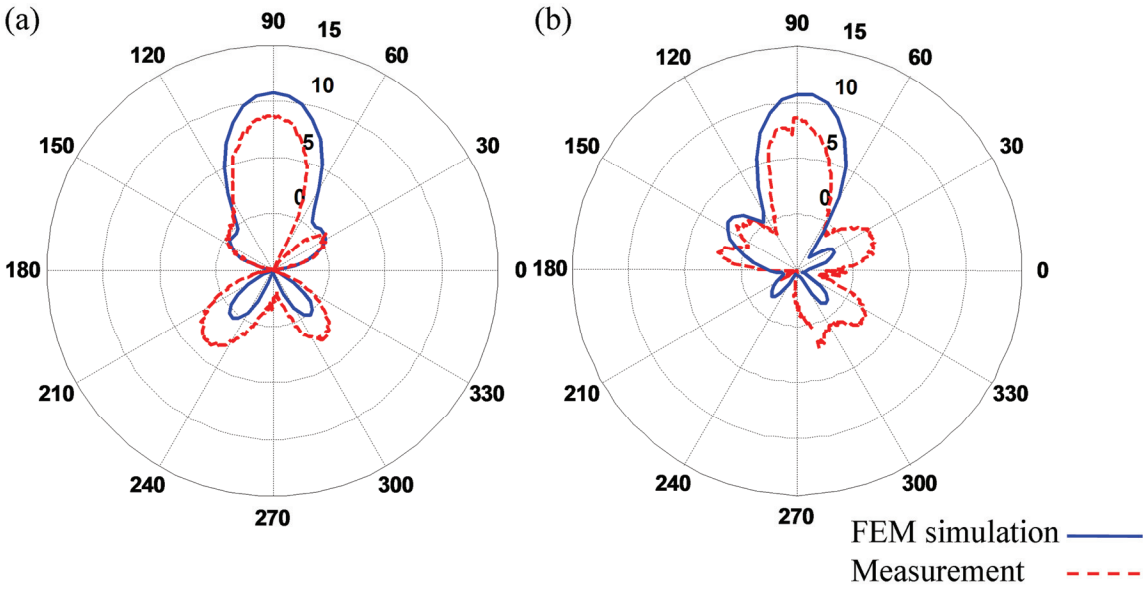

Figure 3.7: Measured and simulated gain (dB) patterns of the prototype in figure 3.6: (a) *x*-*z* cut and (b) *y*-*z* cut.

CHAPTER 4

PHOTONIC ASSEMBLY II: LOW-LOSS DIELECTRICS

In the previous chapter, the fabrication was discussed of effective medial anisotropic dielectrics from laminates of commercial α-Al_2O_3 and Nd-doped barium titanate. The prototype PAs assembled of such AD layers were found to have similar antenna patterns as predicted with FEM but with lower gains. This was primarily because the actual dielectric loss tan $\delta \sim 10^{-3}$ was higher than the required tan $\delta \leq 10^{-4}$. Therefore, we made an effort to prepare dense α-Al_2O_3 and TiO_2 with low dielectric loss using controlled colloidal processing. The original choice of polycrystalline rutile TiO_2 was kept as there was no restriction on the sample availability if prepared from scratch. Traditionally, α-Al_2O_3 or TiO_2 is densified by pressing powders and sintering in air or oxygen atmosphere at 1300-1500ºC for several hours [17,18,34,47,48]. The prepared samples have inhomogeneous microstructures and, especially for TiO_2, poor strength due to substantial grain growth (grain size > 10μm). High temperature sintering of TiO_2 also results in oxygen deficiency, and hence an increased tan δ due to resistive dissipation by mobile electronic charge carriers [49,50]. Acceptor dopants, such as Zn and Al, have been used to reduce tan δ by compensating the effect of reduction [18,50-52], but with little improvement of microstructures or decrease of sintering temperatures. Homogeneous microstructures with fine grains and low densification temperature can be achieved by processing monodisperse particles prepared by controlled hydrolysis of aluminum or titanium alkoxides [53,54]. Although no microwave dielectric measurements have been reported for such α-Al_2O_3 or TiO_2 samples, their homogeneous microstructure, small grain size and a low sintering temperature are expected to lead to a low tan δ [40,49]. However, the high cost

of alkoxides and high purity required, likely inhibit large scale production of α-Al_2O_3 or TiO_2 by this route.

This chapter presents low-temperature sintering of polycrystalline α-Al_2O_3 and TiO_2 with low dielectric loss at GHz frequencies, directly from commercial powders of very high chemical purity. Acceptor-doping of Al of TiO_2 was applied through gel-assisted infiltration [55], which led to a homogeneous doping concentration and microstructure after sintering.

4.1 Dense polycrystalline α-Al_2O_3

4.1.1 Experimental procedure

α-Al_2O_3 powders (AKP30, Sumitomo) were used, as received with > 99.99% purity and an average particle size ($\varnothing_p$) of 0.3 μm. 1 N HNO_3 (Ricca Chemical) was diluted to $p_H = 2.0$ with deionized water obtained from a Milli-Q® ultrapure water purification system (Millipore Corp.). A 20 vol% α-Al_2O_3 suspension was prepared by ultrasonically dispersing powders in the $p_H = 2.0$ HNO_3 solution. The ultrasonic treatment was carried out using a digital sonifier (Branson Ultrasonics Corp.) at 80 watts for 8 min in a 100 ml double-wall beaker (for a batch of 100 g suspension) [56]. The beaker was water-cooled to avoid excessive heating of the suspension by ultrasonic energy dissipation. The suspension was screened to remove any big agglomerates and foreign contaminations using a Nylon Spectra Mesh® with (a) 5 μm aperture, 2% opening area and 100 μm thickness or (b) 10 μm aperture, 2% opening area and 45 μm thickness (Spectrum Laboratories, Inc.). The nylon mesh was placed in a Nalgene filter holder (Nalgene reusable filter holders, Fisher) between the upper suspension chamber and lower receiver. The tip of the ultrasonic cone was kept at least 1.5 cm away from the mesh surface to avoid possible damage or deformation caused by the ultrasonic energy. Slight ultrasonification (3-4 watts) was applied during screening, to maintain a screening speed of 1.5…2 ml/min. Green compacts (disks) were formed by colloidal filtration of the suspension onto a polyethersulfone membrane with 0.22 μm pore size (Millipore Corp.). After drying overnight

in a Purifier^{TM} clean bench (Labconco Corp.), α-Al_2O_3 green compacts were sintered at 1300ºC for 10 hours with a 5ºC/min or 10ºC/min heating and cooling rate.

The apparent density of sintered α-Al_2O_3 was measured using a mercury pyconometer (Model DAB100-1, Porous Materials Inc.) at room temperature. That is because the contact angle of Hg on ceramics is > 90º, so that Hg does not wet the sample due to capillary force [47]. The weight of the empty calibration chamber was determined to be m_c. The chamber was filled with Hg up to a calibration mark, followed by determining the weight of m_{c+Hg}. The samples were added into empty chamber with a measured weight of m_{c+s}, then filled with Hg to the mark and a measured weight of m_{c+s+Hg}. The apparent density was calculated as

$$\rho_a = \frac{m_{c+s} - m_c}{(m_{c+Hg} - m_c) - (m_{c+s+Hg} - m_{c+s})} \cdot \rho_{Hg} \tag{4.1}$$

where the density of Hg (ρ_{Hg}) is 13.55 g/cm^3 at 20ºC. Once the apparent density is known, the relative density (ρ_r) and porosity (ϕ_p) are respectively

$$\rho_r = \frac{\rho_a}{\rho_t} \tag{4.2}$$

$$\phi_p = (1 - \frac{\rho_a}{\rho_t}) \cdot 100\% \tag{4.3}$$

where ρ_t is the theoretical density of the material, obtained from literature or determined by XRD patterns. Three samples were measured to obtain an average density, and a 95% confidence interval. SEM was carried out using a Field-Emission Environmental SEM Philips XL30 (Eindhoven, the Netherlands) on thermally etched surfaces of sintered α-Al_2O_3 samples. Grain size ($\varnothing_g$) and microstructural homogeneity are obtained more representative and reliable from polished and etched cross-sections than from as-formed surfaces. This is because the superficial grains experience a different environment (less neighboring grains, atmospheric ambient) than the grains inside the bulk sample. Before thermal etching, step-wise polishing was carried out to the sample cross-section until shiny surfaces were obtained. Polishing of sintered α-Al_2O_3 with a typical 5 mm×5 mm surface area was done using the following sequence of media:

1. 800 grit (CAMI standard, average particle diameter of 12.2 μm) SiC papers at ~45 N force for 30-40 mins,
2. 9 micron diamond paste at ~45 N force for 30-40 mins,
3. 3 micron diamond paste at ~45 N force for 30-40 mins,
4. 1 micron diamond paste at ~45 N force for 30-40 mins.

The well-polished samples were etched at a temperature, 50ºC lower than the original sintering temperature, using a heating/cooling rate of 10ºC/min without dwelling. Since dielectrics are good insulators, the samples were coated with Au to avoid surface charging during SEM analysis. The average $\varnothing_g$ was analyzed using a linear intercept technique, interpreted for nontextured grains of tetrakaidecahedral shape [57]. At least 200 grains were used in each sample to obtain sufficient accuracy.

Sintered α-Al_2O_3 was machined by Louwers Glass and Ceramic Technologies, the Netherlands, to 3.75 mm × 12.50 mm × 2.00 mm dimensions proportional to those of the copper cavity in figure 3.2, for dielectric measurements. Those dimensions were chosen such that the resonant electromagnetic field modes with a strong electromagnetic field were concentrated primarily within the sample at the center of the cavity. The complex dielectric constant was measured using the method described in Chapter 2.3. A parallel dielectric measurement was also performed on an Agilent E4991A 1 MHz-3 GHz RF Impedance/Material Analyzer.

4.1.2 Results and discussions

As reported previously [56], 20 vol% dispersed α-Al_2O_3 suspensions were screened using a nylon mesh with a 20 μm mesh with apertures covering 14% of the apparent opening area. However it was observed that the suspension flew through the mesh without hindrance and very little particulate contamination was left behind on the mesh surface. This indicated that the 20 μm opening was too wide to effectively screen agglomerates; and a smaller opening size was required. A practical guide was to have a mesh opening size 10 times of the primary particle size, which is 0.3 μm in the case of AKP30 α-Al_2O_3. Meshes with 5 μm and 10 μm openings were used to replace the 20 μm mesh. As observed by SEM images, and shown in figure 4.1, the 5, 10 and 20 μm meshes had effec-

tive apertures of 3, 9 and 20 μm respectively. Unassisted screening with a 5 or 10 μm mesh halted after the first 1-2 ml of the suspension, which was attributed to a small open area fraction (2%) that resulted in easy block by big agglomerates. Slight ultrasonic agitation was hence introduced during screening to keep the openings free from agglomerates and to enable the small particles to pass through.

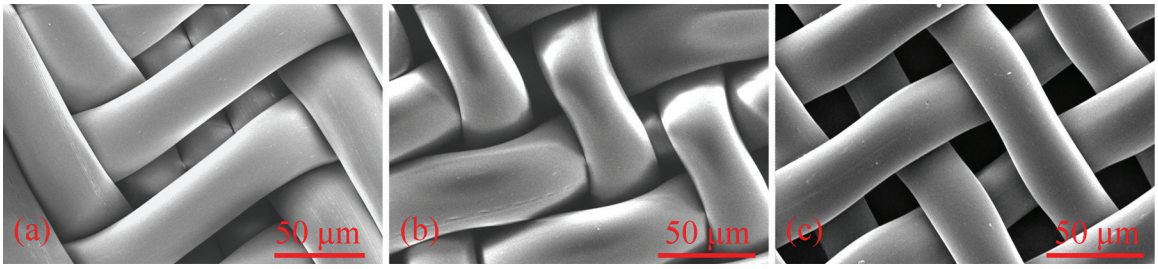

Figure 4.1: SEM images of nylon meshes with (a) 5 μm, (b) 10 μm and (c) 20 μm opening.

Figure 4.2 shows the SEM images of dense samples prepared from 20 vol% suspensions screened with 5 or 10 μm nylon meshes. Those sintered samples had similar grain morphology with an average $\varnothing_g$ of 1.6 μm. The 10 μm meshes were used routinely because screening with 5 μm meshes required a much longer time. In order to minimize unfavorable grain growth, a fast heating rate is required within the capabilities of the furnace. 5ºC/min and 10ºC/min heating rates were tested, but found to have little influence on the grain size or morphology of dense α-Al_2O_3. A 5ºC/min heating was applied for subsequent experiments, as it was considered to cause less damage to the furnace than the 10ºC/min rate. The relative density of the sintered α-Al_2O_3 was measured to be 97.9±1.1%.

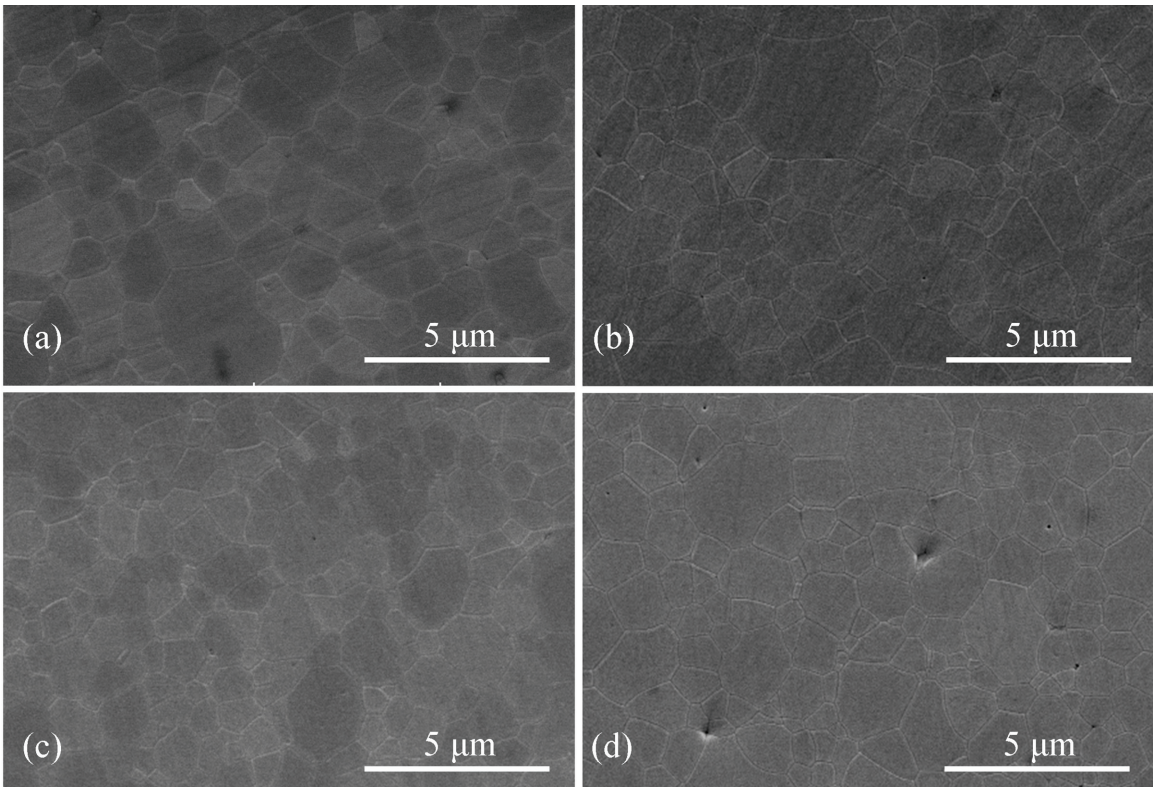

Figure 4.2: α-Al_2O_3 sintered at 1300ºC for 10 hours. The screening mesh and heating rate were respectively (a) 10 μm, 10ºC/min, (b) 5 μm, 10ºC/min, (c) 10 μm, 5ºC/min and (d) 5 μm, 5ºC/min.

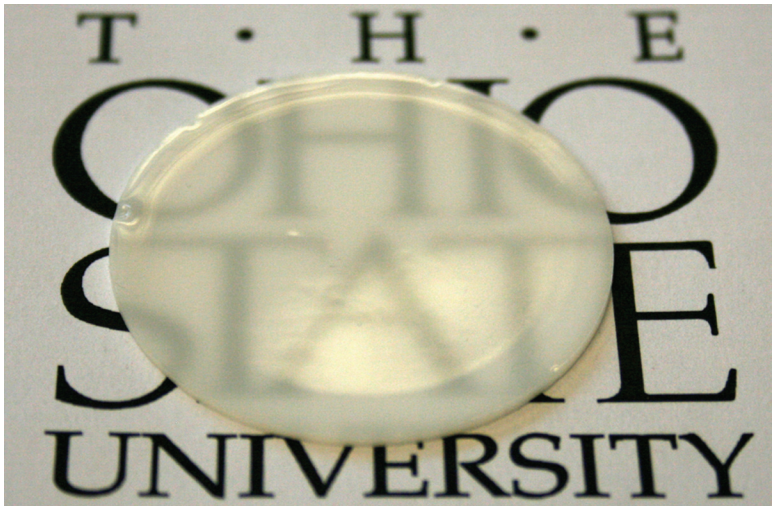

Figure 4.3: Image of a translucent α-Al_2O_3 (1300ºC sintered, 0.5 mm thick).

The sintered α-Al_2O_3 was translucent to visible light, as shown in figure 4.3. This translucency is attributed to the homogeneous, almost-dense microstructure and the small grain size. Real transparency, however, was not observed mainly because of light scattering at residual pores, grain boundaries, the unpolished bottom surface and/or due to intrinsic birefringence of the grains [58]. Residual pores, possibly the main reason for the observed translucency, may have originated from microbubbles, introduced into the α-Al_2O_3 suspensions during screening treatment. Such bubbles can become entrapped in the compact, and end up as large pores that can not be removed by sintering.

Initial measurements using the Agilent network analyzer indicated a tan δ less than 10^{-4} (beyond the instrument capability). In-cavity resonance measurement did not provide accurate tan δ values. This was because the low dielectric constant of α-Al_2O_3 resulted in several and closely separated resonance peaks at 1…10 GHz that could not be matched accurately to simulation. More delicate calculations are currently carried out in Electro-Science Laboratory, targeting α-Al_2O_3 rectangles of larger dimensions which are expected to result in separated resonance peaks.

4.2 Dense polycrystalline TiO_2

Like α-Al_2O_3, dense TiO_2 was prepared using colloidal filtration and low-temperature sintering. The detailed processing parameters were tuned for specific TiO_2 powders, such as the stabilizing media, suspension solid load and sintering temperature [59].

4.2.1 Experimental procedure

TiO_2 powders (PT-401L, Ishihara Corp.) were used as received, and had > 99.99% purity, 72.7 wt% rutile phase and an average $\varnothing_p$ of 0.15 μm, all according to the manufacturer's specifications. The powders were ultrasonically dispersed in aqueous NH_3 with p_H = 10.5 at a solid load of 14 vol%. For a batch of 100 g TiO_2 suspension, the ultrasonic treatment was carried out at 70 watts for 8 min in a 100 ml double-wall beaker. The TiO_2 suspension was screened using a 5 μm aperture Nylon Spectra Mesh® and ultrasonic enhancement. Like α-Al_2O_3 preparation, TiO_2 green compacts were formed by pressure filtration and afterwards drying overnight. Green compacts were then calcined for

10 hours at 600ºC…1300ºC, with a 5ºC/min heating and cooling rate. These prepared samples are denoted as $600TiO_2$, $700TiO_2$…$1300TiO_2$, respectively.

Zeta (ζ)-potential measurements were performed on 1.25 vol% TiO_2 aqueous suspensions using a Zetaprobe Analyzer^{TM} (Colloidal Dynamics Inc.). The titrants included electrostatic stabilizers: 5 mol/L HNO_3 and 5 mol/L tetramethyl ammonium hydroxide (TMAH), and an electrosteric stabilizer: 1 mol/L Aluminon solutions [56]. To further study the colloidal stability of TiO_2 in aqueous HNO_3 and NH_3 solutions, 12.5 vol% TiO_2 suspensions were prepared in HNO_3 solutions with $p_H = 2.03$, 2.35, 2.65 and 3.05, and NH_3 solutions with $p_H = 9.38$, 10.48 and 11.10. The p_H of the HNO_3, NH_3 solutions, TiO_2 suspensions and gels were measured using a p_H/ISE meter (Model 710A, Orion). X-ray diffraction (XRD) was performed on both as-received powders and thermal-treated TiO_2 samples. The obtained diffraction patterns were matched with data published by the International Center for Diffraction Data (ICDD-JCPDS). In this study, XRD was carried out using a Scintag XDS2000 diffractometer with Cu K_α radiation ($\lambda = 1.5406$ Å) in the range of $2\theta = 20…80°$. The XRD data were analyzed using Topas Academic software to determine the phase compositions. The apparent density (ρ_a) of green, calcined/sintered TiO_2 compacts samples measured using an Hg pyconometer at room temperature. Green compacts were dried at 300ºC for 10 hours (denoted as $300TiO_2$) to obtain sufficient mechanical strength for density measurement. For each treatment temperature, three samples were measured to obtain an average density, and a 95% confidence interval.

SEM was carried out on as-formed surfaces (without polishing) if thermal treatment was at < 900ºC, or thermally-etched cross-sections if thermal treatment was at ≥ 900ºC. This distinction was made because in the more porous samples (sintered < 900ºC) polishing of the loosely packed grain structure easily caused debris between grains. Since the Moh's hardness of TiO_2 (6-6.5) is lower than that of α-Al_2O_3 (9), it required fewer polishing steps. TiO_2 with a typical 5 mm×5 mm area, was well-polished after using

- 9 micron diamond paste at ~25 N force for 15 mins,
- 3 micron diamond paste at ~25 N force for 15 mins,
- 1 micron diamond paste at ~25 N force for 15 mins.

The average grain size in 900…1300TiO_2 was characterized using the linear intercept method. The mechanical strength of 900…1300TiO_2 samples (disks) was determined using a biaxial flexure mode with the indented side under tension. The load was applied with a flat punch and a material testing system (Model 810, MTS Systems Corp.). For each temperature, three to four samples were tested and the strength was calculated using a thin plate stress-strain formula [60]. For microwave loss characterization, sintered TiO_2 samples were diamond-machined to dimensions of 3.75 mm × 12.50 mm × 2.00 mm by Louwers Glass and Ceramic Technologies, the Netherlands. The complex dielectric constant was measured following the descriptions in Chapter 2.3.

4.2.2 Results and discussions

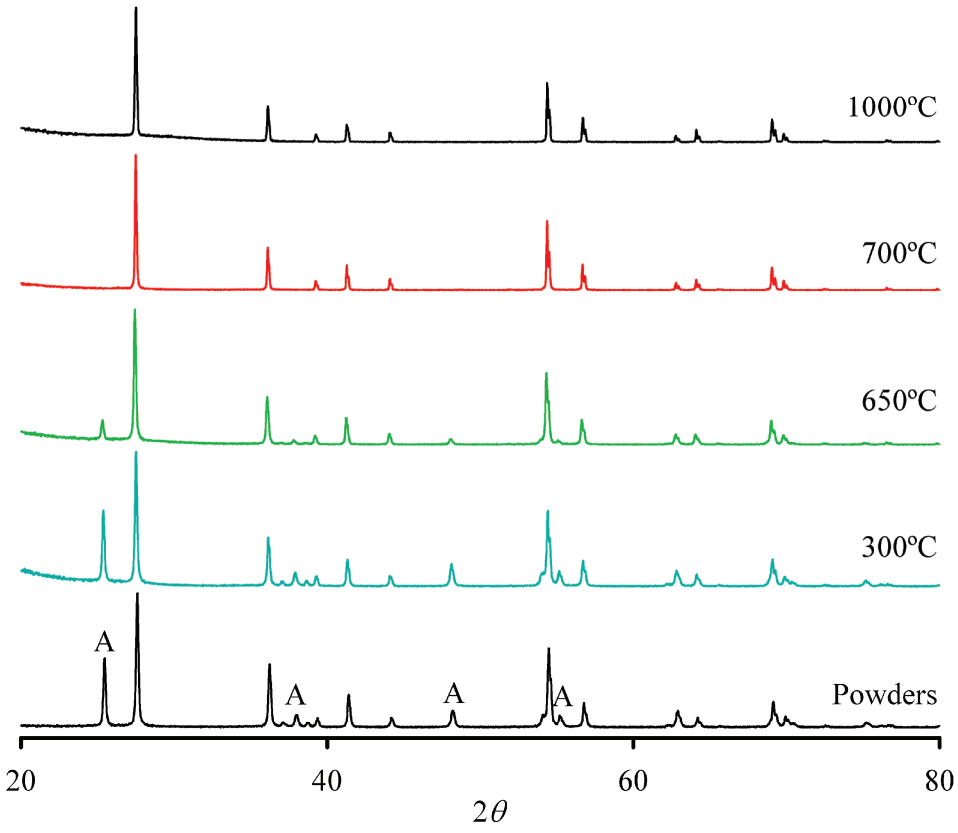

Figure 4.4: XRD patterns of TiO_2 powders and calcined samples. Diffraction peaks from the anatase phase are indicated by A.

As-received TiO_2 powders consist of rutile phase (72.7 wt% from manufacturer data) and, besides that, mostly anatase phase as shown in the XRD pattern in figure 4.4. This impurity anatase phase is a natural result of the preparation routes for high purity powders. These routes are based on the availability of high purity precursors, use of low processing temperatures, and avoiding mechanical reduction of particle size. The average bulk density of the powders was 4.16 g/cm^3, estimated from

$$\rho_{Ave} = \frac{\rho_R \cdot \rho_A}{wt\%_R \cdot \rho_A + wt\%_A \cdot \rho_R} = 4.16 \text{ g/cm}^3 \qquad (4.4)$$

where $wt\%_R$ and $wt\%_A$ are the weight percentage of the rutile and anatase phase respectively, and $\rho_R = 4.25$ g/cm^3 and $\rho_A = 3.89$ g/cm^3 are density of the rutile and anatase phase respectively. $300TiO_2$ used for green density measurement, had identical XRD patterns as those from as-received powders. After treatment at >700ºC, the anatase phase completely transformed to rutile, confirmed by XRD. The dominant as-received impurities include 25 ppm Fe_2O_3, 10 ppm Nb_2O_5 and 10 ppm Na_2O. This impurity concentration was at least 10 times less than the intentional doping levels of 300…1200 ppm used in this study, as discussed in the next section. Therefore the commercial TiO_2 powders as mentioned were considered suitable for a study on the dielectric properties of undoped and intentionally doped polycrystalline rutile TiO_2.

Figure 4.5 shows the ζ potential of 1.25 vol% TiO_2 suspensions titrated with HNO_3 and TMAH solutions respectively. The isoelectric point (IEP) of the TiO_2 powders was measured to be at $p_H = 6.2$. ζ reached a maximum of 85 mV at $p_H = 2.5$ and -93 mV at $p_H = 12.0$. It ($|\zeta|$) was always < 60 mV when Aluminon stabilizer was used with a concentration up to 0.13 wt% (with respect to the dry TiO_2 powders) as shown in figure 4.6. Though Aluminon may show a high $|\zeta|$ in basic environment [56], stabilization by solely H^+ or OH^- was preferred to avoid another, possibly contaminating additive. The decrease of ζ potential at $p_H < 2.3$ is ascribed to dissolution of TiO_2 in HNO_3. This was not observed at high p_H values. Suspensions with a usable solid load of 12.5 vol% TiO_2 suspensions were prepared with various HNO_3 solutions with $p_H = 2.0…2.7$ and NH_3 solutions with $p_H = 9.4…11.1$, to establish the practical p_H range. It was found that gelation occurred if the initial solutions had $2.6 < p_H < 9.5$, as shown in figure 4.7. Sedimentation

experiments were carried out for the remaining p_H ranges. The suspensions with $p_H = 2.3$ and 10.0 were observed to be the most stable, and were prepared from $p_H = 2.0$ HNO_3 and $p_H = 10.5$ NH_3 solutions respectively. Since the acidic $p_H = 2.3$ is close to the p_H where TiO_2 started to dissolve, $p_H = 10.0$ TiO_2 suspension was used to prepare green compacts.

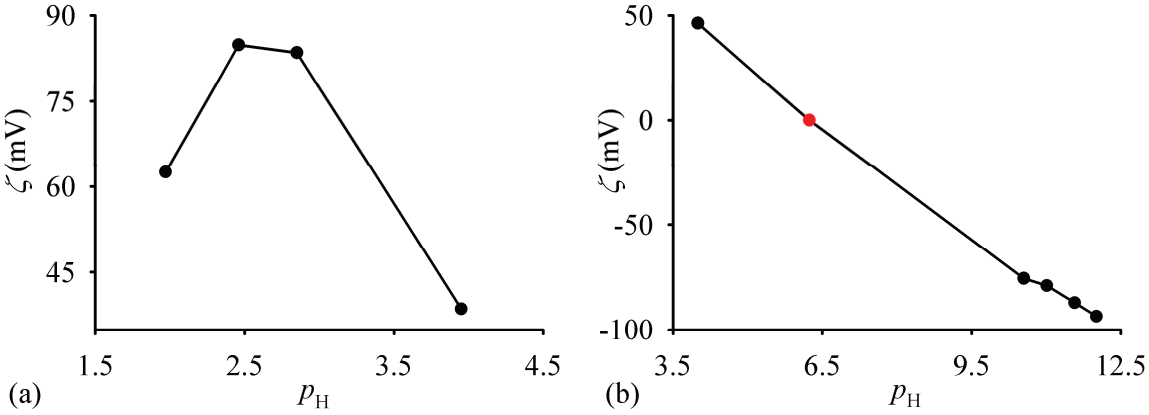

Figure 4.5: Zeta potential of 1.25 vol% TiO_2 suspension using titration with 5 mol/L (a) HNO_3 and (b) TMAH. The IEP point is highlighted in red.

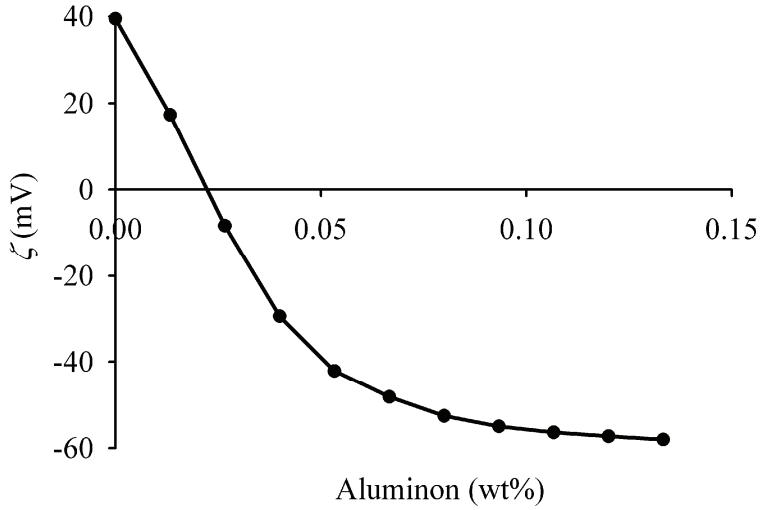

Figure 4.6: Zeta potential of 1.25 vol% PT-401L suspension in the presence of 1 mol/L Aluminon.

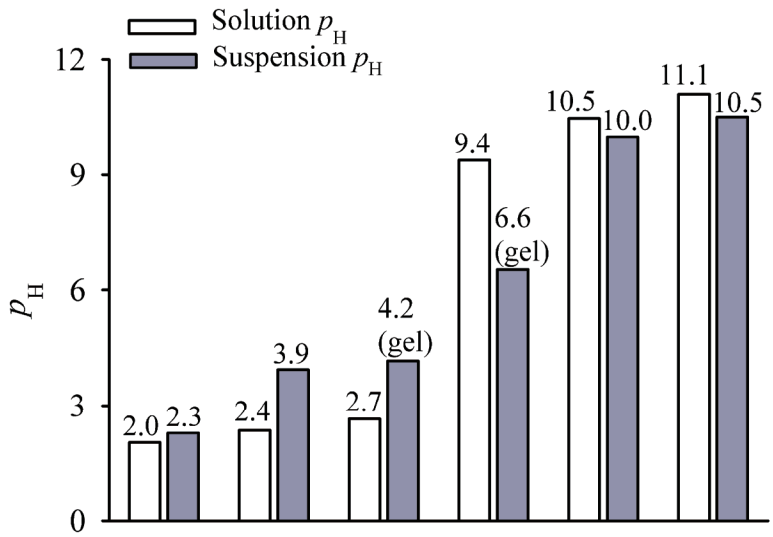

Figure 4.7: p_H of the HNO_3, and NH_3 aqueous solutions, 12.5 vol% PT-401L suspensions or gels.

The solid load in the TiO_2 suspension was optimized to achieve both high green density and efficient colloidal-filtration. Starting with $p_H = 10.5$ NH_3 solution, TiO_2 suspensions with >20 vol% solid load appeared to have a $p_H < 9.2$, and sedimentation occurred within minutes. A lower solid load generally led to a higher green density, but also required more suspension volume to obtain eventually dense samples with certain mass and dimensions. This, in turn, required a longer filtration time, leading to gradual unwanted sedimentation or segregation in the supernatant. For example, the required filtration times for 25 ml 10.0vol%, 20 ml 12.5 vol% and 13 ml 19 vol% TiO_2 suspensions were > 6 hours, 4.5-5 hours and 2.5 hours, respectively. Hence 17 ml 14 vol% TiO_2 suspension with 3.5 hours' filtration was chosen as a compromise between high green density and filtration efficiency (targeting sintered TiO_2 samples with 2 mm thickness for in-cavity measurements). After filtration and drying, the green compacts remained intact with sufficient strength for handling and a smooth shiny surface, as shown in figure 4.8. These observations are in agreement with a high measured relative density of $\rho_r = 57.5 \pm 0.7\%$.

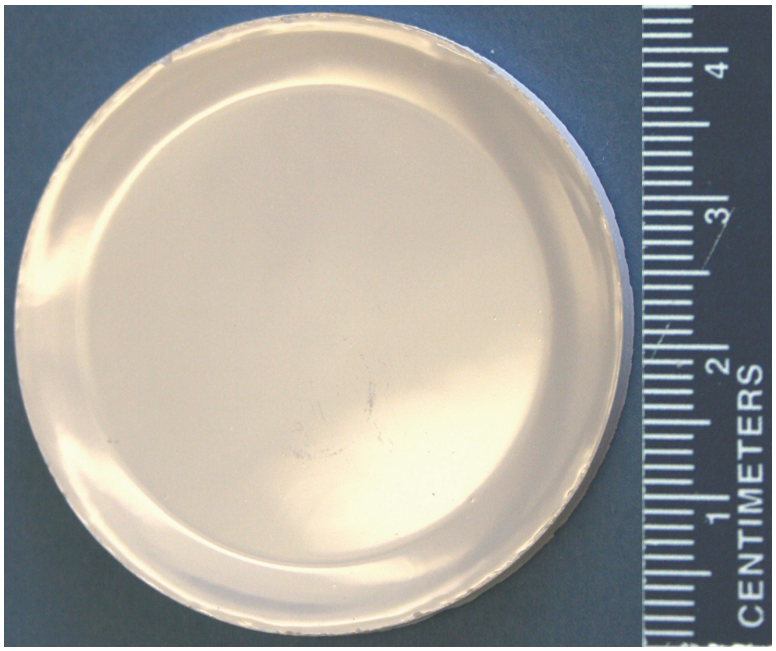

Figure 4.8: TiO_2 green compact after drying overnight.

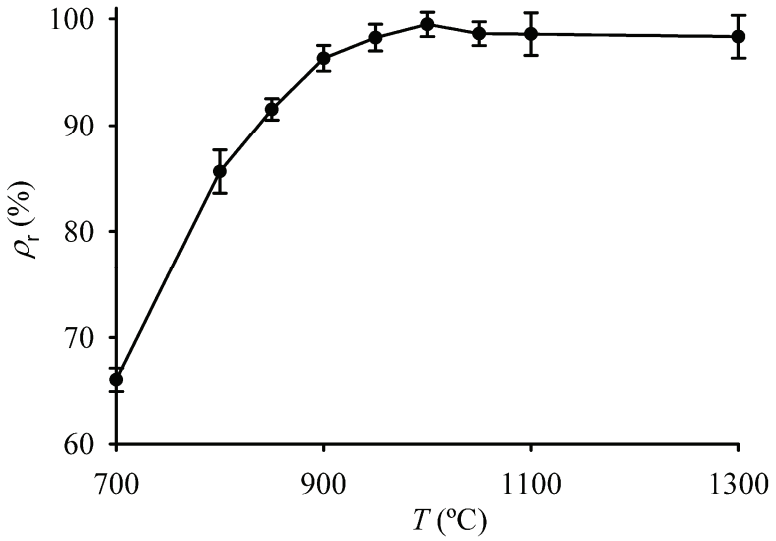

Figure 4.9: ρ_r of TiO_2 versus sintering temperature.

As the sintering temperature increased, the relative density of TiO_2 increased and reached 99.5±1.1% at 1000ºC, as shown in figure 4.9. This densification temperature is, to our

knowledge, the lowest for commercial undoped TiO_2 powders. It was achieved primarily because of the optimized homogeneity of the TiO_2 green compact. A higher temperature, however, resulted in a small but significant decrease in ρ_r. This is attributed to desintering by anomalous grain growth and/or expansion by oxygen released from TiO_2 reduction [61]. It is worth noting that the coring effect (a dark core region in the center of the sample), though reported elsewhere [18], was not observed in our study for all the calcining and sintering temperatures.

The SEM images in figure 4.10 and 4.11 show as-received TiO_2 powders and calcined/sintered samples. The faceted pores in $900TiO_2$ were due to break-out of grains during polishing of the relatively porous samples. The average TiO_2 grain size ($\varnothing_g$) grew exponentially with temperature from 0.5 μm, 1.1 μm, 2.2 μm, 4.0 μm to 14.4 μm in $800TiO_2$ to $1300TiO_2$, as shown in figure 4.12.

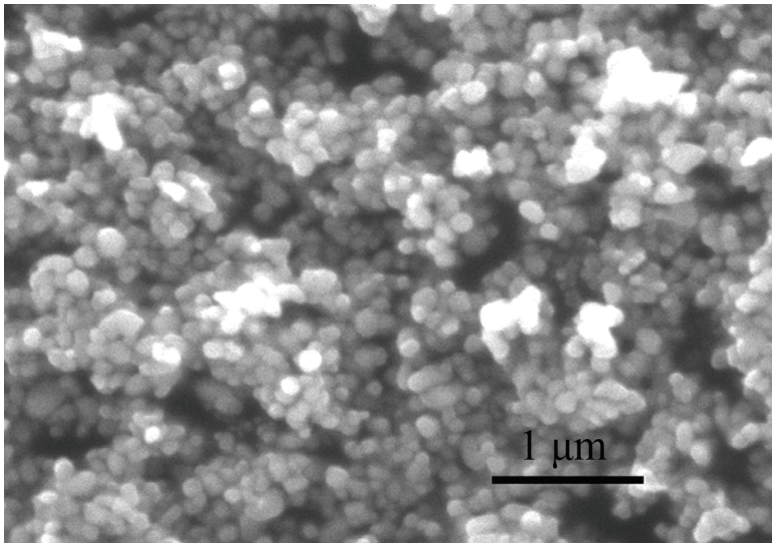

Figure 4.10: SEM of as-received TiO_2 powders.

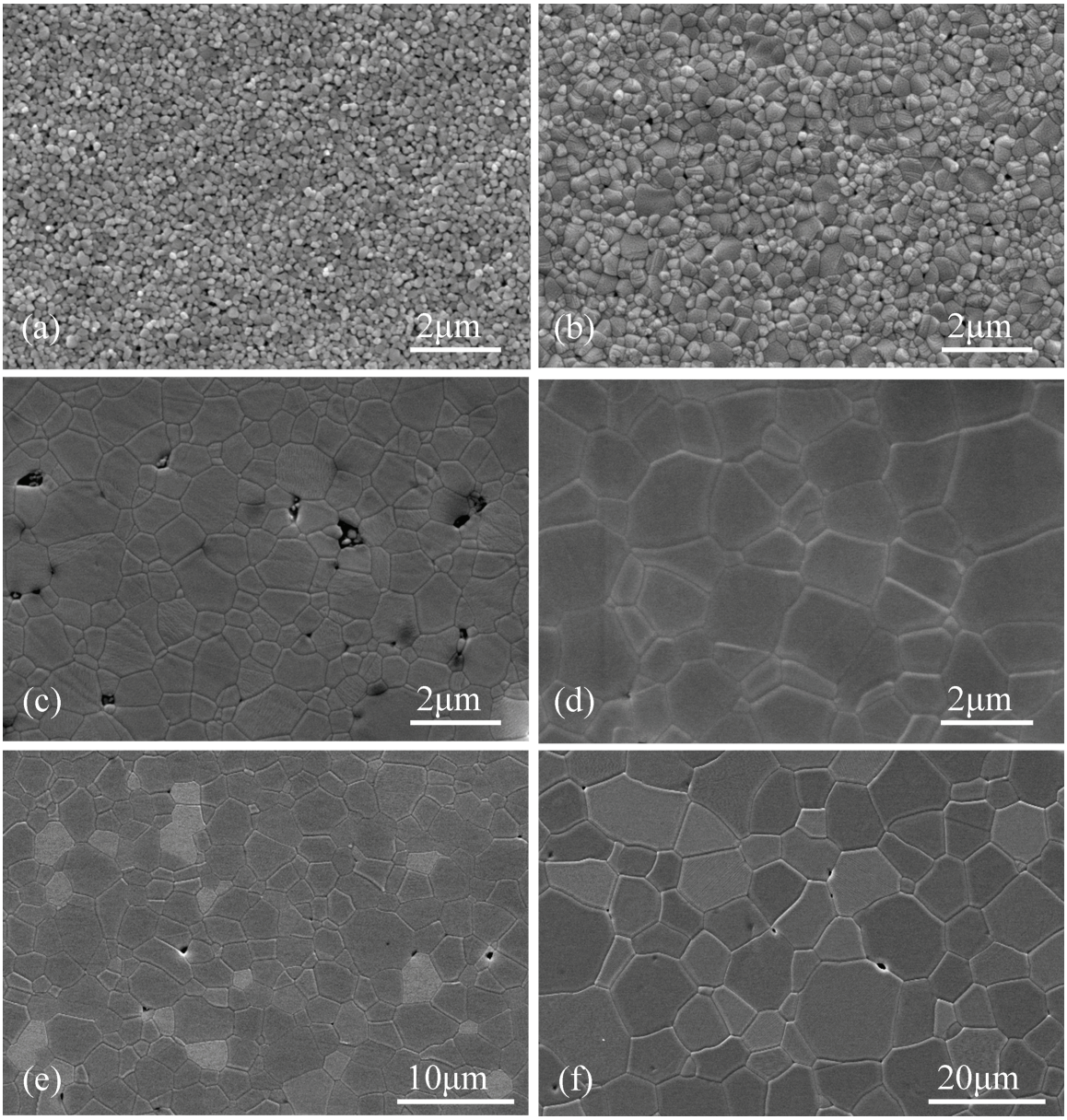

Figure 4.11: SEM images of undoped (a) 700TiO_2, (b) 800TiO_2, (c) 900TiO_2, (d) 1000TiO_2, (e) 1100TiO_2 and (f) 1300TiO_2.

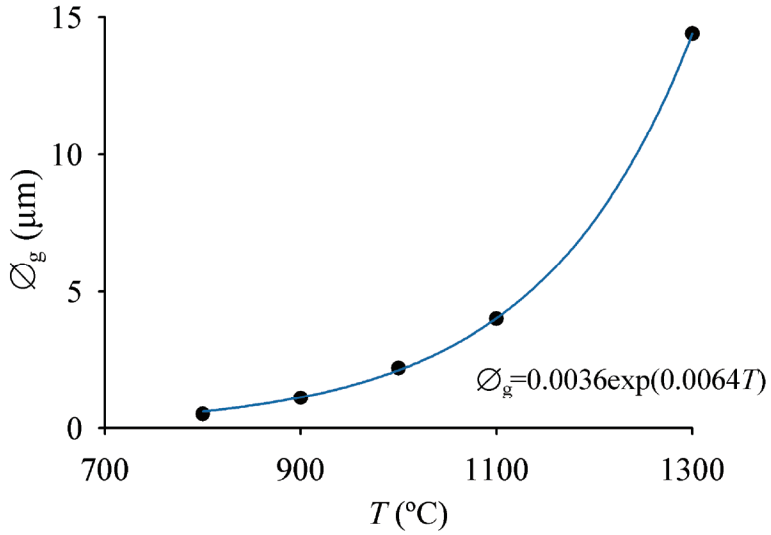

Figure 4.12: Grain growth in 800TiO_2…1300TiO_2.

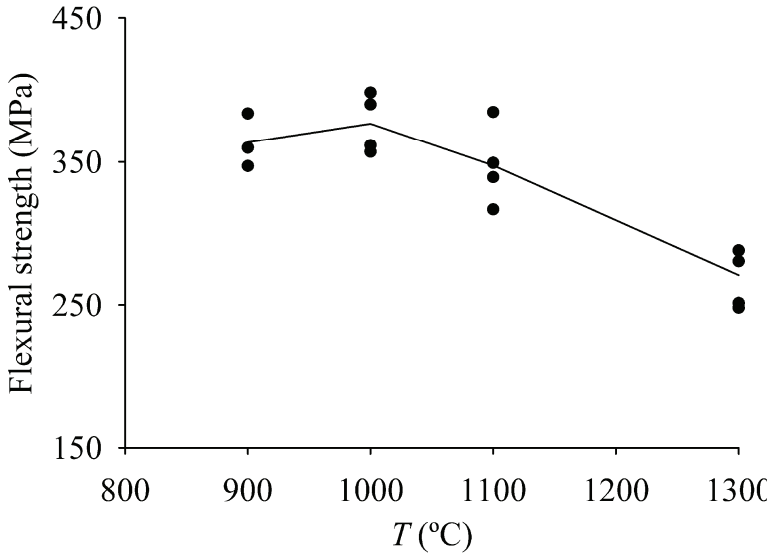

Figure 4.13: Flexural strength of sintered TiO_2. Individual measurement results are represented as dots, and the averages are connected by the line.

The flexural strength of sintered TiO_2 is shown in figure 4.13. 900TiO_2 had a high average strength of 360 MPa, ascribed to its small grain size of 1.1 μm and the presence of crack-growth inhibition from residual pores ($\phi_p = 3.7\%$). A maximum strength of

400 MPa was observed for 1000TiO_2, higher than the 300MPa previously reported [62]. This high strength was attributed to a high relative density of 99.5±1.1%, a smaller grain size of 2.2 μm, and homogeneous microstructure. As the sintering temperature increased from 1000ºC to 1300ºC, the flexural strength decreased by 100 MPa as a result of an increasing average grain size from 2.2 μm to 14.4 μm, as well as an increased porosity from 0.5% to 1.7%.

T (ºC)	ρ_r (%)	ε_r'	tan δ ($\times 10^{-4}$)
900±10	96.3±1.2	110±1	1.852±0.002
950±10	98.2±1.2	113±1	1.678±0.002
1000±10	99.5±1.1	115±1	1.408±0.002
1100±10	98.6±2.0	115±1	1.384±0.002
1300±10	98.3±2.0	115±2	1.287±0.002

Table 4.1: Measured dielectric properties of sintered TiO_2 samples.

In-cavity measurements at 6.3…6.4 GHz for 900TiO_2…1300TiO_2, revealed a dielectric constant increasing from 110 to 115, and a tan δ decreasing from 1.8×10^{-4} to 1.3×10^{-4}, as shown in table 4.1. A tan δ of 1.3×10^{-4} is 8 times lower than the value reported for undoped TiO_2 prepared by sintering of pressed pellets [18] (after the difference in measurement frequencies was corrected using equation (2.23)). Some other reported tan δ data, for example in [34,63], were not taken into comparison because non-cavity measurement was used with less accuracy. A dielectric constant of 115 is, to our best understanding, the highest ever reported for polycrystalline TiO_2 ceramics, which can be ascribed to the near-theoretical density. The measurement frequency of 6.4 GHz was higher than that used to obtain the values reported earlier [18,34], and losses tend to increase proportionally with microwave frequencies [64]. Compared with 1000TiO_2 and 1100TiO_2, 1300TiO_2 was found to have a slightly lower tan δ. However, this was offset by its much larger grain size and lower mechanical strength. The dielectric properties of

sintered TiO_2 with $\rho_r < 96\%$ were not measured because their relatively large porosity resulted in a lower permittivity, and a higher tan δ due to energy dissipation by polar species or contamination absorbed on the pore surface. The dielectric losses found in this study can be ascribed to defects and impurities on the grain boundaries, random-orientation of larger grains and residual pores.

In summary, the optimum structure for MW applications is the dense TiO_2, compacted as described and sintered at 1000ºC. It has a homogeneous microstructure, a small grain size of 2.2 μm, a high flexural strength of 400 MPa and a low dielectric loss of 1.4×10^{-4} at 6.4 GHz. Both the sintering temperature and room temperature dielectric loss are the lowest among all the reported values for commercial undoped TiO_2 samples. The homogeneous microstructure of the porous $700TiO_2$ was utilized to prepare homogeneous cation doping in TiO_2 by gel-assisted infiltration, which will be discussed in the following section.

4.3 Al doped polycrystalline TiO_2

4.3.1 Introduction

Cation doping has been widely used in TiO_2 (both rutile and anatase) to tailor its defect chemistry and hence electric and photo-catalytic properties [18,65-69]. For example, dielectric losses were in polycrystalline TiO_2 rutile decreased by Al^{3+} or Zn^{2+} doping [18]. The possible defects in TiO_2 include O vacancies, Ti interstitials and vacancies, extrinsic defects (due to dopants), electrons and holes. Ti interstitials dominate in extremely reduced atmosphere in which the oxygen partial pressure $p_{O_2} \ll 1$ Pa. Ti vacancies form at temperatures above 1300ºC, $p_{O_2} \sim 0.1$ MPa and long time dwelling [70,71]. Under common sintering conditions, such as those described in Chapter 4.2.1, the dominant intrinsic defect is O vacancy. For simplicity, only double-charged O vacancy is considered.

$$\begin{aligned} O_O^{\times} &\rightleftharpoons \frac{1}{2}O_2(g) + V_O^{\bullet\bullet} + 2e' \\ K_r &= (p_{O_2})^{\frac{1}{2}}[V_O^{\bullet\bullet}][e']^2 \end{aligned} \tag{4.5}$$

As a result, undoped TiO_2 generally behaves as a n-type semiconductor [19,70-73]. Decrease in dielectric losses by Al^{3+} doping can be explained by examining the defect chemistry. If the Al dopant substitutes for a normal Ti position

$$\begin{aligned} &Al_2O_3 \xrightarrow{TiO_2} 2Al'_{Ti} + 3O_O^{\times} + V_O^{\bullet\bullet} \\ &K_d = [Al'_{Ti}]^2[V_O^{\bullet\bullet}] \end{aligned} \tag{4.6}$$

The variation of $[O_O^{\times}]$ can be ignored in K_d at equilibrium. The charge neutrality condition is:

$$[Al'_{Ti}] + [e'] = 2[V_O^{\bullet\bullet}] \tag{4.7}$$

The doping concentrations in this study were considered to be high enough so that equation (4.7) is simplified to

$$[Al'_{Ti}] = 2[V_O^{\bullet\bullet}] \tag{4.8}$$

Combine equation (4.5) and (4.8)

$$[e'] = (2K_r)^{\frac{1}{2}}(p_{O_2})^{-\frac{1}{4}}[Al'_{Ti}]^{-\frac{1}{2}} \tag{4.9}$$

Assume all Al occupies Ti sites, therefore $[Al'_{Ti}] = [Al]$ and

$$[e'] \propto [Al]^{-\frac{1}{2}} \tag{4.10}$$

at a fixed temperature and oxygen pressure. As a result, the "free" electron concentration and dielectric loss can be reduced by acceptor-doping of Al^{3+}. Other acceptor-dopants, such as Cr^{3+}, were found to result in a n-p transition regime in TiO_2, where the conductivity contributions from electrons and holes were similar and the lowest conductivity was observed [70,74]. On the contrary, donor-doping in TiO_2, such as Nb^{5+}, always leads to increased n-type semi-conductivity [68,73,75].

Popular doping methods include solid-state cofiring of dopant oxides and TiO_2 powders [18,65], impregnation of dopant solutions in TiO_2 powders [18,66], infiltration of dopant solutions into a porous TiO_2 matrix [76], coprecipitation, hydrothermal and sol-gel synthesis of dopant salts/alkoxides together with titanium salts/alkoxides [67-69]. Such

doped TiO_2 has been reported to possess improved material properties, but with little discussion on the homogeneity of doping concentration or microstructure. Inhomogeneous doping would introduce microstructural variations, and possibly affect the actual overall material properties. In addition, despite their popularity, the above methods have drawbacks such as the requirement of high sintering temperatures in solid-state cofiring, possible change in the colloidal properties of TiO_2 powders by impregnation, the need of a very homogeneous microstructure for infiltration, and a requirement of similar precipitation/hydrolysis conditions for the dopant and titanium precursors (coprecipitation, hydrothermal and sol-gel synthesis). Here the infiltration method is considered to be the most suitable since homogeneous porous TiO_2 compacts are already available [59], which are expected to result in homogeneous distribution of dopants. Porous TiO_2 compacts were prepared from filtration of colloidally-stabilized TiO_2 suspensions, followed by low temperature calcination, as discussed in Chapter 4.2.1. The processing behavior of the infiltration solution plays an important role in the distribution of cation dopants. During solvent removal, the infiltration solution will experience a higher capillary force at smaller pores than bigger pores. Therefore simple precursor solutions would be continuously drained from bigger pores and concentrated in smaller pores [47]. To resolve this problem, we prepared dopant cation solutions with citric acid (CA) and ethylene glycol (EG), which form stable gel at a low temperature and hence immobilize dopant cations (Pechini method [31]) during solvent removal and subsequent debindering [55]. This gel-assisted infiltration method as described was used for homogeneous Al-doping in TiO_2.

4.3.2 Experimental Procedure

Infiltrating solution

$Al(NO_3)_3 \cdot 9H_2O$ (99.997%), and citric acid (CA, ≥99.5%) were obtained from Sigma-Aldrich, and ethylene glycol (EG, >99%) was obtained from Alfa Aesar. Solutions of CA and EG were first prepared to determine a proper concentration for infiltration. Three concentrations were studied: an aqueous solution of 1.0 mol/L CA and 1.4 mol/L EG (CAEG1), an aqueous solution of 3.5 mol/L CA and 5.0 mol/L EG (CAEG3), and a mixture of 5.0 mol/L CA and 7.5 mol/L EG (CAEG5). This led to a choice for CAEG3

as the infiltrating medium for $Al(NO_3)_3$. The concentration of Al^{3+} ($c_{Al^{3+}}$) in the infiltrating solution was calculated from the porosity (ϕ_p) in $700TiO_2$ and the targeted doping concentration [Al] (x ppm). In a perfect doping procedure, the total amount of Al^{3+} in the infiltrated solution equals to that of the eventual Al present in TiO_2 after sintering. Therefore $c_{Al^{3+}}$ in mol/L is

$$c_{Al^{3+}} = \frac{\rho_{TiO_2}}{M_{TiO_2}} \cdot \frac{1-\phi_p}{\phi_p} \cdot x \cdot 10^{-3} \tag{4.11}$$

where the molecular weight of TiO_2 (M_{TiO_2}) is 79.87 g/mol, and the density of TiO_2 rutile is 4.25 g/cm^3. Three doping concentrations of around 300, 600 and 1200 ppm were studied; the corresponding $c_{Al^{3+}}$ were calculated and prepared to be 0.03, 0.06 and 0.12 mol/L respectively in CAEG3. For comparison of the doping quality using an Al^{3+}-CAEG3, a 0.12 mol/L $Al(NO_3)_3$ aqueous solution (Al^{3+}-H_2O) was prepared, targeting a 1200 ppm doping concentration.

Infiltration procedure

The weight of the $700TiO_2$ compact was used to obtain the pore volume and expected weight gain after a thorough infiltration of the Al^{3+} solution. Al^{3+}-CAEG3 or Al^{3+}-H_2O solution infiltrated from one side of $700TiO_2$ at room temperature (r.t.) until the actual weight gain of the infiltrated $700TiO_2$ matched the expected value. The compact was covered for 2 hours to avoid water evaporation while the solution was penetrating into $700TiO_2$. After confirming that no solution was visible on either compact surface, the Al^{3+}-infiltrated $700TiO_2$ was heated at 120ºC overnight (~12 hours). A step-wise thermal treatment was thereafter carried out for organics removal and sintering: 0.2ºC/min heating to 450ºC, 5ºC/min heating to 900ºC…1300ºC and dwelling for 10 hours, followed by 5ºC/min cooling to r.t. An oxygen restore was carried out in air for pure and Al-doped $1000TiO_2$ and $1300TiO_2$ at 900 and 1100ºC respectively for 50 hours.

The average pore size of $700TiO_2$ was measured using gas adsorption/desorption isotherms with a Micromeritics ASAP 2020 Surface Area and Porosimetry analyzer [47]. During adsorption, physical gas adsorption first occurs onto the external surface as well

as the pores; as the gas pressure increases, the gas starts to condense within the pores. In desorption the reverse process takes place. The two mechanisms should be both considered during the pore size calculation: (a) physical adsorption on the pore walls and (b) capillary condensation in the inner capillary volume. It is assumed that the porous material has cylindrical pores with an average radius of $\overline{r}_p$, and that the adsorption layer thickness is $\overline{t}_{ad}$. Hence the actual radius of the inner cylinder is $\overline{r}_c = \overline{r}_p - \overline{t}_{ad}$, which can be calculated from the Kelvin equation

$$\ln \frac{p}{p^0} = \frac{-2\gamma_{LV} V_L \cos\theta}{RTr_c} \tag{4.12}$$

where p^0 is the saturation gas pressure of the liquid having a plane surface, γ_{LV} is the surface tension of the liquid-vapor interface, V_L is the molar volume of the liquid, θ is the contact angle between the liquid and the pore wall, R is the gas constant, and T is the absolute temperature. For liquid nitrogen which is exclusively used for gas adsorption measurement, equation (4.12) is written as

$$r_c = \frac{4.05}{\log(\frac{p^0}{p})} \text{Å} \tag{4.13}$$

A simplified Barrett-Joyner-Halenda (BJH) correction is applied, which assumes that the ratio of the inner radius to pore radius ($\frac{\overline{r}_p - \overline{t}_{ad}}{\overline{r}_p}$) is a constant [77]. In this study, desorption isotherms were obtained for p^0 to $0.6p^0$ with the simplified BJH correction to obtain the accumulated data.

The density of the CAEG3 solution was calculated from its weight and volume. The viscosity of the CAEG3 solution was measured using a simple Falling Ball Viscometer (316 Stainless Steel ball with glass tube #2, Gilmont Instrument). The contact angle of CAEG3 on a dense TiO_2 surface was measured using an EasyDrop Contact Angle Measuring Instrument (Krüss). The actual Al concentration in sintered TiO_2 was characterized by Laser Microprobe Analysis (LMA), using a New Wave™ UP193 193 nm Laser Ablation System sampling into a Thermo Finnigan Element 2 HR-ICP-MS. SEM was carried

out on as-formed 700TiO_2 surface or on thermally etched cross-sections of sintered TiO_2 with Al doping. EDAX in a Philips XL30 ESEM was used to detect any Al-rich clusters on the surface of sintered TiO_2 prepared by infiltrating Al^{3+}-CAEG3 and Al^{3+}-H_2O solutions respectively.

4.3.3 Results and discussions

700TiO_2 had a porosity of 34.0% as shown in figure 4.9 and an average pore diameter of ~45 nm from BET measurement shown in figure 4.14. The SEM image in figure 4.15 shows that 700TiO_2 has a porous and homogeneous microstructure.

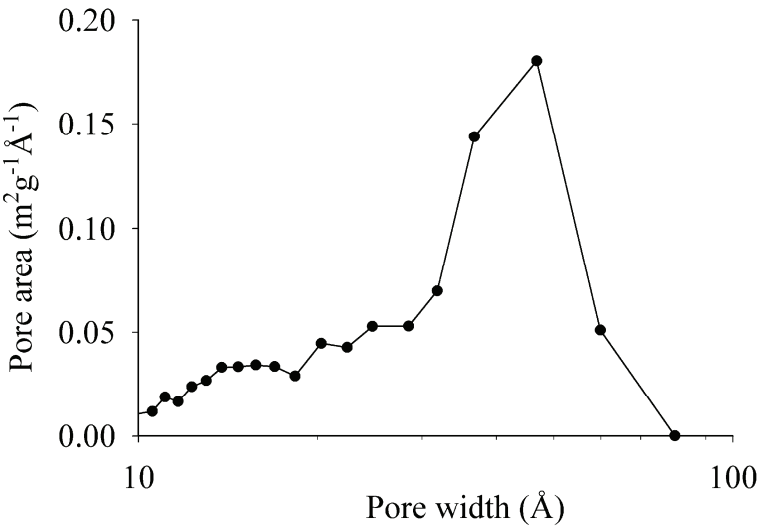

Figure 4.14: Pore size distribution in 700TiO_2 from BET measurement.

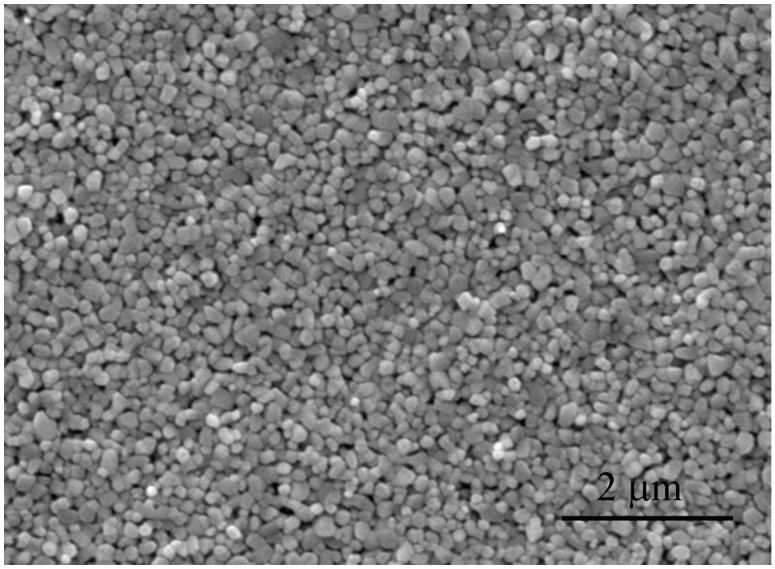

Figure 4.15: SEM image of 700TiO_2 surface.

CAEG and $Al(NO_3)_3$ solutions

The gelling temperature of CAEG1, CAEG3 and CAEG5 solutions increased from ~110ºC, ~120ºC to ~160ºC. This was attributed to the present protons (i.e. H_3O^+) that catalyzed the gelation and had a higher concentration in the most diluted CAEG solution. Most of water in the initial solution evaporated just before gelation, possibly leaving the pores in the TiO_2 compact partially filled with CAEG gel. Therefore a concentrated CAEG solution was preferred to provide a stable gel, and an effective immobilization of Al^{3+} inside the pores. After gelation, CAEG1, CAEG3 and CAEG5 had a volume shrinkage of ~70%, ~20% and <5% respectively. The nonaqueous CAEG5 solution showed little volume shrinkage after gelation, but was nonetheless not suitable for subsequent organics removal. In that case, the as-formed gel would block porous channels, inhibit H_2O and CO_x releasing during organics removal, and result in unwanted extrusion of precursor materials to the surface. CAEG3 was therefore selected as the carrier for $Al(NO_3)_3$. The density of Al^{3+}-CAEG3 was 1.31 g/ml, which was used to calculate the expected weight gain for fully infiltrated 700TiO_2.

The propagation rate of liquid penetrating into a cylindrical channel is [78]

$$\frac{dX}{dt} = \frac{(P_A + g\rho_L h + \frac{2\gamma_{LV}}{r_p}\cos\theta)(r_p^2 + 4sr_p)}{8\eta X} \tag{4.14}$$

where X is the penetration distance, P_A is unbalanced atmospheric pressure, ρ_L is the liquid density, h is the vertical distance between liquid fronts at two times, γ_{LV} is the surface tension of the liquid-vapor interface, θ is the contact angle between the liquid and the pore wall, s is the slip coefficient, r_p is the channel radius, and η is the dynamic viscosity of the liquid. Since the CAEG3 solution wets the TiO_2 surface, $s \sim 0$. In the case of capillary penetration, $P_A + g\rho_L h \ll \frac{2\gamma_{LV}}{r_p}\cos\theta$. All this implies that (4.14) is therefore simplified to

$$\frac{dX}{dt} = \frac{\gamma_{LV} r_p \cos\theta}{4\eta X} \tag{4.15}$$

Integrating both sides of (4.15) results in the penetration time (t)

$$t = \frac{2X^2\eta}{\gamma_{LV} r_p \cos\theta} \tag{4.16}$$

X was estimated from multiplying the thickness of porous 700TiO_2 compact by a typical tortuosity of 3 [47]. r_p was ~23 nm from figure 4.14. The CAEG3 solution had η of 39.9±2.0 mPa·s at room temperature, γ_{LV} of 57.1±0.4 mN/m and θ of 38.9±4.6º on dense TiO_2 compacts. Substitution of these values into (4.16) gave an estimated period of 0.8 hour for Al^{3+}-CAEG3 to completely infiltrate a 2 mm thick 700TiO_2 compact from one side. For the case of Al^{3+}-H_2O infiltration, the solution viscosity at r.t. was ~1.00 mPa·s, and the estimated infiltration time was 0.02 hour. The actual infiltration time was chosen as 2 hours to ensure a complete penetration for both Al^{3+}-CAEG3 and Al^{3+}-H_2O. When using the calculated amount of infiltration liquid, no solution was visible on either 700TiO_2 surface after 2 hours.

Sintered TiO_2 with Al-doping

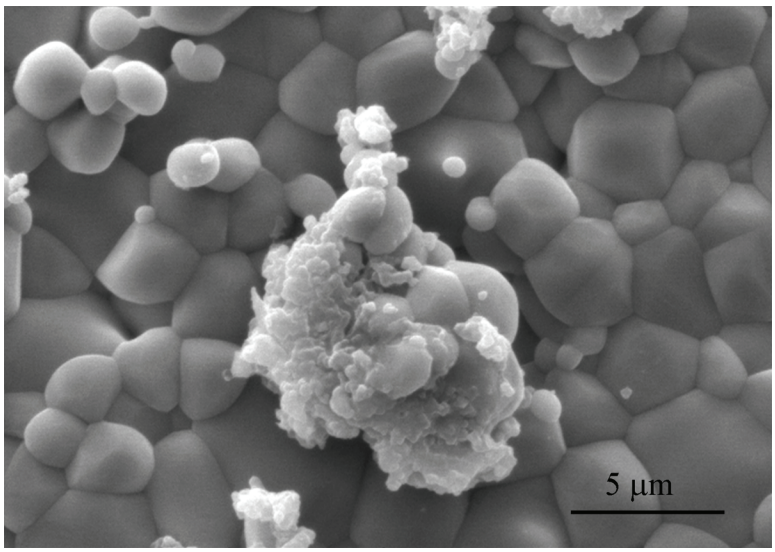

Figure 4.16: Al-rich clusters on the surface of sintered 1100TiO_2, prepared by Al^{3+}-H_2O infiltration.

Al-doped TiO_2, prepared by Al^{3+}-H_2O infiltration, was found to have with small clusters on the TiO_2 surface, as shown in figure 4.16. The actual Al concentration in these clusters was as high as ~30 at% from EDAX analysis. On the contrary, Al-rich clusters were not observed on Al-doped TiO_2 prepared with Al^{3+}-CAEG3 infiltration. The actual [Al] in dense TiO_2 (sintered at 1100ºC) was close to the targeted values, as indicated by the LMA results in table 4.2. LMA also showed a homogeneous doping level of ~1220 ppm across the sample thickness of 1200 ppm Al doped TiO_2. The homogenous doping profile, obtained after Al^{3+}-CAEG3 infiltration, is attributed to a very efficient immobilization of Al^{3+} by the CAEG gel within TiO_2 compacts. The slow rate of 0.2ºC/min between 120ºC to 450ºC was used to gradually remove H_2O and CO_x without corrupting CAEG gel or 700TiO_2 compact. In a regular Pechini synthesis, self-combustion often occurs above 100ºC in the presence of concentrated metal nitrates. However, no visible combustion occurred in $Al(NO_3)_3$-infiltrated TiO_2, mainly because of the very low concentration

of NO_3^-. During gelling and organics removal, there was no color change, or other visible changes in the TiO_2 compacts.

Target [Al]	[Al] at the upper (infiltrating) side	[Al] at the bottom side
300 ppm	350 ppm	350 ppm
600 ppm	650 ppm	620 ppm
1200 ppm	1270 ppm	1200 ppm

Table 4.2: LMA results of Al doped TiO_2, prepared with Al^{3+}-CAEG3 infiltration.

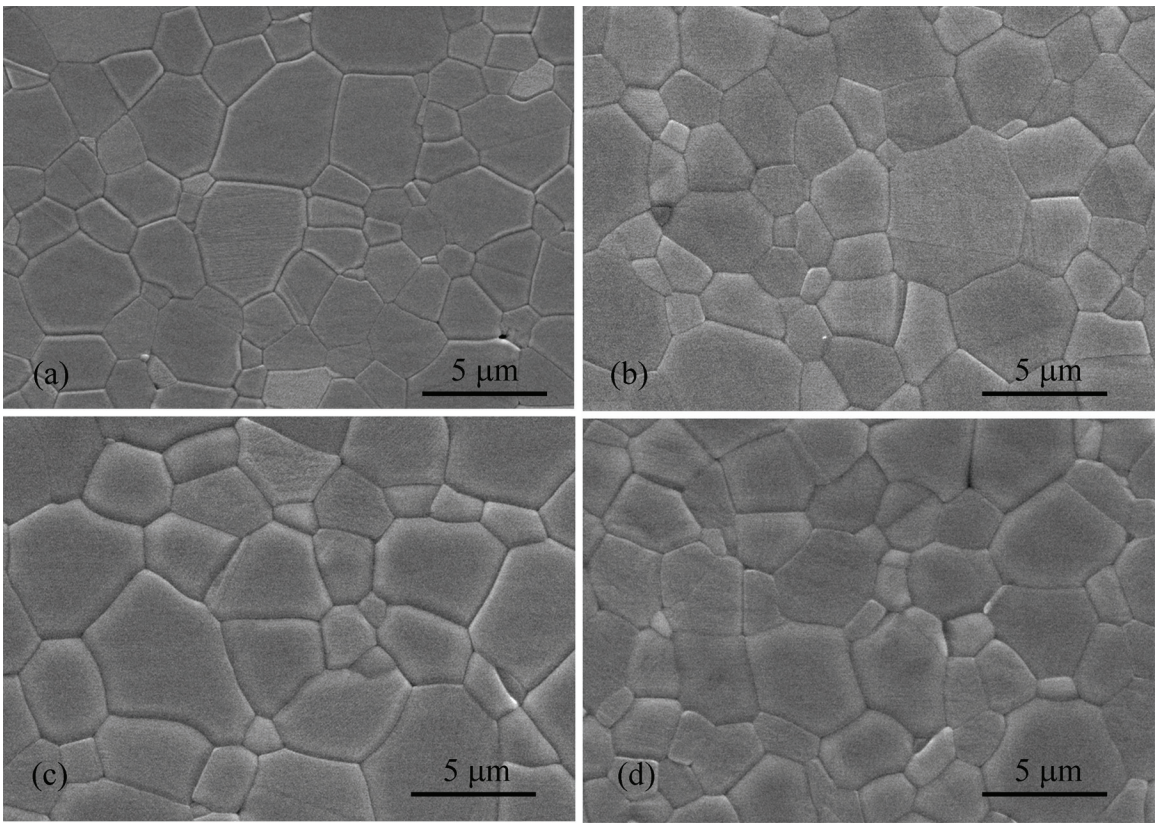

Figure 4.17: 1100TiO_2 with (a) no dopant, (b) 300 ppm Al, (c) 600 ppm Al, (d) 1200 ppm Al. All samples were polished and thermal etched.

The SEM images of dense Al-doped TiO_2 are shown in figure 4.17 and 4.18. The average grain size was found to be independent of Al concentration. The homogeneous dense microstructure was attributed to both a uniform doping, and a homogeneous microstructure of the starting porous TiO_2. For $1300TiO_2$, the undoped sample appeared to be more porous than doped samples and showed less grooving.

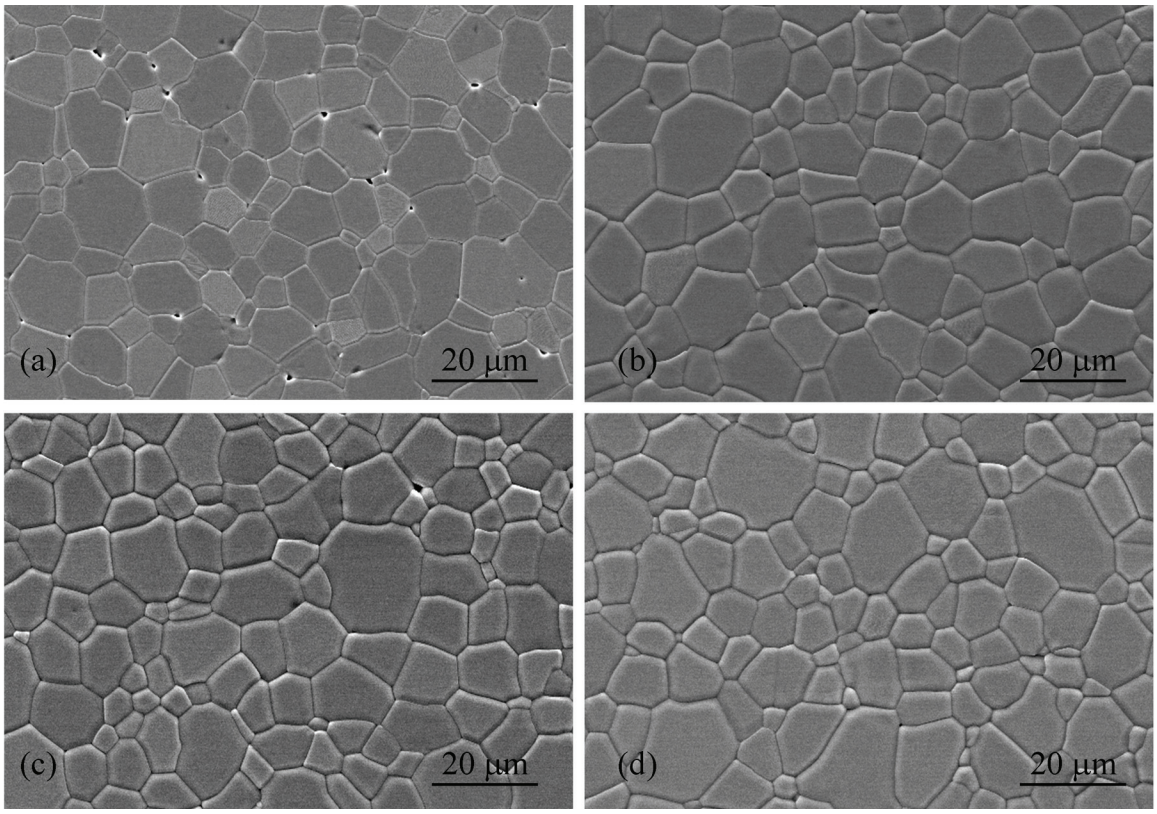

Figure 4.18: $1300TiO_2$ with (a) no dopant, (b) 300 ppm Al, (c) 600 ppm Al, (d) 1200 ppm Al. All samples were polished and thermal etched.

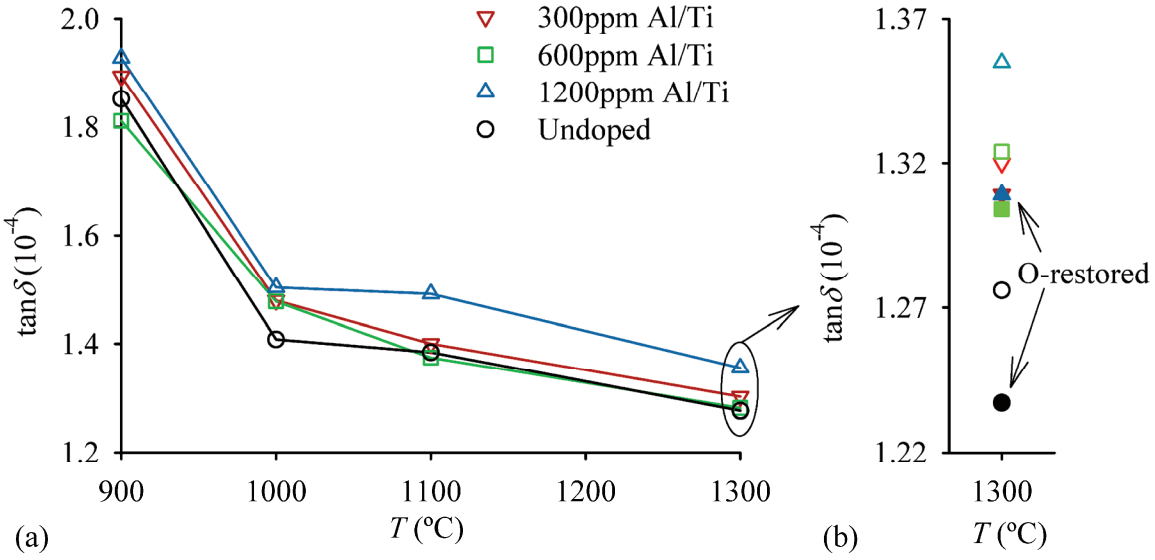

Figure 4.19: Measured dielectric loss of (a) undoped and Al doped TiO_2 before O restore, (b) undoped and Al doped 1300TiO_2 after O restore.

Figure 4.19(a) shows the measured dielectric properties of undoped and Al doped TiO_2 sintered at different temperatures. Although Al was reported to decrease tan δ by >70 times with respect to the undoped TiO_2 [18], our results showed the Al dopant did not significantly decrease the already very low tan δ values. In addition, the highest doping concentration of 1200 ppm resulted systematically in higher tan δ, for all the sintering temperatures. It was observed after oxygen restore, tan δ did not change for pure or Al-doped 1000TiO_2, but slightly decreased by ~4% in both pure and Al-doped 1300TiO_2 as shown in figure 4.19(b). It is concluded that O-restore and Al doping did not effectively reduce tan δ possibly because of an already small O reduction to be compensated. It should be noted that in [18] the use of a solid-state co-sintering at 1500ºC led to inhomogeneous microstructures and substantial grain growth. In our study, good homogeneity was maintained starting from the TiO_2 green body to the sintered TiO_2 structure, also with Al-doping. The observed loss at 6.4 GHz was equivalent to the reported best value if equation (2.23) was taken into account. Moreover, the measured ε_r' of 115 was higher than the 100-105 found mostly in the literature. This gel-assisted infiltration method is

considered to be of generic use for cation doping systems where chemical and microstructural homogeneity is critical.

4.4 Laminates of home-made α-Al_2O_3 and TiO_2

The relative high loss in the AD laminates discussed in Chapter 3 was also due to the presence of the external organic adhesive used for lamination. Here we explored lamination of α-Al_2O_3 and TiO_2 by a reactive bonding. Individual α-Al_2O_3 and TiO_2 sheets were fabricated from tape-casting as described in Appendix A. The α-Al_2O_3|TiO_2 laminates were fabricated from the two sheets, with α-Al_2O_3 as outer surfaces. This is because α-Al_2O_3 has a TEC, 1…2 ppm/K (depending on the actual temperature) smaller than that of TiO_2, and will be under compression during cooling [49,79]. The formation of an Al_2TiO_5 intermediate layer was observed when α-Al_2O_3 and TiO_2 were co-sintered at 1300ºC for 3 hours with a slight pressure of 0.25 MPa applied. This layer, as shown in figure 4.20, can be used as an intrinsic (reactive) adhesive, to replace the more lossy external adhesive. Microstructure of α-Al_2O_3 and TiO_2 was observed of less homogeneity than that in the samples prepared from colloidal processing. This can be ascribed to a low compacting capability of tape-casting process, due to the use of a relatively high amount of binders and additives.

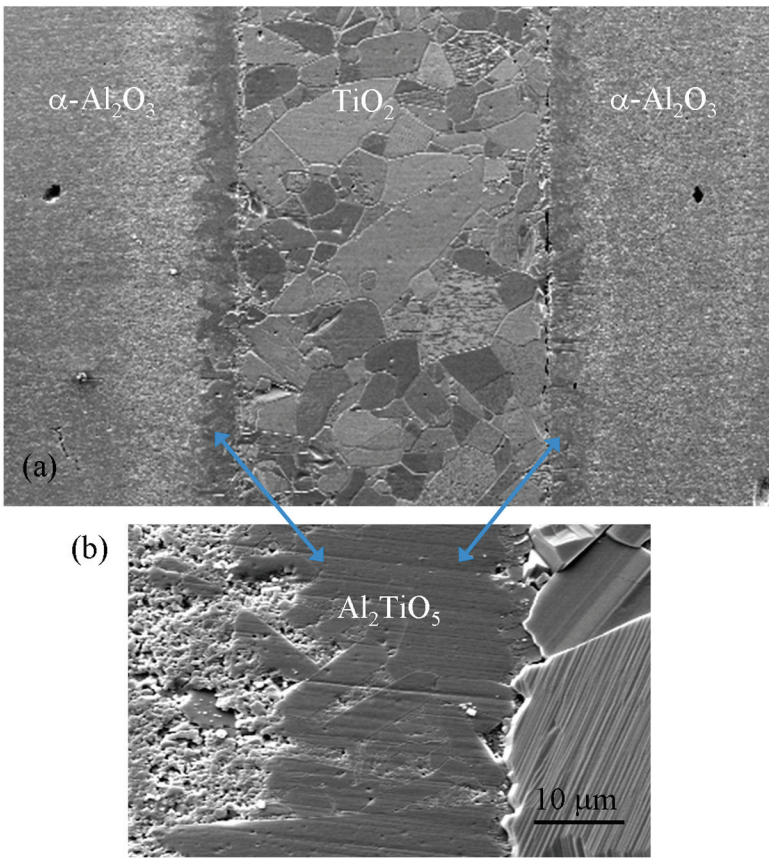

Figure 4.20: (a) cross-section of homemade α-Al_2O_3|TiO_2 laminates, sintered at 1300ºC for 3 hours. (b) Microstructure at the α-Al_2O_3 and TiO_2 interface.

Small laminates of cm dimensions were obtained intact and sustained diamond-machining; whereas larger parts tended to crack during machining. Cracking and de-lamination were a result of the dissimilar TECs of α-Al_2O_3 and TiO_2, and residual thermal stress in the laminates. They may initiate during cutting at the free edges of the bonding surface, where a highly localized stress was observed and predicted normal to the sheet plane [80-82]. Therefore, a hot-press technique should be applied to the laminates to lower the reaction temperature, reduce the residual stress and the thickness of Al_2TiO_5. An externally applied compression stress and thinner layers of α-Al_2O_3 and TiO_2 may also be favorable to avoid crack formation.

CHAPTER 5

MAGNETIC MATERIALS FOR MICROWAVE FREQUENCIES

Ferrimagnetic iron oxides (ferrites [6]) are the most promising for applications at MW frequencies, because they combine the properties of a magnetic material with that of an electrical insulator [7]. Ferrites have a much higher electrical resistivity than metallic ferromagnetic materials, resulting in minimization of eddy current losses, and total penetration of the EM field. Furthermore, the widespread use of ferrites rests upon a remarkable flexibility in tailoring the magnetic properties, ease of preparation, and a favorable cost price. Hence ferrites are frequently applied as circuit elements, magnetic storage media like read/write heads, non-reciprocal and non-linear devices, such as phase shifters and Faraday rotators. The electromagnetic properties of ferrites are affected by operating conditions such as field strength, temperature and frequency. Generally, ferrites have relatively low Curie temperatures (T_C), at which ferrimagnetic materials become paramagnetic. Also due to their magneto-crystalline anisotropy, the frequency range of some ferrites is limited by the occurrence of transverse ferrimagnetic resonance (FMR), the so called Snoek's limitation [83]. Therefore, magnetic losses and thermal stability in ferrites need particular attention.

Ferrites include a wide range of materials with various crystal structures, compositions and applications. In this chapter, a short literature survey is presented about specific types of ferrites, which can be applied at the MW range with low losses. First of all, the

crystal structures and basic ferrimagnetisms were reviewed. Then, the fundamental magnetic behaviors and limitations are discussed, as well as possible technical solutions. This is followed by a summary of preparation methods for bulk, film and granular ferrites with a few typical examples of the latest developments. Ca,V,Zr-substituted yttrium-iron garnets, as an example of low-loss ferrites, will be discussed since they are considered for the ferrimagnetic component for MPAs antennas as discussed in Chapter 1.1 [12]. Reduction of both magnetic and dielectric losses is expected to be attainable by careful control of chemical compositions and ceramic fabrication routes.

5.1 Intrinsic properties of ferrites

Commonly used ferrites are classified into three types: spinels, hexagonal ferrites and garnets, according to their primary crystal lattice. Generally, ferrimagnetism arises from the antiparallel alignment of the magnetic moments on transition metal ions, present on different magnetic sublattices. The origin of the antiparallel coupling can be explained by super-exchange of valence electrons between the filled *p*-orbitals of O^{2-} and unfilled *d*-orbitals of the transition metal cations. In ferrites, the oppositely directed magnetic moments do not exactly cancel, thus a net magnetic moment results [5,6,84].

5.1.1 Spinels

Spinels have the general formula $MeO{\cdot}Fe_2O_3$, where *Me* represents a divalent transition ion or a combination of ions having an average valence of two [6]. In spinel ferrites, the relatively large oxygen anions form a cubic close packing with ½ of the octahedral and ⅛ of the tetrahedral interstitial sites occupied by metal ions. Figure 5.1 shows a cubic unit cell containing eight formula units, in which tetrahedral and octahedral sites are labeled as A and B respectively. The distribution of cations over A- and B-sites is determined by their ionic radius, electronic configurations and electrostatic energy in the spinel lattice [6]. Cations like Zn^{2+} and Cd^{2+}, show a marked preference for the A sites, thus their spinels are obtained with a formula $Me^{2+}[\,Fe_2^{3+}\,]O_4$, where the Fe^{3+} ions between brackets are on the B-sites. When cations have a stronger B-site preference than Fe^{3+}, as is the

case for Mn^{2+}, Ni^{2+} and Co^{2+}, Fe^{3+} can occupy A-sites to form inverse spinels, denoted as $Fe^{3+}[Me^{2+}Fe^{3+}]O_4$.

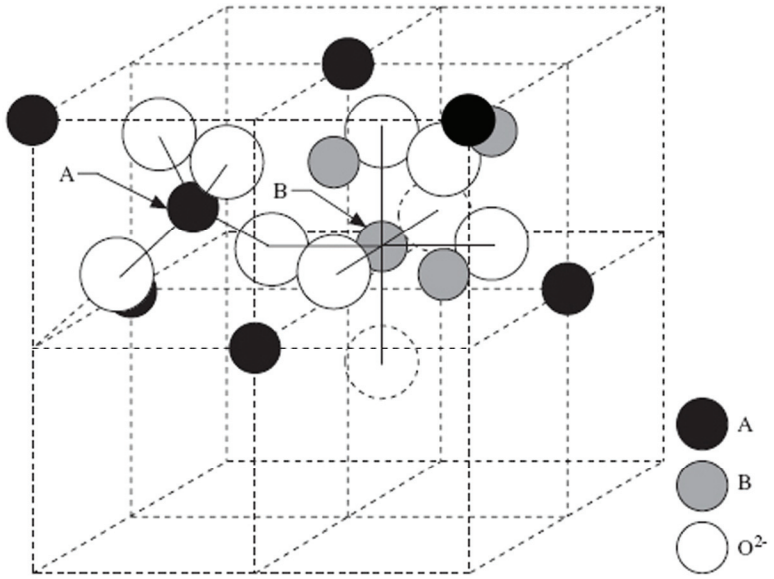

Figure 5.1: Two octants of a spinel unit cell. A and B represent tetrahedrally and octahedrally coordinated sites respectively [85].

The spinel crystal structure can be considered in terms of A-site and B-site magnetic sublattices. In the Néel model of ferrimagnetism, there are three super-exchange interactions: A-A, B-B and A-B, which are all antiferrimagnetic. The A-B interaction has the greatest exchange energy, primarily due to the small cation-O^{2-} bond length and the favorable cation-O^{2-}-cation bonding angle [6]. The dominance of the A-B interaction results in antiparallel alignment between the magnetic moments in the two types of sublattices, and also parallel alignment of the cations within each sublattice, despite the A-A or B-B antiferrimagnetic interaction. Therefore in the ideal inverse spinel structure, the spin moments of Fe^{3+} on B-sites cancel out with those of Fe^{3+} on A-sites. The net magnetization of the solid is ascribed to the uncompensated magnetic moments from all the divalent ions at B-sites.

The best magnetic properties are obtained with mixed spinels, which contain more than one divalent cation, such as NiZn and MnZn spinels. The substitutions influence the degree of the inversion, the strength of the super-exchange, the magnetic moment, and T_C. For examples:

- the saturation magnetization ($4\pi M_s$) of MgMn spinel can be varied from 95 to 223 KA/m (1200 to 2800 G), depending on the degree of inversion, in turn depending on the sintering conditions [7],
- addition of Zn^{2+} at A-sites increases M_s, but reduces T_C [6],
- small amounts of Co^{2+} reduce the crystal anisotropy, because the anisotropy of Co partly compensates that of Fe [5,6].

5.1.2 Hexagonal ferrites

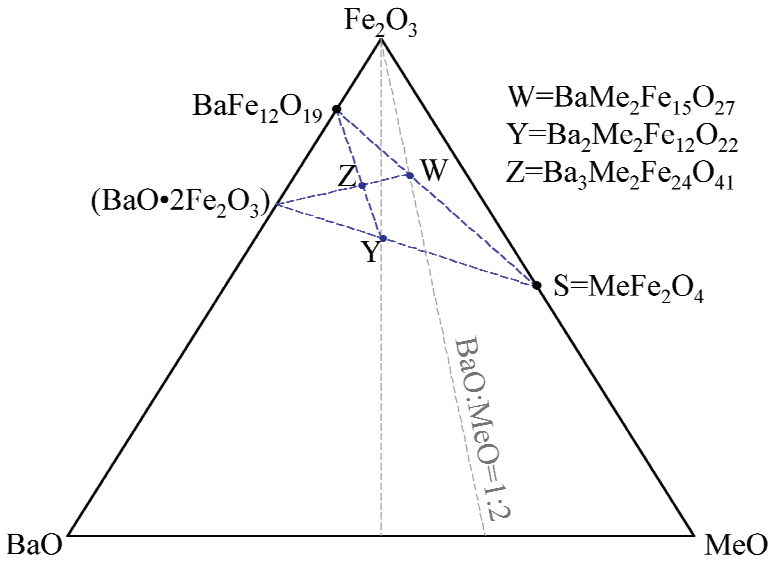

Figure 5.2: Composition diagram of ferrites, indicating hexagonal ferrite phases: M, W, Y, and Z, and spinel S, after [6].

The group of ferrites possessing hexagonal crystal structures is referred as hexagonal ferrites or hexaferrites. Four types of hexagonal ferrites are distinguished and indicated as

M, W, Y and Z as shown in the composition diagram in figure 5.2. They correspond to (BaO+*Me*O)/Fe_2O_3 ratios of 1:6, 3:8, 4:6 and 5:12 respectively. *Me* can be a transition metal cation or a combination of cations as it would occur in spinels. The crystal and magnetic structure of the different types of hexagonal ferrites are remarkably complex, as shown for the most important M-type $BaFe_{12}O_{19}$ in figure 5.3. The M-type unit cell contains 10 oxygen layers, sequentially constructed from 4 blocks, S (spinel), R (hexagonal), S* and R*. S* and R* have equivalent atomic arrangements as S and R, but are rotated 180° about the c axis with respect to S and R. An S or S* block consists of two O^{2-} layers; while an R or R* block contains three O^{2-} layers, with one oxygen position in the middle layer replaced by a Ba^{2+} ion [86].

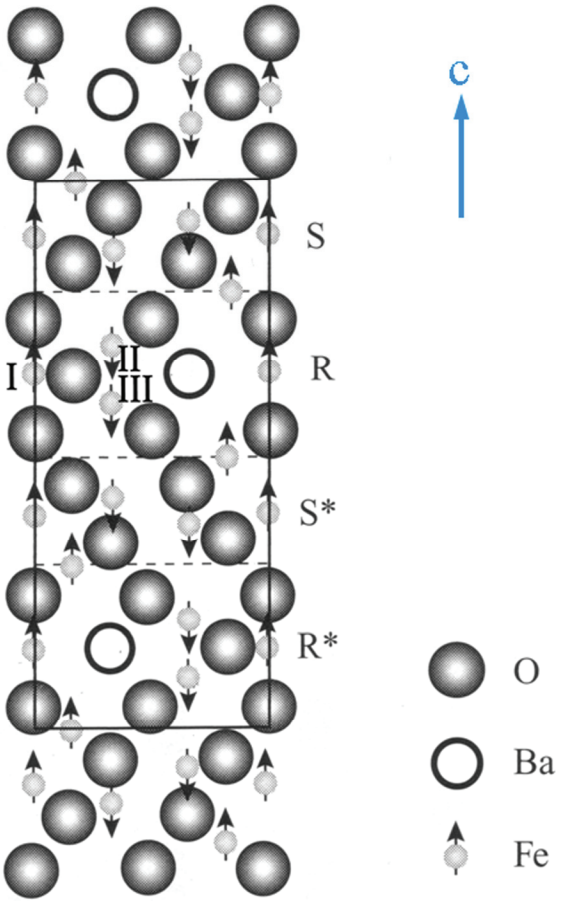

Figure 5.3: Structure of M type $BaFe_{12}O_{19}$ [86].

Each block in the M-type hexagonal ferrite has 6 interstitial Fe^{3+} ions in 3 different types of lattice sites, having parallel or opposite spin directions, as listed in table 5.1. In the R or R* block, the super-exchange interactions force Fe^{3+}(I) to be aligned antiparallel with Fe^{3+}(II) and Fe^{3+}(III), whereas the latter two are parallel to each other, as shown in figure 5.3. These strongly preferred alignments are imposed on the adjacent S and S* blocks, and account for the uniaxial magnetization anisotropy of the crystal along the c axis [5]. The entire unit cell has a net magnetic moment of 20 μ_B, in which the Bohr magneton μ_B is the magnetic moment produced by one unpaired electron.

Sub-block	**Tetragonal**	**Octahedral**
S and S*	↓↓	↑↑↑↑
R and R*	-	↑↑↑↓↓

Table 5.1: Types of lattice sites and spin directions of interstitial Fe^{3+} ions in S, S* R and R* blocks [86].

5.1.3 Garnets

The general formula for garnets is $Re_3Fe_5O_{12}$, where *Re* is one of the rare earth metal ions, including Y, La and Gd. The cubic unit cell contains 8 formula units or 160 atoms, which can be described as a spatial arrangement of 96 O^{2-} with interstitial cations. A well-known garnet, yttrium iron garnet $Y_3Fe_5O_{12}$ (YIG) is shown in figure 5.4. The coordination of the garnet cations is considerably more complex than that in spinels, with 24 Y^{3+} in dodecahedral (12-coordinated) sites, 24 Fe^{3+} ions in tetrahedral sites and the remaining 16 Fe^{3+} in octahedral sites. Like in spinels and hexagonal ferrites, a wide range of transition metal cations can substitute Y^{3+} or Fe^{3+}; especially rare earth ions may replace the ions on octahedral and dodecahedral sites. The cation site distribution in garnets is normally represented by grouping between { }, [ ], ( ) for dodeca-, octa- and tetrahedral sites respectively, and hence YIG can be written as $\{Y_3\}[Fe_2](Fe_3)O_{12}$. A substituted YIG can be written as $\{Y_{3-x}Me_x^{l+}\}[Fe_{2-y}Me_y^{m+}](Fe_{3-z}Me_z^{n+})O_{12}$, in which Me^{l+}, Me^{m+} and Me^{n+} are different substitution cations. Chemical stoichiometry leads to the relation

of $3(x+y+z) = xl + ym + zn$. The substitution is not fully random, as each type of lattice site will accept specific metal ions with a suitable size: 0.9…1.05 Å at dodecahedral sites, 0.65…0.8 Å at octahedral sites and 0.4…0.64 Å at tetrahedral sites [29]. For example, pentavalent ions such as V^{5+} and As^{5+} occupy tetrahedral sites, while Ca^{2+} substitutes on dodecahedral sites [87].

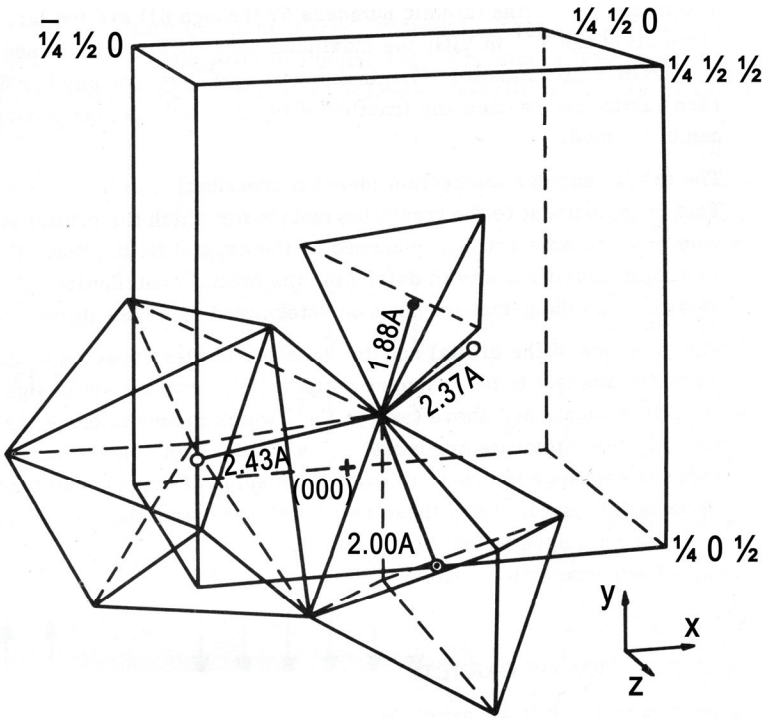

Figure 5.4: Unit cell structure of YIG, showing cation coordination structure [84]: Fe^{3+}(⊙) on tetragonal sites, Fe^{3+}(●) in octahedral sites and Y^{3+}(○) on dodecahedral sites.

In YIG, Y^{3+} with no 4*f* electrons does not have a magnetic moment; three Fe^{3+} ions on tetrahedral sites align antiparallel with two Fe^{3+} on octahedral sites. The dominant antiferromagnetic exchange between these two types of Fe^{3+} results in a net magnetic moment of 5 μ_B per formula unit. In case Re^{3+} has a permanent magnetic moment, the Re^{3+} ions form a third magnetic sublattice. At low temperatures, the overall magnetization is parallel to that of Re^{3+}; whereas at increased temperatures, Re^{3+} behaves paramagnetically

in the exchange field produced by the strong Fe^{3+} coupling [87]. Therefore, a compensation temperature will be observed in the magnetization curve, when the sign of the spontaneous magnetization reverses. The magnetic properties of YIG can be tailored over a very wide range, as all three different crystallographic sites are available for substitutions by different metal cations with various valence states. For instance, Sc substitutions at octahedral sites raise $4\pi M_s$ up to 151 KA/m (1900 G); whereas Al or Ga substitutions at tetragonal sites can lower $4\pi M_s$ to 24 KA/m (300 G).

5.2 Relevant theory of magnetism

MW applications of ferrites are based on the unique interactions of MW radiation with ferrites. These high frequency properties depend on the motion of magnetic dipoles in the presence of a constant magnetic field and a superimposed MW magnetic field. Here we discuss the magnetic behavior of ferrites in a static field, and followed by a discussion of MW field response.

5.2.1 Ferrites in a static field

If a magnetic material is in a static magnetic field **H**, the magnetic induction inside the ferrite **B** is calculated by (in SI unit)

$$\mathbf{B} = \mu_0(\mathbf{H} + \mathbf{M}) \tag{5.1}$$

where μ_0 is the permeability of free space and **M** is the magnetization inside the ferrite. The magnetization depends on the external field and materials properties, with the latter determined by both individual magnetic moments of the constituent particles and the interactions between each other. The magnetization is related to the field by

$$\mathbf{M} = \chi_m \mathbf{H} \tag{5.2}$$

where χ_m is the magnetic susceptibility, which represents that extent of material response to an applied magnetic field. From equation (5.1) and (5.2), the permeability is defined as

$$\mu = \frac{\mathbf{B}}{\mathbf{H}} = \mu_0(1 + \chi_m) = \mu_0\mu_r \tag{5.3}$$

where μ_r is the relative permeability. The magnetization curve, i.e. a plot of M vs H, is often used to represent the magnetic behavior of ferrites in a static field. As shown in figure 5.5, the curve (from $0 \rightarrow M_s$) can be sub-divided into three major regions: ($0 \rightarrow$a) the initial susceptibility region where reversible domain wall movements and rotation occur, (a→b) where irreversible domain wall motion occurs, and (b→M_s) where the irreversible magnetization rotation occurs. M is effectively constant above saturation, and the entire M vs H curve forms a hysteresis loop.

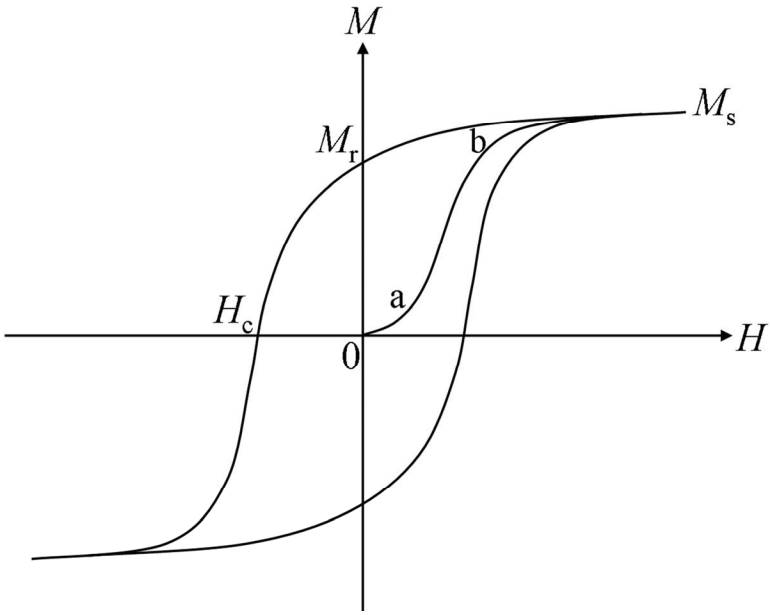

Figure 5.5: A typical hysteresis loop of a ferrite. M_r, M_s, and H_c are the remanence, saturation magnetization, and coercivity respectively.

5.2.2 Wave propagation in ferrites

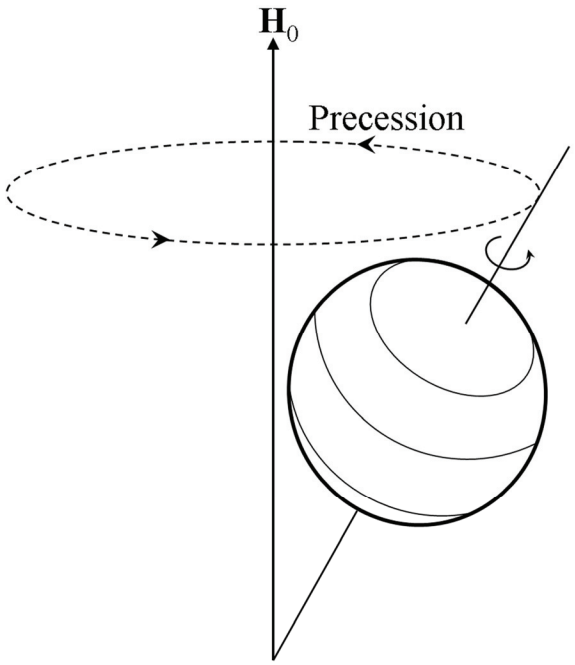

Figure 5.6: Electron precession under the influence of a static magnetic field $\mathbf{H}_0$, after [88].

The magnetization of the ferrites is primarily due to uncompensated spin moments of the electrons [6]. In a bias static magnetic field $\mathbf{H}_0$, the magnetic moment $\mathbf{M}$ precesses around the direction of $\mathbf{H}_0$ as shown in figure 5.6. The classical equation of magnetization motion, without damping, is

$$\frac{d\mathbf{M}}{dt} = \gamma_g (\mathbf{M} \times \mathbf{H}) \tag{5.4}$$

where $\mathbf{H}$ is the sum of all the magnetic fields experienced by the spinning electrons. The gyromagnetic ratio γ_g, is the ratio of magnetic moment to the angular momentum, and given by $\frac{gq_e}{2m_e c} = 35.2 \text{ Km/(A} \cdot \text{s) (SI)} = 2.8 \text{ MHz/G (cgs)}$ for free electrons. Here q_e is the absolute value of the electronic charge, m_e is the mass of the electron, c is the velocity

of light and the Landé *g*-factor equals 2 for pure spin moments. To describe the effect of MW field, it is assumed that a MW field $\mathbf{h}\exp(\mathrm{j}\omega t)$ is superimposed on and propagates parallel to $\mathbf{H}_0$ along the *z*-axis, with an amplitude much smaller than that of $\mathbf{H}_0$. The overall magnetic fields can be expressed as

$$\mathbf{H} = \mathbf{H}_\mathrm{i} + \mathbf{h}\exp(\mathrm{j}\omega t) \tag{5.5}$$

where ω represents the frequency of the MW field and $\mathbf{H}_\mathrm{i}$ is the sum of the static fields within the ferrites. In addition to the external $\mathbf{H}_0$, $\mathbf{H}_\mathrm{i}$ includes the internal bias field from the magnetocrystalline anisotropy and the demagnetizing field counteracting $\mathbf{H}_0$. For an infinite medium without anisotropy, magnetostriction or imperfections, only $\mathbf{H}_0$ contributes to $\mathbf{H}_\mathrm{i}$. Therefore the spinning electrons experience a large static magnetic field along *z*-direction, and a small alternating component perpendicular to the *z*-axis. The magnetization is

$$\mathbf{M} = \mathbf{M}_0 + \mathbf{m}\exp(\mathrm{j}\omega t) \tag{5.6}$$

where $\mathbf{M}_0$ is equal to $\mathbf{M}_\mathrm{s}$ at a given temperature if the ferrite is saturated under $\mathbf{H}_0$, $\mathbf{m}$ is the magnetization caused by the MW field. Since it is assumed that $\mathbf{H}_0 \gg \mathbf{h}$, the precession remains very small and $\mathbf{M}_0 \gg \mathbf{m}$. Substitution of (5.5) and (5.6) into (5.4) results in a singularity of $\mathbf{m}$ when

$$\omega_0 = \gamma_\mathrm{g} H_0 \tag{5.7}$$

This is defined as the gyromagnetic resonance condition (in an infinite medium), at which the torque from the MW field on spinning electrons is in phase with their precessional motion in the static field. As a result, the precession amplitude increases; and energy of the MW field transfers to the spin system. The permeability tensor is formulated as

$$\boldsymbol{\mu} = \mu_0 \begin{pmatrix} \mu_\mathrm{r} & -j\kappa_\mathrm{r} & 0 \\ -j\kappa_\mathrm{r} & \mu_\mathrm{r} & 0 \\ 0 & 0 & 1 \end{pmatrix} \tag{5.8}$$

in which

$$\mu_r = 1 + \frac{\omega_0 \omega_m}{\omega_0^2 - \omega^2} \tag{5.9}$$

$$\kappa_r = \frac{\omega \omega_m}{\omega_0^2 - \omega^2} \tag{5.10}$$

The resonance frequency $\omega_m = \gamma_g 4\pi M_s$ if the ferrite is magnetically saturated. When a plane MW wave propagates parallel to the bias field, the ferrite is considered as an insulating medium with a permittivity ε and a magnetic tensor shown in (5.8). Solving Maxwell equations applied to the MW field leads to a plane wave solution in the form of $\mathbf{h} = \mathbf{h}_0 \exp(-\Gamma)$, in which Γ is the propagation constant. Two propagation constants are obtained

$$\begin{aligned} \Gamma^+ &= \frac{j\omega}{c}(\varepsilon_r \cdot \mu_r^+)^{\frac{1}{2}} \\ \Gamma^- &= \frac{j\omega}{c}(\varepsilon_r \cdot \mu_r^-)^{\frac{1}{2}} \end{aligned} \tag{5.11}$$

in which the effective permeability is

$$\begin{aligned} \mu_r^+ &= \mu_r + \kappa_r \\ \mu_r^- &= \mu_r - \kappa_r \end{aligned} \tag{5.12}$$

The positive and negative signs correspond to the two oppositely circularly-polarized waves resolved from the linearly polarized plane MW wave. Since $\kappa_r \neq 0$, $\mu_r^+ \neq \mu_r^-$ and $\Gamma^+ \neq \Gamma^-$. In particular, μ_r^+ goes into resonance, whereas μ_r^- is weakly influenced. Therefore one hand of polarization wave travels faster and rotates more than the opposite hand over a fixed length. When these two circular polarized waves are recombined to a plane wave, the polarization direction is rotated with respect to that in the incident wave. This is known as the Faraday rotation (FR) of MW in ferrites.

In reality, magnetic relaxation occurs, as the energy of the uniformly processing spin system transfers into lattice vibrations and finally dissipates as heat. The energy loss can be expressed as the imaginary components in (5.9) and (5.10)

$$\mu_r^* = \mu_r' - j\mu_r'' \tag{5.13}$$

$$\kappa_r^* = \kappa_r' - j\kappa_r'' \tag{5.14}$$

$$\begin{aligned} \mu_r^+ &= \mu_r^* + \kappa_r^* = \mu_r'^+ - j\mu_r''^+ \\ \mu_r^- &= \mu_r^* - \kappa_r^* = \mu_r'^- - j\mu_r''^- \end{aligned} \tag{5.15}$$

in which μ_r', μ_r'', κ_r', κ_r'', $\mu_r'^{\pm}$ and $\mu_r''^{\pm}$ are functions of γ_g, ω, M_0, H_0 and the relaxation processes. The complex propagation constants are now

$$\begin{aligned} \Gamma^+ &= \frac{j\omega}{c}(\varepsilon_r \cdot \mu_r^+)^{\frac{1}{2}} = \alpha^+ + j\beta^+ \\ \Gamma^- &= \frac{j\omega}{c}(\varepsilon_r \cdot \mu_r^-)^{\frac{1}{2}} = \alpha^- + j\beta^- \end{aligned} \tag{5.16}$$

in which α is the attenuation constant of amplitude, and β is the phase constant. The relation of $\alpha^{\pm}$, $\beta^{\pm}$, $\mu_r'^{\pm}$ and $\mu_r''^{\pm}$ with the magnitude of the applied H_0 at a fix MW frequency is shown by an example in figure 5.7.

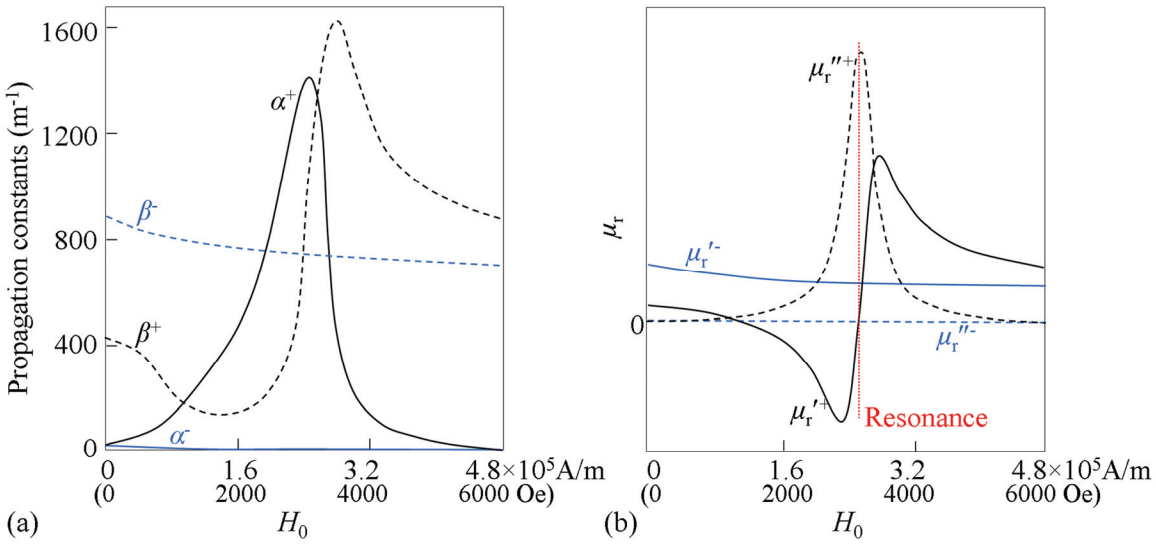

Figure 5.7: Variation of (a) the propagation constants in (5.16) and (b) the effective permeability in (5.15) with the external field H_0, after [5]. In this example, the resonance line width ΔH = 40 KA/m (500 Oe), the saturation magnetization $4\pi M_s$ = 160 KA/m (2000 G), and the MW frequency is fixed at 9 GHz.

Faraday rotation

Faraday rotation (FR) was named after M. Faraday, who discovered that the polarization plane of a linearly polarized light rotated as the light propagated through a paramagnetic liquid under an applied magnetic field. At MW frequencies, FR is also observed and the net rotation angle per unit length is expressed by the phase constants in equation (5.16), assuming no attenuation in the amplitude of both circularly polarized propagations [5].

$$\theta_F = \frac{\beta^- - \beta^+}{2} = \frac{\omega \varepsilon_r^{\frac{1}{2}}}{2c}\left[\left(1+\frac{\omega_m}{\omega_0+\omega}\right)^{\frac{1}{2}} - \left(1+\frac{\omega_m}{\omega_0-\omega}\right)^{\frac{1}{2}}\right] \tag{5.17}$$

in which θ_F is the specific FR angle (radian/m). It would be seen from figure 5.7(a) $|\beta^- - \beta^+|$ is large over a broad region below resonance, which suggests that FR-utilized devices should be operated below resonance and close to the region of the negative effective permeability, as shown in figure 5.7(b). At a small field below resonance with $\omega \gg \omega_0$ and $\omega > \omega_m$

$$\theta_F \approx \frac{\omega_m \varepsilon_r^{\frac{1}{2}}}{2c} \tag{5.18}$$

which indicates that θ_F is determined by the saturation magnetization of the ferrites. It is noteworthy that the FR direction depends on the direction of the bias field but not the propagating direction of the MW. This non-reciprocal effect has made ferrites critical components in modulators, circulators, and isolators at MW frequencies.

5.2.3 Magnetic losses and relaxation

Magnetic relaxation and losses are closely related to both intrinsic and extrinsic factors, including the crystal structure, impurities, microstructure, porosity, geometric dimensions, as well as the operating temperature, frequency and power of the MW field. In a static or low frequency magnetic field, the magnetic losses are mostly ascribed as hysteresis losses. The loss magnitude increases with a high magnetic anisotropy and magnetostriction, and can be visualized as the area within the hysteresis loop as shown in figure 5.5. The hysteresis effect indicates the energy required for domain wall movement

under a magnetic field. At high frequencies, the domain movement is not able to catch up with the alternating magnetic field, and consequently dampens. Instead, other loss mechanisms arise, including eddy current loss, domain resonance and ferrimagnetic resonance. Eddy current loss is observed especially in more conductive ferrites, such as spinels. In those materials, the conduction mechanism is primarily ascribed to electron hopping between cations, for example $Fe^{2+} \leftrightarrow Fe^{3+}$ and $Mn^{2+} \leftrightarrow Mn^{3+}$. With modern preparation technique, the eddy current loss can be minimized, by careful control of the chemical composition of ferrites. For instance, improvements were made by increasing the grain boundary resistivity through appropriate doping. Dopants reported in literature, that have this effect, include the glass forming dopant SiO_2, and segregating Nb_2O_5, ZrO_2 and Ta_2O_5 [89-92]. For ferrites with high resistivity, domain wall resonance and ferrimagnetic resonance became dominant at high frequencies. Domain wall resonance is closely related to the grain size and defect concentration. A small grain size favors fewer domain walls and thus less associated resonance, as a result of the balance between the magnetostatic energy and domain wall energy. The magnetostatic energy decreases with the volume of the grains ($\propto \varnothing_g^3$), whereas domain wall energy increases proportionally to the wall area, which can be assumed $\propto \varnothing_g^2$. Therefore below a critical grain size, single-domain grains form favorably without domain walls or related domain wall resonance. The ferrimagnetic resonance is partly controlled by chemical composition and resultant magnetocrystalline anisotropy. This resonance, in principle the same as the gyromagnetic resonance, occurs in unsaturated ferrites, which experience primarily an anisotropic magnetic field provided by the crystal structure. The domain wall resonance is usually observed at lower MHz, while ferrimagnetic resonance occurs at the high MHz or even GHz range depending on the actual structure and chemistry of the ferrites.

In the MW frequency range, spin waves may be excited and coupled with the incoming MW waves. The two major relaxation processes are [5,6,84,93,94],

- spin-spin relaxation, during which the uniform precession of magnetic moments couple into degenerate spin wave modes having the same frequency,

- spin-lattice relaxation, during which energy is transferred from the uniform mode into lattice vibrations through various channels, such as impurities which couple to both the magnetic spin system and the crystal lattice.

A good measure for the relaxation energy is the experimentally observed resonance linewidth ΔH, which is related to the damping rate. Relaxation with a faster damping rate leads to a broader ΔH. Spin-spin relaxation may be promoted by imperfections or inhomogeneities in ferrites, such as impurities, porosity, surface pits and anisotropy of random-oriented grains. For example, single-crystal YIG has the narrowest linewidth ΔH = 8.0 A/m (0.1 Oe) at 10 GHz; whereas polycrystalline YIG has a broader ΔH on the order of 800…8000 A/m (10…100 Oe) [95]. The ΔH broadening is associated with the effective magnetic field in each crystallite, which is the sum of macroscopic, demagnetizing and anisotropic field. Because of the random orientation of the crystallites, there is a distribution of effective magnetic field, and in turn, a distribution of resonance frequencies. Inhomogeneities, such as inclusions, pores and surface roughness, can also disturb the local effective fields and lead to ΔH broadening. In addition, the MW field with a high power may introduce instability of the spin motion, resulting in an early decrease of permeability before resonance. The power threshold can be increased by reducing the average grain size.

5.2.4 Ferrites in MW applications

Spinels can be adapted for 3-30 GHz applications by selecting the proper chemical composition [96-99]. For instance, Li spinel is frequently used in microwave devices owing to its square hysteresis loop and a high T_C [6]; Ni spinels are preferred for high power applications because of their stable magnetic properties for frequency and temperature variations. However, spinel ferrites exhibit the well known Snoek's limitation [83], i.e. spinel ferrite of a high permeability has a low natural ferrimagnetic resonance frequency, due to the small cubic magnetocrystalline anisotropy. Contrary to spinels, garnets are rather weakly ferrimagnetic, due to their large formula unit. Garnets contain only trivalent ions; therefore no electron hopping on cation sites can occur, leading to an extremely high resistivity and a low magnetic loss even at high frequencies. Its saturation magneti-

zation, temperature sensitivity and magnetocrystalline anisotropy can also be tuned by changing the compositions [5,86]. Hexagonal ferrites have been developed, for example as permanent magnets, for 1…100 GHz range because of their intrinsic uniaxial anisotropy. This makes their permeability values surpass the Snoek's limitation [98], however also attributes to a high magnetic loss.

In MW signal processing, such as the F layer in MPA structures, the required ferrite must have a low loss at GHz frequencies. Neither spinels nor hexaferrites have favorable properties for MW FR applications, because of their relatively high eddy current loss and/or magnetic loss. Therefore, the only choice will be garnet, which has the lowest current loss and narrowest resonance linewidth (indicating low magnetic losses) among ferrites. Detailed studies on garnet properties and application conditions should be carried out considering

- chemical substitutions to lower losses and tune FR angles,
- microstructural homogeneity, which is essential for eliminating imperfections as energy scattering centers,
- porosity, which should be minimized to avoid "diluting" FR effect or increasing magnetic loss,
- external static field, which should be sufficient to saturate the garnet below resonance,
- actual magnetic losses, which also depend on demagnetizing fields from microstructures and geometric dimensions, and the amplitude of the external static field,
- power of MW waves, which should be smaller than the instability power threshold.

5.3 Synthesis of polycrystalline ferrites

Low-cost and reliable polycrystalline ferrites are used in industrial applications, although they may have less favorable magnetic properties than single crystal ferrites. For MW applications, polycrystalline ferrites are required to have high density, fine grains, and homogeneous microstructures to avoid possible losses.

Most of the bulk ferrites are prepared by a standard ceramic co-firing route [6,87]. In that route, raw material oxides/chlorides/carbonates are first stoichiometrically mixed using

dry, or more commonly, wet milling, followed by solvent removal by heating. During calcination or pre-sintering, the raw materials are then reacted to form the ferrite phase. Typically the reaction temperature for spinels is 900…1200ºC, while it may be as high as 1500ºC for hexagonal ferrites and garnets [87], because of their complex structures. After calcination, the heavily agglomerated lumps formed must be milled again to homogenize/adjust their compositions and to obtain a more uniform and small particle size. At the end of the milling cycle, organic binders are added to facilitate the particle packing during shape forming. The ferrites are finally fired to dense materials, possibly at controlled and programmed oxygen partial pressure, to obtain cations in the right valence. Tape casting, roll compaction, cold isostatic pressing (CIP) and hot pressing (HP) are also applied during compaction for shaping ferrite powders and achieving a high density. The major advantage of co-firing processing is its low-cost and fabrication convenience, which however is offset by inhomogeneous microstructures and imperfections leading to high losses in the prepared polycrystalline ferrite.

Over the recent years, nanotechnology has also been extended to ferrites. Various chemical synthesis techniques for ferrite nanoparticles have been proposed and developed. Usually, the techniques start from the precursor preparation, in which the ions are well mixed on a molecular scale. Solid precursor compositions are then formed by co-precipitation [101,102], hydrothermal treatment [103,104], sol-gel methods [105] and spray roasting. The solid precursors may be amorphous or crystalline single phases with a homogeneous or inhomogeneous composition or physical mixtures of such phases. The precursors are heated to cause decomposition and chemical reaction to produce the desired ferrite phase. The new methods allow the calcining temperature to be lowered by 400-600ºC compared to the conventional co-firing. As a result, the primary particle size can be controlled in the nanometer scale range, and possibly with a large variation of ellipsoidal dimensions, such as in needles or ellipsoids. However, these methods have been limited to relatively simple ferrites, such as pure YIG or two-component spinels, as multiple substitutions make it difficult to achieve a common condition for all the cations to hydrolysize/precipitate/gel. Therefore, another group of synthetic techniques has been introduced to form a single, amorphous solid intermediate that is homogeneous on atomic

scale, directly from the liquid precursor solutions. For example, in the Pechini processes, an intermediate amorphous solid complex forms, which is subsequently decomposed and thermally reacted to yield multi-component oxide phases. Recently, several variants of self-sustaining combustion synthesis are also developed [106,107]. These combustion processes are rapid and may realize direct conversion from the molecular mixture of the precursor solution to the final oxide product, avoiding the formation of crystalline intermediate phases that require inter-crystallite diffusion for completion of the reaction. The phase forming temperature resulted in the Pechini or self-combustion methods can be hundreds of degree lower than co-firing methods. In addition, they are more favorable to form uniform particle morphology, more specific, spherical particle morphology. However, special precautions must be taken regarding release of gases, mainly of CO_x and NO_x during combustion. Magnetic nancomposites [108-111] have been studied which consist of nanoparticles embedded in a non-magnetic matrix, either inorganic or organic. These materials are believed to be promising because the matrices retard motion of the particles, resulting in individually dispersed particles with limited agglomeration and narrow particle size distribution.

Planar magnetic elements have been required and used for compatibility with strip line and microstrip systems. The typical thickness of these planar components is 0.1-0.2 mm, depending on the operation frequency. The preparation methods of ferrite films include spin and dip coating [112,113], pulsed laser deposition (PLD) [114-116], and jet vapor deposition. The PLD technique is most studied and applied to a variety of ferrites, resulting in good magnetic and dielectric properties. For instance, PLD has been successfully applied to prepare high quality hexaferrite $BaFe_{12}O_{19}$ [115] and spinel Li-Zn films [108]. Ferrite thin films have also been fabricated from coating of ferrite nanoparticles. In addition, despite these successful preparations, problems with the microstructures of the ferrite films have been reported. Ferrites are brittle materials; so internal and external stresses should be avoided to prevent cracking and peeling of the film. The compositions need to be adjusted to reduce magnetostriction (change of the ferrite crystal dimensions upon magnetization). And, of course, low-loss homogeneous microstructures must be maintained.

CHAPTER 6

CA,V,ZR-SUBSTITUTED YIG

6.1 Introduction

As discussed in Chapter 5.2.4, the magnetic properties of ferrites can be tailored for specific applications by substitutions and microstructure-control. Here we study for example the ferrite component (F layer) in MPA structures mentioned in Chapter 1. As discussed, the requirements are FR of ~10 /mm and extremely low losses. The actual F layer will be in a planar geometry with a thickness about 0.25 mm, which in practice will be determined by the actually realized FR angle θ_F. MW devices, that utilize the FR effect, are usually operated below resonance to avoid significant energy absorption of the MW field by the spin system in ferrites. Therefore equation (5.18) can be used to estimate a desired saturation magnetization in ferrites from the required the FR angle. Actual losses are not easily predicted by mathematical equations, but generally decrease with reduced anisotropy and porosity, and increased microstructural homogeneity.

YIG was selected as the starting composition and structure, for its low loss and capability to host a wide range of substitutions. It has been reported that at octahedral (d) site substitution, for example In^{3+}, Sc^{3+} and Zr^{4+} [23,24], leads to an increased saturated magnetization, and a reduced magnetocrystalline anisotropy. Significant reduction of the half resonance linewidth (ΔH) was observed in those substituted garnets. However, octahedral substitutions decrease the Curie temperature (T_C) substantially and hence the temperature stability of the garnet. Substitution on tetrahedral Fe^{3+} (a) sites generally results in a lower saturated magnetization, and decreased magnetocrystalline anisotropy [25].

V^{5+} is a common substitution in (a) sites, which can also provide enhancement in T_C to compensate the unfavorable reduction by octahedral substitution [30]. This was explained by V^{5+} replacing the Fe^{3+}-O^{2-}-Fe^{3+} super-exchange through its partially filled 3*d* states. Dodecahedral sites are substituted, often by Ca^{2+}, for charge compensation of cation substitutions with deviating valency on the two other sites. Bi^{3+} dodecahedral substitution was reported to increase the light transmission and thus increase the effective FR of YIG in the optical regime [21,29]. In addition, both Bi^{3+} and V^{5+} have been reported to lower the sintering temperature of YIG by 200-300ºC [105].

For MPA applications at MW frequencies, a composition of Ca,V,Zr -substituted YIG (CVZG) was selected. The functions of the multiple substitutions are: Ca^{2+} for charge compensation; Zr^{4+} for reducing magnetocrystalline anisotropy and increasing the saturation magnetization ($4\pi M_s$); and V^{5+} for maintaining a high T_C. Zr^{4+} is used instead of the more common In^{3+} because the ionic radius of Zr^{4+} (0.72 Å) is closer to that of Fe^{3+} (0.65 Å) than In^{3+} (0.80 Å) on octahedral sites. The fabrication methods for this complex composition have been limited to conventionally co-firing and the Pechini method, as discussed in the previous chapter. The Pechini gel method was used, because it favors (a) a homogeneous chemical composition, and (b) spherical particles in the eventual powders. Preliminary experimental results were presented, followed by discussion on magnetic properties related to microstructures.

6.2 Experiment procedure

The starting chemicals were $Ca(NO_3)_2 \cdot 4H_2O$ (ACS, Fisher), $Fe(NO_3)_3 \cdot 9H_2O$ (ACS, ACROS), $Y(NO_3)_3 \cdot 6H_2O$ (99.9%, Sigma-Aldrich), V_2O_5 (99.9%, Alfa-Aesar), $ZrOCl_2 \cdot 8H_2O$ (>99.5%, Ridel-deHaën) and citric acid (CA, >99.5%, Sigma-Aldrich), ethylene glycol (EG, >99%, from Alfa-Aesar), and 1 N HNO_3 (Ricca Chemical). Deionized water was obtained from a Milli-Q® ultrapure water purification system (Millipore Corp.). Concentrated aqueous solutions of $Ca(NO_3)_2$, $Fe(NO_3)_3$, $Y(NO_3)_3$ were prepared, as well as aqueous solutions of $ZrOCl_2$, and V_2O_5 in diluted HNO_3. These solutions were used to avoid possible concentration variation due to poorly defined crystal water

stoichiometry in the hydrated salts. The composition of CVZG was determined from literature data and prepared as $Y_{2.65}Ca_{0.35}Fe_{4.70}V_{0.05}Zr_{0.25}O_{12}$.

Solutions of Y^{3+}, Ca^{2+}, Fe^{3+}, V^{5+} and Zr^{4+} were mixed in their stoichiometric ratio. CA and EG were added afterwards into the mixture in molar ratios of n(CA):n(total cations) = 1.5 and n(CA):n(EG) = 0.7. The mixture solution was stirred in a 50ºC oil bath for 1 hour using a Rotavapor setup (model R-205v, Brinkmann Instruments Inc.). The oil bath temperature was then raised to 60ºC, and the pressure was gradually decreased from 1 bar to 20 mbar to remove water. Evacuation was stopped when the gel had dried but not yet foamed. The dried gel was taken out of the beaker and ground into powders using an agate mortar. Thermal processing started with organic removal at 450ºC for 30 min with a 1ºC/min heating rate, followed by calcining at 600ºC, 800ºC, 1000ºC or 1200ºC for 1 hour, with 5ºC/min heating and cooling rate. The calcined CVZG powders were denoted as 600CVZG…1200CVZG respectively. The powders were ground again using an agate mortar for subsequent characterization.

XRD patterns were obtained using a Scintag XDS 2000, operating with Cu-K_α radiation (λ = 1.5406 Å). The lattice parameter and amount of impurity perovskite $YFeO_3$ (YIP) phase were estimated by examining XRD patterns with Topas Academic software. The primary particle size ($\varnothing_p$) was obtained using a Micromiretics ASPA 2020 Analyzer (Micromeritics Instrument Corp.). Transmission electron microscopy (TEM) was performed on 600, 800 and 1000CVZG calcined powders using a Philips CM12 (Philips, the Netherland). Magnetization curves were measured using a LakeShore Vibrating Sample Magnetometer (VSM) (Lake Shore Cryotronics, Inc.) with a sensitivity of 1×10^{-9} A·m^2 (1×10^{-6} emu). Complex magnetic permeability measurements were carried out using an Agilent E4991A 1 MHz-3 GHz RF Impedance/Material Analyzer. For this measurement, the calcined powders were pressed at 250 MPa into a washer shape, which had an inner diameter of 3.1 mm and outer diameter of 8.0 mm. The measurement was repeated on the same CVZG washers after sintering in air at 1250ºC for 3 hours. Because of a linear shrinkage of 4…7% in 1200CVZG…600CVZG after sintering, the center of the washer-shaped samples was ground to maintain an inner diameter of 3.1 mm.

6.3 Results and discussions

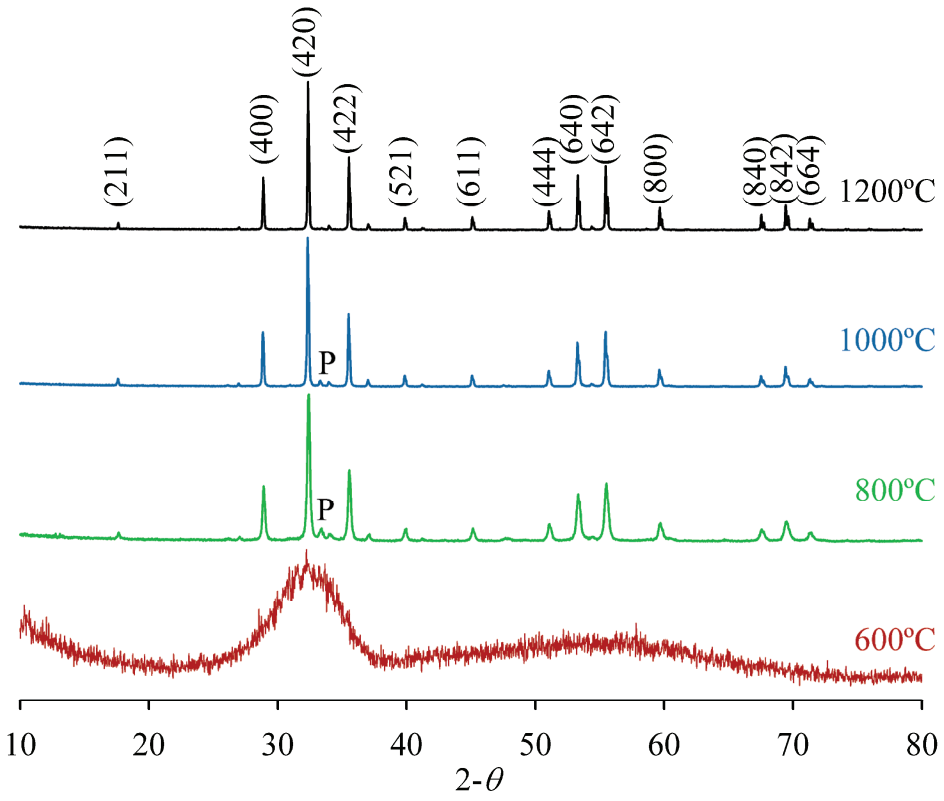

Figure 6.1: XRD patterns of 600…1200CVZG powders. The diffraction peaks from the YIP phase are denoted as P. The slight peak splitting observed in 1000 and 1200CVZG is due to Cu-$K_{\alpha 2}$.

The XRD patterns of as-calcined powders are shown in figure 6.1. 600CVZG showed an amorphous pattern, which was confirmed by its instability in TEM analysis. At 800ºC, the powders already showed mostly YIG garnet phase, with a 6 wt% of impurity YIP phase. However, this small amount of YIP was not considered to influence the magnetic properties of 800CVZG. As the temperature increased, the amount of impurity YIP phase decreased to 3 wt% at 1000ºC and completely disappeared at 1200ºC. The lattice parameter was estimated to be 12.41 Å and the theoretical density was 5.16 g/cm^3. It was noticed that the precursor gel should be ground before calcining to minimize formation of

the YIP phase. In one experiment it was confirmed that a smaller amount of YIP was observed in 800CVZG prepared from pre-ground powders than unground powders, as shown in figure 6.2. This is explained by a severe self-combustion between nitrates and CAEG gel above ~140ºC. The reaction heat is thought to be entrapped in unground gel, resulting in an inhomogeneous temperature distribution and consequent phase formation. The color of the calcined powders varied from dark red, green, dark green to dark gray for 600, 800, 1000 and 1200CVZG respectively.

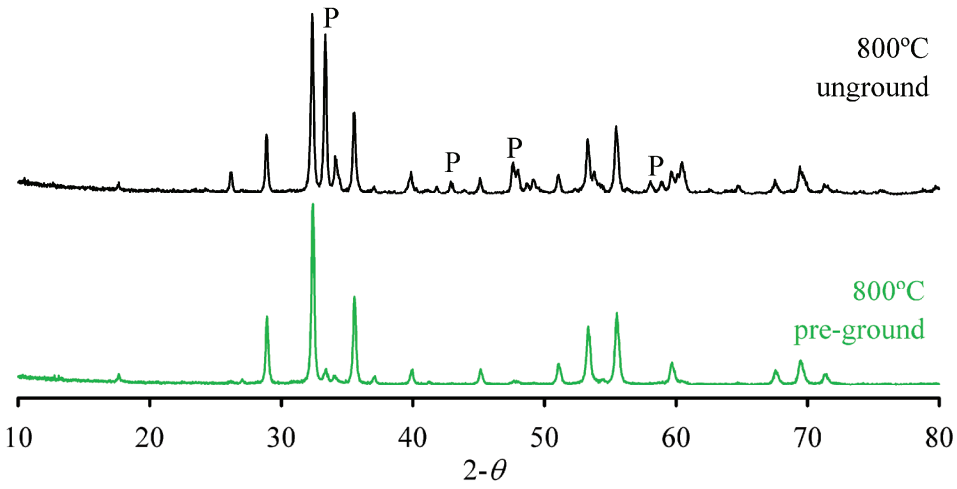

Figure 6.2: XRD patterns of 800CVZG, prepared from unground and pre-ground precursors. The diffraction peaks from the YIP phase are denoted as P.

The particle size ($\varnothing_p$) of calcined CVZG powders grew exponentially with the calcination temperature, as shown in figure 6.3. Figure 6.4 shows TEM images of 800CVZG and 1000CVZG powders, the particle size of which was in agreement with that obtained from the BET measurement.

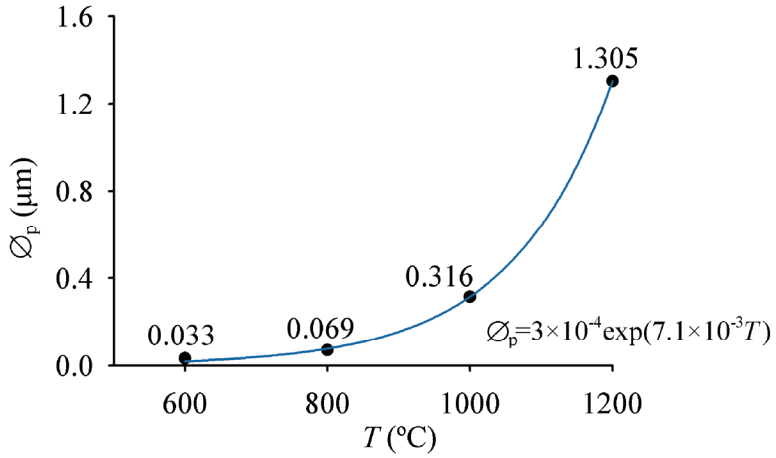

Figure 6.3: The relation of primary particle size and calcination temperature.

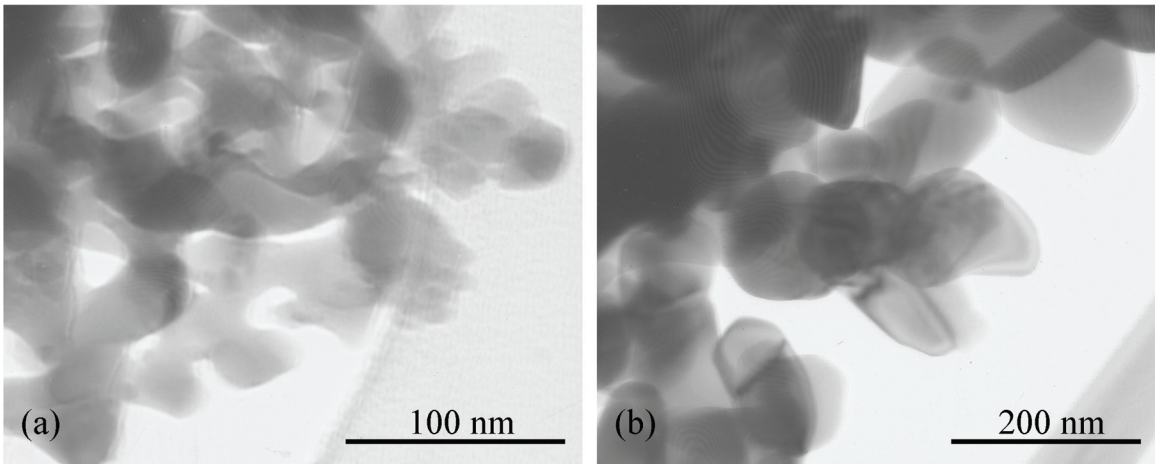

Figure 6.4: TEM images of (a) 800CVZG and (b) 1000CVZG.

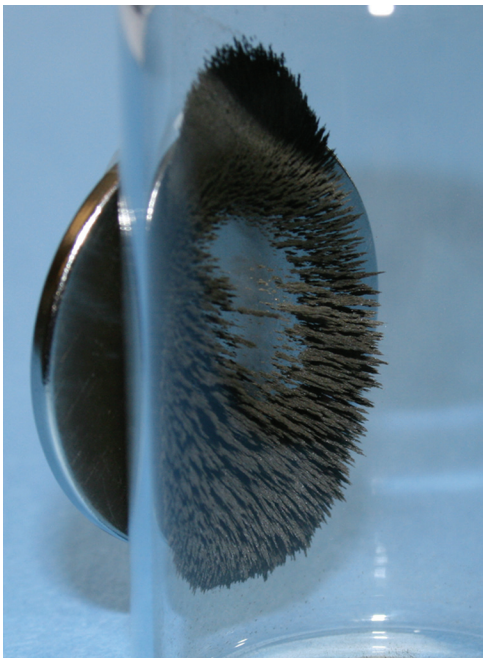

Figure 6.5: An example of soft ferrimagnetic 1200CVZG attracted to a magnet.

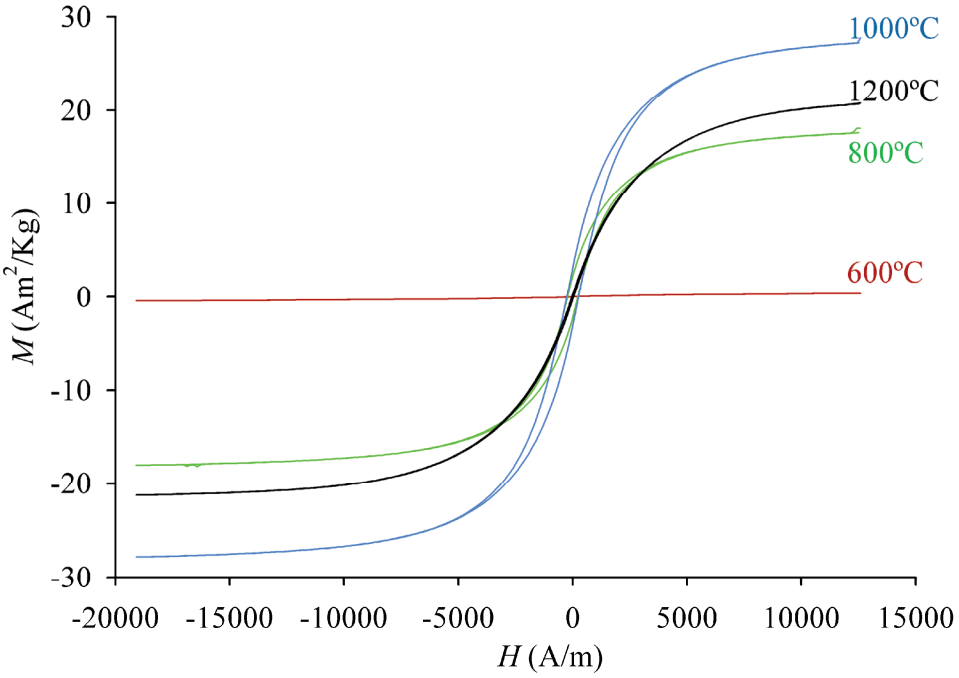

Figure 6.6: Magnetization curves of calcined CVZG powders.

800…1200CVZG were easily magnetized under a magnetic field provided by a small permanent magnet. An example for 1200CVZG is given in figure 6.5. On the contrary, 600CVZG did not respond to the magnet. The magnetization curves (M~H) in figure 6.6 confirmed different magnetization behaviors for the calcined samples. 600CVZG was paramagnetic, mainly due to the amorphous phase and nanometer particle size. 800…1200CVZG were soft-ferrimagnetic, as indicated from their narrow hysteresis loops. 1000CVZG had the highest saturation magnetization (M_s) and coercivity (H_c), while 1200CVZG was almost hysteresis free. $\varnothing_p$, H_c and M_s are summarized in table 6.1, and the variation of H_c~$\varnothing_p$ is shown in figure 6.7. It was observed that H_c decreased after a critical particle size, a phenomenon known as super-magnetization. This is explained by the magnetocrystalline anisotropy energy becoming comparable to the thermal energy for small particles. Therefore, the thermal energy, even at room temperature, overcome the anisotropy and spontaneously reverses magnetization in particles with $\varnothing_p$ < 100 nm. The FR angle, calculated from the measured M_s using equation (5.18), had a maximum value of 11.7º/mm in 1000CVZG.

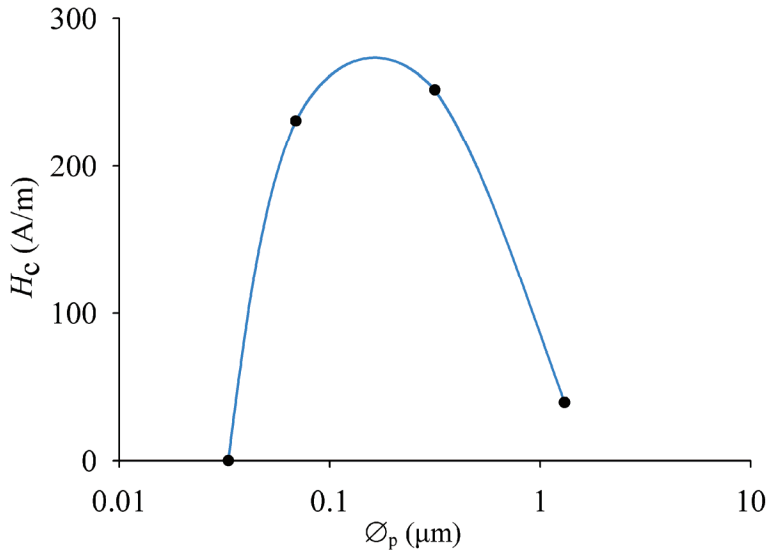

Figure 6.7: Variation of coercivity H_c vs. primary particle size of CVZG.

T (ºC)	$\varnothing_p$ (μm)	H_c (A/m)	M_s (A·m^2/Kg)	θ_F (º/mm)*
600	0.033	-	-	-
800	0.069	230.8 (2.9 Oe)	18.0 (18.0 emu/g)	7.6
1000	0.316	250.7 (3.2 Oe)	27.9 (27.9 emu/g)	11.7
1200	1.305	35.8 (0.5 Oe)	21.4 (21.4 emu/g)	9.0

Table 6.1: Magnetic properties of calcined CVZG powders. *FR angles were calculated from equation (5.18), assuming ε_r~15, no loss in CVZG, and the applied static field has a proper magnitude to saturate CVZG below resonance.

T (ºC)	Calcined CVZG				Sintered CVZG			
	ρ (g/cm^3)	ϕ_p (%)*	$\mu_r'^{\dagger}$	μ_r''	ρ (g/cm^3)	ϕ_p (%)*	$\mu_r'^{\dagger}$	μ_r''
600	2.21	57.2	0.95	0.04	2.34	54.7	1.53	0.1
800	2.38	53.9	3.74	0.23	2.80	45.7	13.63	0.25
1000	2.72	47.3	5.12	0.64	2.90	43.8	14.27	0.44
1200	3.46	32.9	17.32	0.8	4.35	15.7	64.02	0.91

Table 6.2: High frequency magnetic properties of calcined and sintered CVZG. *The porosity was calculated from the XRD density of 5.16 g/cm^3. $^{\dagger}\mu_r'$ and μ_r'' were obtained at lower MHz and 3 GHz respectively.

The complex permeability (μ_r' and μ_r'') of calcined CVZG was shown in figure 6.8. As the calcination temperature increased, both μ_r' and μ_r'' increased, while the resonance frequency decreased due to increased particle size. Figure 6.9 shows that sintering at 1250ºC resulted in lower resonance frequencies, increased μ_r' but not influence on μ_r'' at GHz frequencies. The μ_r' increased dramatically because of domain formation and higher relative density after sintering. However, the compaction method of uniaxial pressing

was inefficient as the primary particle size increased into submicron scales. As a result, both calcined and sintered samples had a significant amount of porosity, as listed in table 6.2. Since it is difficult to extract the actual bulk permeability of the magnetic component from its porous structure, the measured μ_r' and μ_r'' are presented without normalization. For a significant FR effect, the magnetic materials are required to have a high M_s and μ_r' in a static field, and low μ_r'' (hence low $\tan\delta = \frac{\mu''}{\mu'}$) at GHz frequencies. It should be pointed out that the high frequency measurement as presented was performed without a static magnetic field. Upon application of the static field, the magnetic losses are expected to decrease dramatically due to the alignment of the magnetic moment. The current results suggest 1250ºC sintered 1000CVZG would be a good candidate for F layer in MPAs, for its high M_s and low losses at GHz. Colloidal processing of 1000CVZG will be carried out to increase the density of the green and sintered compacts, as well as obtaining a homogeneous microstructure.

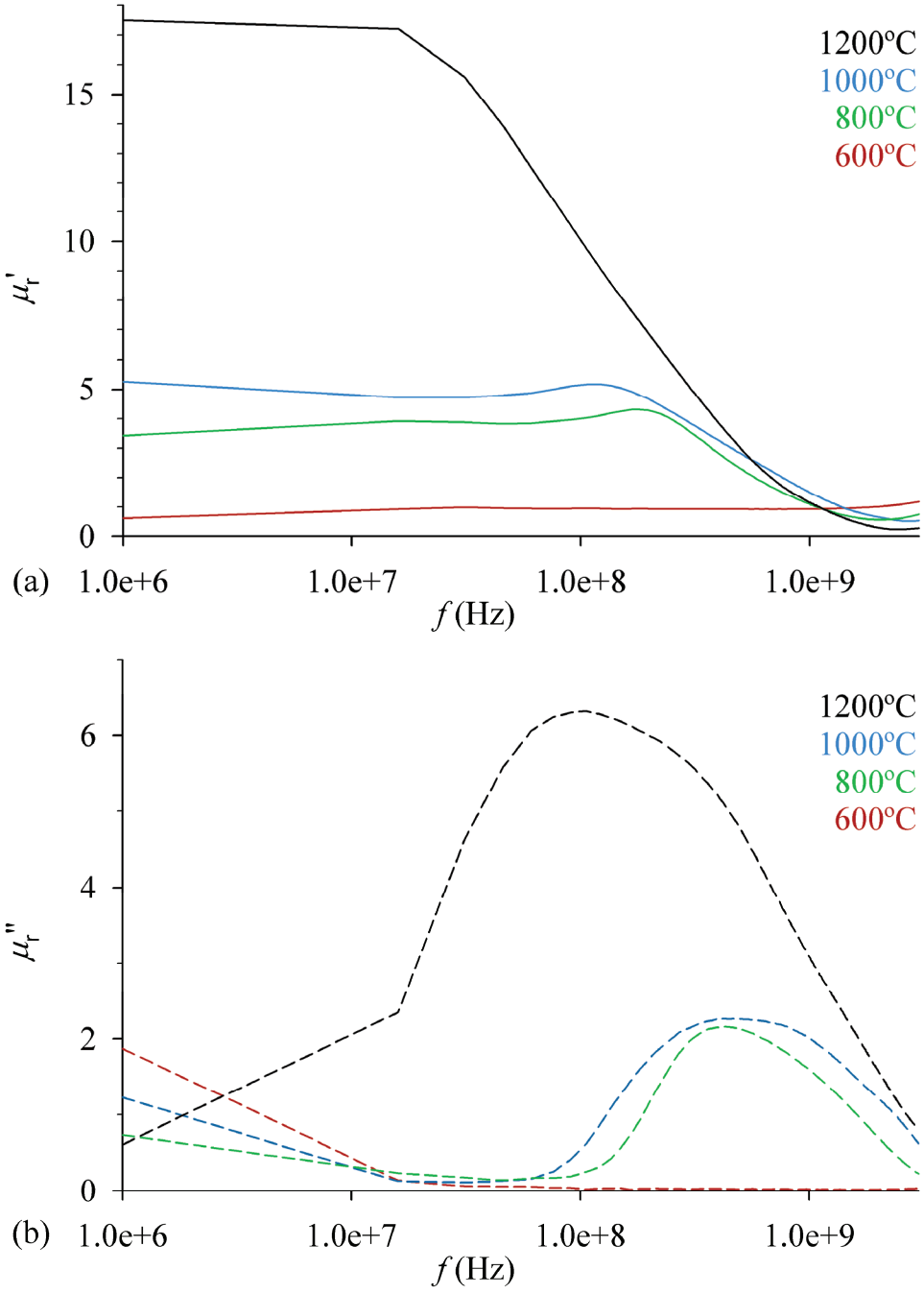

Figure 6.8: Complex permeability of calcined 600…1200CVZG.

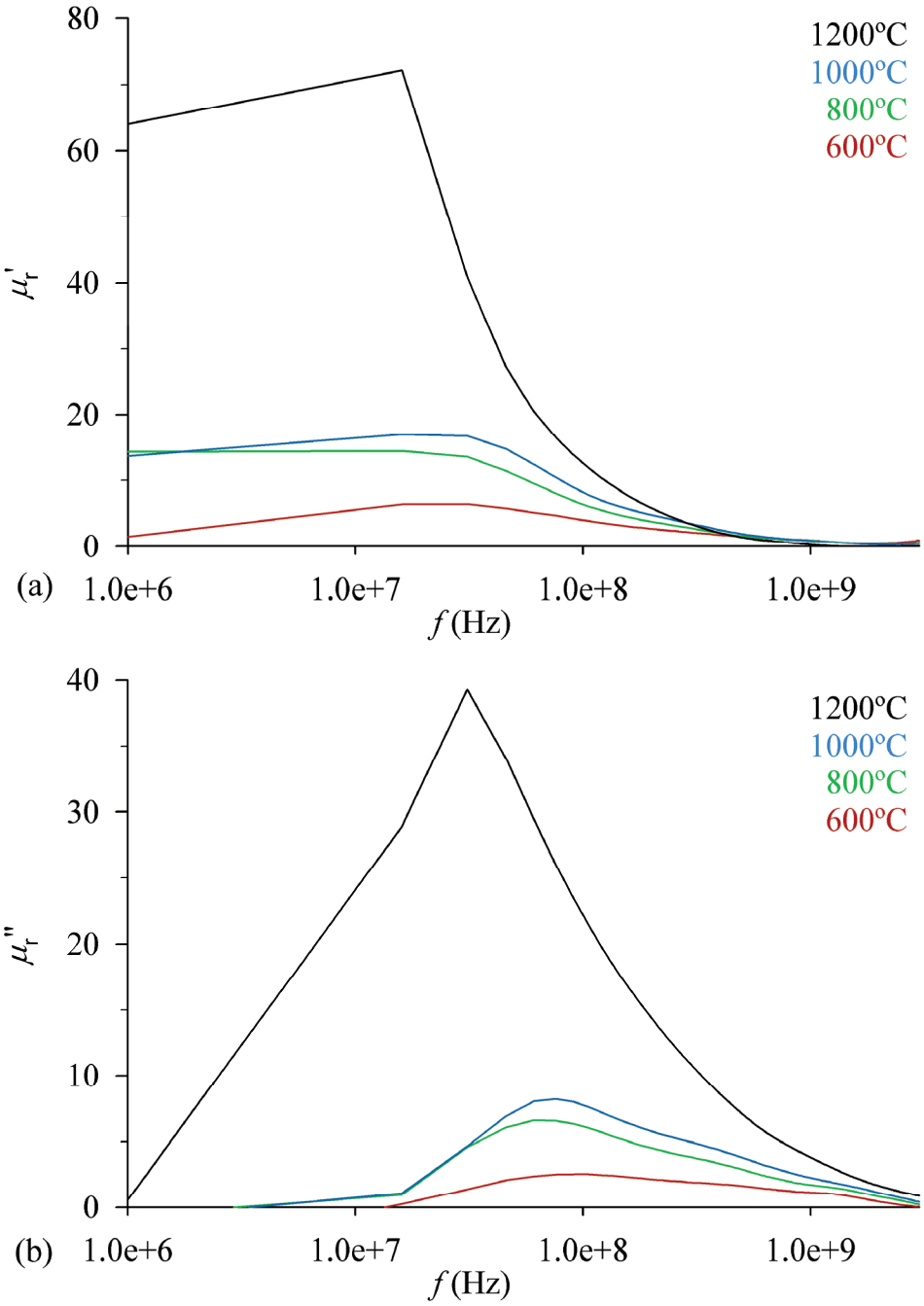

Figure 6.9: Complex permeability of 600…1200CVZG after sintering at 1250ºC.

CHAPTER 7

FUTURE WORK FOR COMPLEX MPA DESIGNS

Demonstration of effective low-loss AD and F materials as discussed in Chapter 3, Chapter 4 and Chapter 6, has opened new avenues for high-performance antenna structures. Starting from the obtained promising results, advanced and delicate ceramic processing and ceramic parts are and will have to be developed to meet the requirements for more advanced and complex MPA designs.

7.1 Optimization of AD materials

The current hurdles towards commercialization of AD materials are the high-temperature lamination, and the expensive diamond-machining step. They also limit the fabrication capability to realize complicated AD materials in advanced antenna designs. Therefore the use of advanced ceramic processing techniques is proposed to overcome these problems, as well as improve fabrication efficiency. The two techniques that are most suitable, and currently under intense study are Robocasting® [118-121] and ink-jet printing [122]. In these methods, ceramic dispersion gels are directly written into a target pattern. The Robocasting technique can write 3D connected structures; the ink-jet printing technique produces complex 2D patterns and also allows for 3D structures. Our previous studies on α-Al_2O_3 and TiO_2 have already shown that it is possible to reach the target dielectric properties. In addition they provide colloidal processing methods to prepare high quality dispersions to be applied in the Robocasting and ink-jet printing techniques as mentioned.

7.1.1 Robocasting

Robocasting is a novel and powerful tool for producing complex 3D structures, with high aspect ratio walls or spanning elements. A stable colloidal suspension is first prepared with a high solid load (~60 vol%) in the presence of polymer binders. Gelation is achieved by changing the p_H to the isoelectric point of the hydrophilic polymer binders. Consequently, the dispersed particles become linked in the polymer network, forming a thixotropic gel. When extrude through a dispensing needle, the gel experiences a high shear stress and thus flow. After the gel leaves the needle, the absence of shear stress results in an immediate formation of a solid gel. Multiple layers and components can be deposited in one run, because the low solvent content and high solid load in the gel avoid adjacently casted elements to merge with each other. The pre-designed casting routes and directions are performed by a 3D positioning device as shown in figure 7.1. After casting, the green part is dried, debindered and finally sintered to an almost full density.

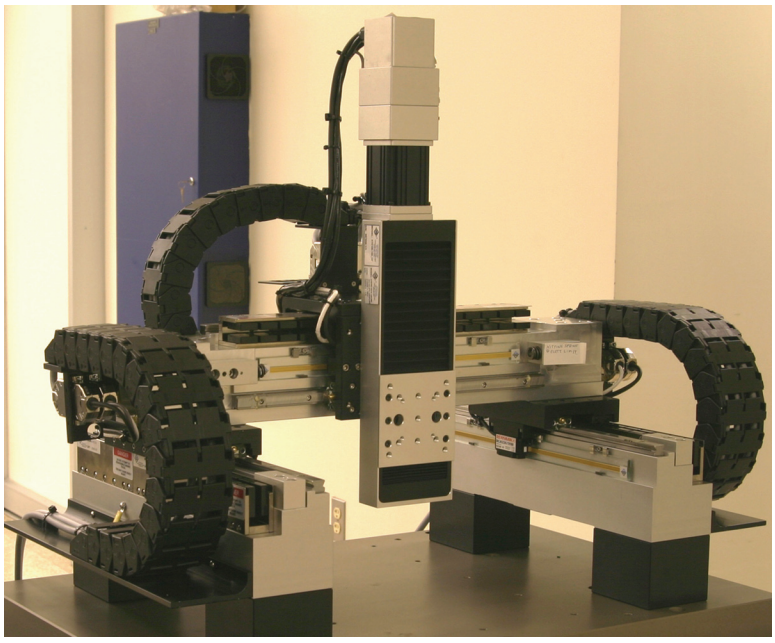

Figure 7.1: Mechanical bearing system of a customized Robocastor (Aerotech Inc.).

Robocasting can be used in fabricating AD layers by adopting woodpile structures. Single or multiple AD layers can be made by alternatively writing parallel rods of different dielectrics. A simple design of Robocasted AD layer is shown in figure 7.2 (a), in which the ε_{rh} dielectric is TiO_2 rods and ε_{rl} dielectric is air. The larger difference in permittivity between TiO_2 and air than barium titanate and α-Al_2O_3 can provide a higher dielectric anisotropy which is favorable for miniaturization of the target antenna designs. Contrary to its machined counterpart in figure 7.2(b), robocasting of (a) will take only minutes, whereas days are spent on (b) during laminating and diamond-machining. The directions of the principle dielectric axes in AD layers are customizable by adjusting casting routes and directions. For green parts consisting of multiple components, the mismatch between thermal expansion coefficients must be minimized to avoid cracking and fracturing during thermal treatment.

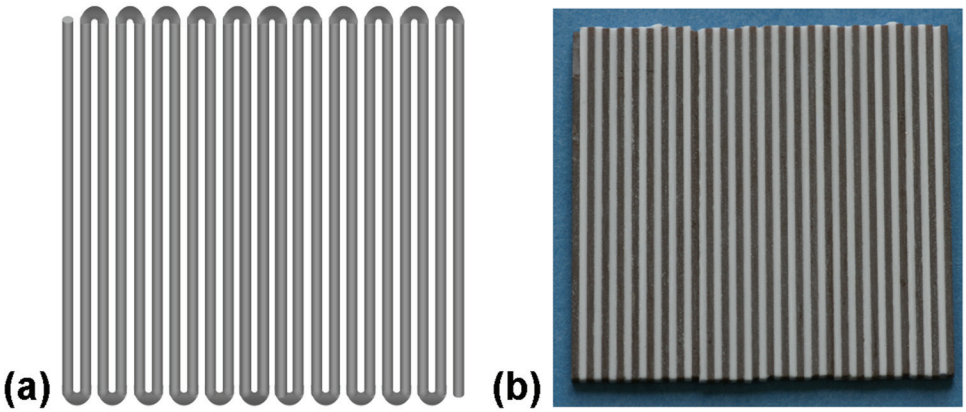

Figure 7.2: (a) Designed AD layer of casted TiO_2 rods. (b) AD layer of α-Al_2O_3 and barium titanate made from adhesive-lamination and diamond-machining.

7.1.2 Ink-jet printing

Ink-jet printing will be used to print AD layers with complex, detailed patterns, for example, a mosaic pattern with each block assigned to a different ceramics. Unlike Robocasting, suspensions used in ink-jet printing are of a low solid load (1- 5vol%) and water-like viscosity. The suspension must be fully deagglomerated and colloidally stabilized to

avoid blockage inside the delicate piezoelectric printing heads. An ink-jet printer is shown in figure 7.3, which is equipped with multiple printing heads. A 5 vol% TiO_2 suspension was successfully printed in parallel rows, as shown in figure 7.4. No clogging or sedimentation was observed during printing, which was attributed to the optimization of the TiO_2 suspension. Other ceramic suspensions, such as α-Al_2O_3 and CVZG, are now studied for their printing capabilities. The positioning accuracy has been tested and approved, which is critical for replicating complicated MPA patterns into actual structures. Due to a high solvent content in the printing suspension, green patterns should be carefully dried before sintering or printing another layer atop of the previous one. The creation of 3D structures might be possible, but would require repeated (automated) drying and debindering treatments between the printings of adjacent layers.

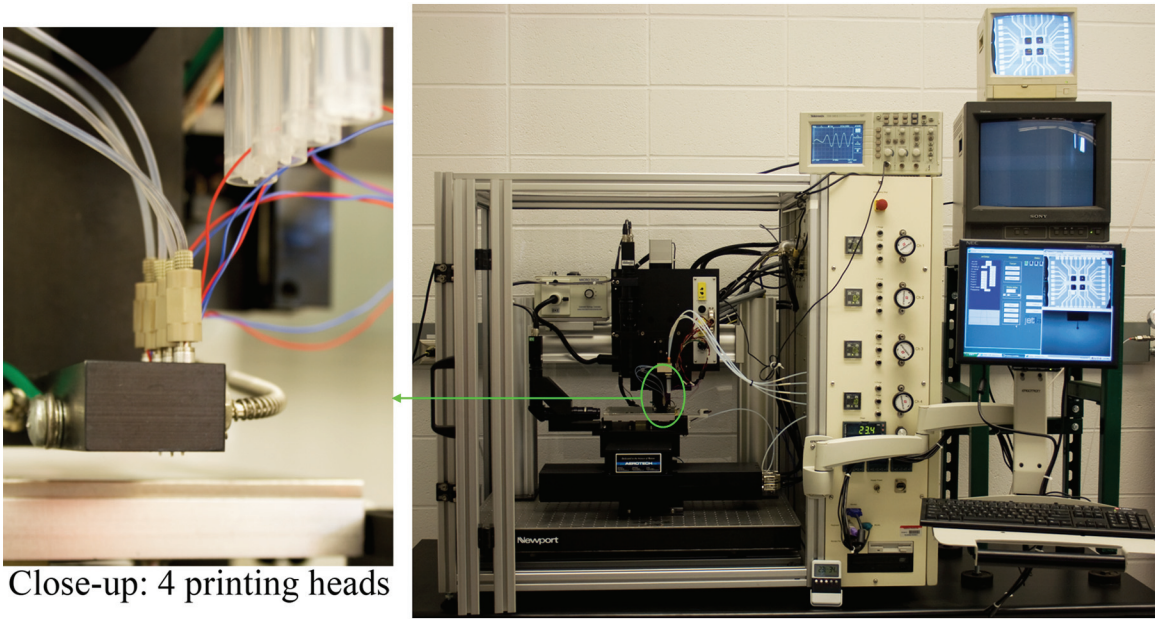

Figure 7.3: Ink-jet printer (MicroFab Technologies, Inc.).

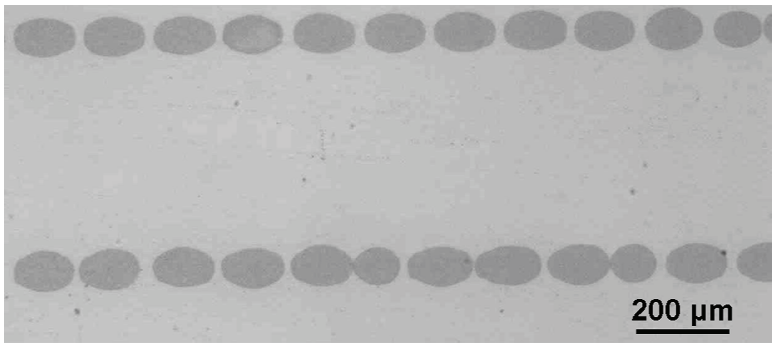

Figure 7.4: Optical image of ink-jet printed parallel rows of TiO_2.

7.2 Optimization of F materials

The major challenge in the fabrication of CVZG F materials is their consolidation into usable dense sheets, without adversely affecting the favorable magnetic properties obtained in powders and sintered compacts. Both dielectric and magnetic properties are determined by both chemical compositions and microstructures. Dielectric losses in CVZG can result from energy dissipation by electron hopping across multi-valence cations, scattering due to inhomogeneity, and polar species absorbed on porous structure. Magnetic properties and complex permeability of CVZG powders were found to be directly related to the particle size, domain size and porosity. These effects are so outspoken and yet complicated, that no semi-quantitative prediction is possible. Chemical and microstructure homogeneity also critically influence ceramic properties, especially substituted ceramics. However, this aspect has so far, not been a topic of detailed studies on magnetic ceramics, especially for substituted garnets. Therefore optimization of F materials focuses on densification of CVZG with homogeneous chemistry and microstructures with consideration of the following aspects:

- pre-treatment and dispersion of CVZG powders to produce a deagglomerated and stabilized suspension,
- careful control of the partial oxygen pressure during sintering to avoid reduction of multi-valence cations.

Recent research demonstrated the possibility to disperse nanoparticles of Fe_3O_4 [123,124], but little is known about the colloidal properties of submicron garnet powders. Therefore exploration is currently being carried out for CVZG powders. As shown in figure 6.4, the as-prepared CVZG powders slightly agglomerated, which is attributed to magnetic, chemical and van der Waal attractions. 1000CVZG is studied as a starting material because its average particle size of ~0.3 μm is considered suitable for colloidal stabilization. Various surfactants, such as citric acid and Darvan-C, and solvents, such as water and iso-propanol, can be tested to determine practical stabilizing conditions. A successful colloidal processing will also provide a pathway for fabricating CVZG layers or patterns by Robocasting and ink-jet printing.

Starting from the optimized magnetic properties, proper instrumentation can be set up for measuring the Faraday rotation effect, and its relationship with the measured magnetic properties. Since Faraday rotation is related to the layer thickness, a proper value can be estimated for each frequency range (wavelength).

CONCLUSIONS

In this study, we designed and fabricated dielectrics and ferrites for MW antenna applications, based on a specific MPA design for use in the X-band. The MPAs are composed of anisotropic dielectric (AD) and ferrimagnetic (F) layers, which are studied and prepared separately.

The fabrication and characterization were demonstrated of textured mean-field anisotropic dielectrics from ceramic laminates using commercially available α-Al_2O_3 and barium titanate substrates. Loss effects of several possible adhesive agents were documented; M-bond 610 provided the best compromise between dielectric loss and mechanical strength. Artificial anisotropic dielectric layers with thicknesses as small as 1 mm were achieved by careful diamond machining. One application of such anisotropic dielectric layers is demonstrated for the first time in a simplified 6-layer antenna assembly. To lower the dielectric loss in AD layers further, dense α-Al_2O_3 and TiO_2 were prepared by colloidal consolidation and low temperature sintering. Commercially available α-Al_2O_3 and TiO_2 powders were stabilized in p_H = 2.0 HNO_3 and p_H = 10.5 NH_3 solutions respectively. After colloidal consolidation and drying, compacts with a high relative density were obtained. Such compacts densified almost completely at a temperature as low as 1300ºC for α-Al_2O_3 and 1000ºC for TiO_2. The 1300ºC-sintered α-Al_2O_3 had a dielectric loss tangent $< 10^{-4}$ at GHz. The 1000ºC-sintered TiO_2 had a better overall performance than samples sintered at other temperatures: a homogeneous microstructure, a small grain size of 2.2 μm, a high flexural strength of 400 MPa and a low dielectric loss of 1.4×10^{-4} at 6.4 GHz. Both the sintering temperature and room temperature dielectric loss are the lowest among all the reported values for undoped TiO_2 samples. Al was homogeneously doped into polycrystalline rutile TiO_2 using a gel-assisted infiltration method and low-temperature sintering. Aqueous solution of citric acid and ethylene glycol was used

as the infiltration medium, which formed a gel on heating to immobilize Al^{3+} inside the infiltrated TiO_2. The sintered Al-doped TiO_2, obtained from such compacts was found to have homogeneous microstructure, and uniform doping concentration. The success of the doping method as presented relied on cation immobilization by the gel and microstructure homogeneity of infiltrated compacts.

Ca,V,Zr substituted-$Y_3Fe_5O_{12}$ garnet (CVZG) was selected for the F layer because of its low loss and capability to provide Faraday rotation required by MPAs. CVZG was successfully prepared using the citric-gel method, and the garnet phase formed at a temperature as low as 800ºC. The primary particle size was found to increase exponentially with the calcination temperature. The magnetic permeability and loss were observed to be closely related to the primary particle sizes, and grain size. A 1000ºC calcined CVZG with the highest saturated magnetization and relatively low loss, was selected as the candidate material for F layers. In addition, its submicron particle size made it suitable for the subsequent colloidal processing, now under study to produce a homogeneous and dense garnet structure.

In summary, the current progress and fabrication principles for AD and F materials have provided options for new antenna concepts. Individual ceramic components have been optimized for specific MPA antenna requirements. Advanced processing techniques can be applied to accommodate more advanced and complicated antenna designs, and offer opportunities for large scale fabrication.

BIBLIOGRAPHY

1. A.J. Moulson and J.M. Herber, *Electroceramics: Materials, Properties, Applications*, 2nd ed., John Wiley & Sons, 2003. ISBN 0-471-49747-7.

2. I.M. Reaney and D. Iddles, "Microwave dielectric ceramics for resonators and filters in mobile phone networks," *J. Am. Ceram. Soc.*, **89** [7] 2063-72 (2006).

3. R. Freer and F. Azough, "Microstructural engineering of microwave dielectric ceramics," *J. Eur. Ceram. Soc.*, **28** 1433-41 (2008).

4. W.H. von Aulock, *Handbook of microwave ferrite materials*, Academic press, New York and London, 1965. ISBN-10: 0127233504.

5. B. Lax and K.J. Button, *Microwave ferrites and ferrimagnetics*, McGraw-Hill, New York, 1962.

6. J. Smit and H.P.J. Wijn, *Ferrites. Physical properties of ferrimagnetic oxides in relation to their technical applications*, Wiley, New York, 1959.

7. M. Pardavi-Horvath, "Microwave applications of soft ferrites," *J. Magn. Magn. Mater.*, **215-6** 171-83 (2000).

8. C. Williams, "Design considerations for microwave packages," *Am. Ceram. Soc. Bul.*, **70** [4] 714-21 (1991).

9. IEEE Std 521™-2002 (Revision of IEEE Std 521-1984), IEEE standard letter designations for radar-frequency bands.

10. A. Figotin and I. Vitebsky, "Nonreciprocal magnetic photonic crystals," *Phys. Rev. E*, **63**, 066609 (2001).

11. A. Figotin and I. Vitebsky, "Electromagnetic unidirectionality in magnetic photonic crystals," *Phys. Rev. B*, **67** 165210 (2003).

12. G. Mumcu, K. Sertel, J.L. Volakis, A. Figotin and I. Vitebsky, "RF propagation in finite thickness non-reciprocal magnetic photonic crystals," *IEEE Antenna Propagat. Soc. Symp.*, **2** 1395-8 (2004).

13. M.E. Tobar, J. Krupka, E.N. Ivanov and R.A. Woode, "Anisotropic complex permittivity measurements of mono-crystalline rutile between 10 and 300 K", *J. Appl. Phys.*, **83** [3] 1604-9 (1998).

14. D.C. Flanders, "Submicrometer periodicity gratings as artificial anisotropic dielectrics," *Appl. Phys. Lett.*, **42** [6] 492-4 (1983).

15. X. Gong, E.E. Hoppenjans, Z.N. Wing, R.G. Geyer, J.W. Halloran and W.J. Chappell, "Tailored and anisotropic dielectric constants through porosity in ceramic components," *IEEE T. Microw. Theory*, **53** [11] 3638-47 (2005).

16. R.E. Collin, "A simple artificial anisotropic dielectric medium," *IEEE T. Microw. Theory*, **6** [2] 206-9 (1958).

17. N.M. Alford and S.J. Penn, "Sintered alumina with low dielectric loss," *J. Appl. Phys.*, **80** [10] 5895-8 (1996).

18. A. Templeton, X. Wang, S.J. Penn, S.J. Webb, L.F. Cohen and N.M. Alford, "Microwave dielectric loss of titanium oxide," *J. Am. Ceram. Soc.*, **83** [1] 95-100 (2000).

19. Y. Konishi, "Novel dielectric waveguide components – microwave applications of new ceramic materials," *Proc. IEEE*, **79** [6] 726-40 (1991).

20. K. Wakino, T. Nishikawa, Y. Ishikawa, and H. Tamura, "Dielectric resonator materials and their application for mobile communication systems," *Br. Ceram. Trans. J.*, **89** [2] 39-43 (1990).

21. K. Shinagawa, "Faraday and Kerr effects in ferromagnets", *Solid State Sci.*, **128**, [Issue: Magneto-Optics], 137-75 (2000).

22. H.J. Van Hook and F. Euler, "Anisotropy linebroadering in polycrystalline V-In substituted YIG," *J. Appl. Phys.*, **40** [10] 4001-5 (1969).

23. H.J. Van Hook, J.J. Green, F. Euler and E.R. Czerlinsky, "Linewidth reduction through Indium substitution in Calcium-Vanadium garnet," *J. Appl. Phys.*, **39** [2] 730-1 (1968).

24. W. Simonet and A. Hermosin, "Tempertarue dependence of the first magnetocrystalline anisotropy constant of polycrystalline Ca-In-V and Ca-Zr-YIG," *J. Appl. Phys.*, **49** [3] 1956-8 (1978).

25. C.E. Patton, "Effective lindwidth due to porosity and anisotropy in polycrystalline yttrium iron garnet and Ca-V-substituted yttrium iron garnet at 10 GHz," *Phys. Rev.*, **179** [2] 352-8 (1969).

26. H.J. van Hook, "Microwave loss in low-magnetization in polycrystalline garnets: a comparation of Ga and Ca-V-In-substituted YIG," *IEEE T. Magn.*, September 770-3 (1971).

27. J.B. Llabrés, "Curie temperature and superexchange interaction in cacium-vanadium iron garnets," *Phys. Stat. Sol. (a)*, **4** K61 K61-4 (1971).

28. F. Euler, and H.J. Van Hook, "Magnetic anisotropy of vanadium-indium-substituted YIG," *J. Appl. Phys.*, **41** [8] 3325-31 (1970).

29. R.M Lambert, "Faraday rotation in a calcium-bismuth-vanadium iron garnet," *J. Phys. D: Appl. Phys.*, **4** 139-46 (1971).

30. A.S. Hudson, "Substituted calcium-vanadium garnets as potential microwave materials," *J. Phys. D.: Appl. Phys.*, **5** 1031-37 (1971).

31. M. Pechini, U.S. Patent 3,330,697, 1967.

32. C. Kittel, *Introduction to Solid State Physics*, 8th ed., John Wiley & Sons, 2005. ISBN 0-471-41526-X.

33. G.G. Raju, *Dielectrics in electric fields*, Marcel Dekker, 2003.

34. L. Egerton and J. Thomson Jr., "Preparation of high density ceramic TiO_2 having low dielectric loss at microwave frequencies," *Ceram. Bul.*, **50** [11] 924-8 (1971).

35. V.L. Gurevich and A.K. Tagantsev, "Intrinsic dielectric loss in crystals," *Adv. Phys.*, **40** [6] 719-67 (1991).

36. N.M. Alford, J. Breeze, X. Wang, S.J. Penn, S. Dalla, S.J. Webb, N. Ljepojevic, and X. Aupi, "Dielectric loss of oxide single crystals and polycrystalline, analogues from 10 to 320 K," *J. Eur. Ceram. Soc.*, **21** 2605-11 (2001).

37. L.M. Rodriguez-Martinez and J.P. Attfield, "Cation disorder and size effects in magnetoresistive manganese oxide perovskites," *Phys. Rev. B.*, **54** [22] 15622-5 (1996).

38. S. Kwashima, M. Nishida, I. Ueda, and H. Ouchi, "$Ba(Zn_{1/3}Ta_{2/3})O_3$ ceramics with low dielectric loss at microwave frequencies," *J. Am. Ceram. Soc.*, **66** [6] 421-3 (1983).

39. I.M. Reaney, P.L. Wise, I. Qazi, C.A. Miller, T.J. Price, D.S. Cannell, D.M. Iddles, M.J. Rosseinsky, S.M. Moussa, M. Bieringer, and L.D. Noailles, "Ordering and quality factor in $0.95BaZn_{1/3}Ta_{2/3}O_3$-$0.05SrGa_{1/2}Ta_{1/2}O_3$ production resonators," *J. Eur, Ceramc. Soc.*, **23** [16] 3021-34 (2003).

40. S.J. Penn, N.M. Alford, A. Templeton, X. Wang, M. Xu, M. Reece, and K. Schrapel, "Effect of porosity and grain size on the microwave dielectric properties of sintered alumina," *J. Am. Ceram. Soc.*, **80** [7] 1885-8 (1997).

41. E.S. Kim and K.H. Yoon, "Effect of nickel on microwave dielectric properties of $Ba(Mg_{1/3}Ta_{2/3})O_3$," *J. Mater. Sci.*, **29** 830-34 (1994).

42. M.P. McNeal, S.J. Jang, and R.E. Newnham, "The effect of grain and particle size on the microwave properties of barium titanate ($BaTiO_3$)," *J. Appl. Phys*. **83** [6] 3288-97 (1998).

43. L. Zhang, G. Mumcu, S. Yarga, K. Sertel, J.L. Volakis, and H. Verweij, "Fabrication and characterization of anisotropic dielectrics for low-loss microwave applications," *J. Mater. Sci.*, **43** [5] 1505-9 (2008).

44. G. Mumcu, K. Sertel, and J.L. Volakis, "A measurement process to characterize natural and engineered low loss uniaxial dielectric materials at microwave frequencies," *IEEE T. Microw. Theory*, **56** [1] 217-23 (2008).

45. D. Kajfez and P. Guillon, *Dielectric resonators*, Artech House, Dedham, MA, 1986.

46. J. Krupka, K. Derzakowski, B. Riddle, and J. Baker-Jarvis, "A dielectric resonator for measurements of complex permittivity of low loss dielectric materials as a function of temperature," *Meas. Sci. Technol.*, **9** [10] 1751-6 (1998).

47. M.N. Rahaman, *Ceramic processing and sintering*, 2nd ed., Marcel Dekker, 2003. ISBN 0-8247-0988-8.

48. T. Burg, T. Bak, J. Nowotny, L. Sheppard, C.C. Sorrell, and E.R. Vance, "Effect of sintering on microstructure of TiO_2 ceramics," *Adv. Appl. Ceram.*, **106** [1-2] 57-62 (2007).

49. F.A. Grant, "Properties of rutile (titanium dioxide)," *Rev. Mod. Phys.*, **31** 646-74 (1959).

50. R.A. Parker, "Static dielectric constant of rutile (TiO_2), 1.6-1060°K," *Phys. Rev.*, **124** 1719-22 (1961).

51. J.F. Baumard and E. Tani, "Electric conductivity and charge compensation in Nb-doped TiO_2 rutile," *J. Chem. Phys.*, **67** [3] 857-60 (1977).

52. L.G. Rowan, "Microwave dielectric loss of V^{+4}-doped TiO_2 at low temperatures," *Phys. Rev. B.*, **5** [5] 1675-6 (1972).

53. M.F. Yan and W.W. Rhodes, "Low temperature sintering of TiO_2," *Mater. Sci. Eng.*, **61** 59-66 (1983).

54. E.A. Barringer and H.K. Bowen, "Formation, packing, and sintering of monodisperse titanium dioxide powders," *J. Am. Ceram. Soc.*, **65** [12] C199-201 (1982).

55. L. Zhang, H. Verweij, "Preparation of homogeneous Al-doped TiO_2 rutile by gel-assisted infiltration," unpublished.

56. K. Shqau, M.L. Mottern, D. Yu, and H. Verweij, "Preparation and properties of porous α-Al_2O_3 membrane supports," *J. Am. Ceram. Soc.*, **89** [6] 1790–4 (2006).

57. M.I. Menderson, "Average grain size in polycrystalline ceramics," *J. Am. Ceram. Soc.*, **52** [8] 443-6 (1969).

58. R. Apetz and M.P.B. van Bruggen, "Transparent alumina: a light-scattering model," *J. Am. Ceram. Soc.*, **86** [3] 480-6 (2003).

59. L. Zhang, K. Shqau, G. Mumcu, S. Yarga, K. Sertel, J.L. Volakis and H. Verweij, "Viable route for dense TiO_2 with low microwave dielectric loss," unpublished.

60. J.B. Wachtman Jr., W. Capps, and J. Mandel, ''Biaxial flexure tests for ceramic substrates,'' *J. Mater.*, **7** [2] 188–94 (1972).

61. O. Sudre and F.F. Lange, "The effect of inclusions on densification: III, the desintering phenomenon," *J. Am. Ceram. Soc.*, **75** [12] 3241-51 (1992).

62. Y. Kishi and K. Ogura, "High strength, electrically conductive pore-free TiO_2 ceramics made by hot isostatic pressing," *J. Mater. Res.*, **12** [4] 1056-61 (1997).

63. C.T. Dervos, E. Thirios, J. Novacovich, P. Vassiliou, and P. Skafidas, "Permittivity properties of thermally treated TiO_2," *Mater. Lett.*, **58** 1502-07 (2004).

64. X. Wang, *The investigation of polycrystalline Al_2O_3 and TiO_2 as models for high frequency dielectrics*, Thesis, South Bank University, London. September, 1999.

65. W.Y. Wang, D.F. Zhang, T. Xu, X.F. Li, T. Zhou, and X.L. Chen, "Effect of temperature on nonlinear electrical behavior and dielectric properties of (Ca, Ta)-doped TiO_2 ceramics," *Mater. Res. Bul.*, **37** 1197-1206 (2002).

66. M. Okutan, E. Basaran, H.I. Bakan, and F. Yakuphanoglu, "AC conductivity and dielectric properties of Co-doped TiO_2," *Physica B*, **364** 300-5 (2005).

67. D. Morris, Y. Dou, J. Rebane, C. E. J. Mitchell, R. G. Egdell, D. S. L. Law, A. Vittadini, and M. Casarin, "Photoemission and STM study of the electronic structure of Nb-doped TiO_2," *Phys. Rev. B*, **61** [20] 13445-57 (2000).

68. L. R. Sheppard, T. Bak, and J. Nowotny, "Electrical Properties of Niobium-Doped Titanium Dioxide. 1. Defect Disorder," *J. Phys. Chem. B*, **110** 22447-54 (2006).

69. J.B. Yin and X.P. Zhao, "Preparation and Electrorheological Activity of Mesoporous Rare-Earth-Doped TiO_2," *Chem. Mater.*, **14** 4633-40 (2002).

70. T. Bak, J. Nowotny, M. Rekas, and C.C. Sorrell, "Defect chemistry and semiconducting properties of titanium dioxide: I Intrinsic electronic equilibrium," *J. Phys. Chem. Solids*, **64** 1043-56 (2003).

71. T. Bak, J. Nowotny, M. Rekas, and C.C. Sorrell, "Defect chemistry and semiconducting properties of titanium dioxide: II Defect diagrams," *J. Phys. Chem. Solids*, **64** 1057-67 (2003).

72. J. Yahia, "Dependence of the electrical conductivity and thermoelectric power of pure and aluminum-doped rutile on equilibrium oxygen pressure and temperature," *Phys. Rev.*, **130** [5] 1711-9 (1963).

73. M.F. Yan and W.W. Rhodes, "Effects of cation contaminants in conductive TiO_2 ceramics," *J. Appl. Phys.*, **53** [12] 8809-18 (1982).

74. J. Nowotny, M. Radecka, and M. Rekas, "Semiconducting properties of undoped TiO_2," *J. Phys. Chem. Solids*, **58** [6] 927-37 (1997).

75. D. Morris, Y. Dou, J. Rebane, C.E.J. Mitchell, and R.G. Egdell, "Photoemission and STM study of the electronic structure of Nb-doped TiO_2," *Phys. Rev. B*, **61** [20] 13445/1-13 (2006).

76. E. Volceanov, A. Volceanov¸ and Ş. Stoleriu, "Assessment on mechanical properties controlling of alumina ceramics for harsh service conditions." *J. Eur. Ceram. Soc.*, **27** 759-62 (2007).

77. E.P. Barrett, L.G. Joyner, and P.P. Halenda, "The determination of pore volume and area distributions in porous substances. I. Computations from nitrogen isotherms," *J. Am. Chem. Soc.*, **73** 373-80 (1951).

78. E.W. Washburn, "The dynamics of capillary flow," *Phys. Rev.*, **17** 273-83 (1921).

79. R. Munro, "Evaluated material properties for a sintered α-Al_2O_3," *J. Am. Ceram. Soc.*, **80** [8] 1919-28 (1997).

80. V. Sergo, D.M. Lipkin, G. De Portu, and D.R. Clarke, "Edge stresses in alumina/zirconia laminates," *J. Am. Ceram. Soc.*, **80** [7] 1633-8 (1997).

81. S. Ho, C. Hillman, F.F. Lange, and Z. Suo, "Surface cracking in layers under biaxial, residual compressive stress," *J. Am. Ceram. Soc.*, **78** [9] 2353-9 (1995).

82. H.P. Kirchner, J.C. Conway Jr., and A.E. Segall, "Effect of joint thickness and residual stresses on the properties of ceramic adhesive joints: I. Finite element analysis of stress in joints," *J. Am. Ceram. Soc.*, **70** [2] 104-9 (1987).

83. S. Chikazumi, *Physics of ferromagnetism*, 2nd ed., Oxford University Press, New York, 1997.

84. W.H.von Aulock, *Handbook of microwave ferrite materials*, Academic Press, New York, 1965.

85. R.A. McCurrie, *Ferromagnetic materials: structure and properties*, Academic Press, London, 1994.

86. N. Spaldin, *Magnetic material: fundamentals and device applications*, University Press, Cambridge, 2003.

87. G. Winkler, *Crystallography, chemistry and technology of ferrites*; in: *Magnetic properties of Materials*, McGraw-Hill, New York, 1971.

88. H.W. Katz, *Solid state magnetic and dielectric devices*, John Wiley & Sons, 1959.

89. J.R. Claycomb, N. Tralshawala, L.M. Xie, J. Wosik, and J.H. Miller Jr., "Microwave study of $Nd_{0.7}Sr_{0.3}MnO_3$ thin film resistivity," *J. Appl. Phys.*, **85** 3749-52 (1999).

90. H. Inaba, T. Abe, Y. Kitano and J. Shimomura, "Magnetic properties and the grain boundary structure of Mn-Zn ferrites with the addition of Nb_2O_5," *J. Magn. Magn. Mater.*, **133** 487-9 (1994).

91. T. Inui, K. Konishi, and K. Oda, "Fabrications of broad-band RF-absorber composed of planar hexagonal ferrites," *IEEE T. Magn.*, **35** 3148-50 (1999).

92. M. Drofenik, A. Žnidaršič and I. Zajc, "Highly resistive grain boundaries in doped MnZn ferrites for high frequency power supplies," *J. Appl. Phys.*, **82** 333-40 (1997).

93. M. Sparks, *Ferromagnetic Relaxation Theory*, McGraw-Hill, 1964.

94. P. van der Zaag, J. Ruigrok, A. Noordermeer, M. van Delden, P. Por, M. Rekveldt, D. Donnet, and J. Chapman, "The initial permeability of polycrystalline MnZn ferrites: the influence of domain and microstructure," *J. Appl. Phys.*, **74** 4085-95 (1993).

95. H. Chen, P. DeGasperis, R. Marcelli, and M. Pardavi-Horvath, "Wide-band linewidth measurements in yttrium iron garnet films," *J. Appl. Phys.*, **67** 5530-32 (1990).

96. M. Sugimoto, "The past, present, and future of ferrites," *J. Am. Ceram. Soc.*, **82** [2] 269-80 (1999).

97. S. Kim, D. Han, and S. Cho, "Microwave absorbing properties of sintered Ni-Zn ferrite," *IEEE T. Magn.*, **30** 4554-6 (1994).

98. T. Nakamura and E. Hankui, "Control of high-frequency permeability in polycrystalline (Ba,Co)-Z-type hexagonal ferrite," *J. Magn. Magn. Mater.*, **257** 158-64 (2003).

99. R.F. Louh, T.G. Reynolds III and R.C. Buchanan, *Ceramic Materials for Electronics*, 3rd ed., Marcel Dekker, 2004.

100. E. Otsuki, S. Yamada, T. Otuska, K. Shoji, and T. Sato, "Microstructure and physical properties of manganese-zinc ferrites for high-frequency power supplies," *J. Appl. Phys.*, **69** 5942-4 (1991).

101. S.R. Janasi, D. Rodrigues, F.J.G. Landgraf, and M. Emura, "Magnetic properties of coprecipitated barium ferrite powders as a function of synthesis conditions," *IEEE T. Magn.*, **36** 3327-9 (2000).

102. V.V. Paike, P.S. Niphadkar, V.V. Bokade, and P.N. Joshi, "Synthesis of spinel $CoFe_2O_4$ via the co-precipitation method using tetraalkyl ammonium hydroxides as precipitating agents," *J. Am. Ceram. Soc.*, **90** [9] 3009-12 (2007).

103. C.K. Kim, J.H. Lee, S. Katoh, R. Murakami, and M. Yoshimura, "Synthesis of Co-, Co-Zn and Ni-Zn ferrite powders by the microwave-hydrothermal method," *Mater. Res. Bul.*, **36** [12] 2241-50 (2001).

104. J. Zhou, J. Ma, C. Sun, L. Xie, Z. Zhao, H. Tian, Y. Wang, J. Tao, and X. Zhu, "Low-temperature synthesis of $NiFe_2O_4$ by a hydrothermal method," *J. Am. Ceram. Soc.*, **88** [12] 3535-7 (2005).

105. C. Tsay, C. Liu, K. Liu, N. Lin, L. Huc, and T. Yeh, "Low temperature sintering of microwave magnetic garnet materials," *Mater. Chem. Phy.*, **79** 138-42 (2003).

106. S. Ounnunkad, P. Winotai, and S. Phanichphant, "Effect of La doping on structural, magnetic and microstructural properties of $Ba_{1-x}La_xFe_{12}O_{19}$ ceramics prepared by citrate combustion process," *J. Electroceram.*, **16** [4] 357-61 (2006).

107. S. Verma, S.D. Pradhan, R. Pasricha, S.R. Sainkar, and P.A. Joy, "A novel low-temperature synthesis of nanosized NiZn ferrite," *J. Am. Ceram. Soc.*, **88** [9] 2597-9 (2005).

108. R. Ramprasad, P. Zurcher, M. Petras, M. Miller, and P. Renaud, "Fundamental limits of soft magnetic particle composites for high frequency applications," *Phys. Stat. Sol. (b)*, **233** 31-8 (2002).

109. L. Li, G. Li, R.L. Smith Jr., and H. Inomata, "Microstructural evolution and magnetic properties of $NiFe_2O_4$ nanocrystals dispersed in amorphous silica," *Chem. Mater.*, **12** 3705-14 (2000).

110. X. Huang and Z. Chen, "A study of nanocrystalline $NiFe_2O_4$ in a silica matrix," *Mater. Res. Bull.*, **40** 105-13 (2005).

111. X. Liu, S. Fu, and C. Huang, "Magnetic properties of Ni ferrite nanocrystals dispersed in the silica matrix by sol-gel technique," *J. Magn. Magn. Mater.*, **281** 234-9 (2004).

112. N. Matsushita, C. Chong, T. Mizutani, and M. Abe, "Ni-Zn ferrite films with high permeability ($\mu' = \sim 30$, $\mu'' = \sim 30$) at 1 GHz prepared at 90ºC," *J. Appl. Phys.*, **91** 7376-8 (2002).

113. J. Bursik, P. Kosovan, and I. Subrt, "Thick Fe_2O_3, Fe_3O_4 films prepared by the chemical solution deposition method," *J. Sol-Gel Sci. Tech.*, **39** [2] 85-94 (2006).

114. T.G. Mathe, T. Moyo, and J.Z. Msomi, "Optical properties of $Zn_{0.5}(Ni, Co)_{0.5}Fe_2O_4$ mixed spinel ferrites thin films," *Phys. Stat. Sol. (c)*, **5** [2] 591-3 (2008).

115. Y.Y. Song, S. Kalarickal, and C.E. Patton, "Optimized pulsed laser deposited barium ferrite thin films with narrow ferromagnetic resonance linewidths," *J. Appl. Phys.*, **94** 5103-10 (2003).

116. A.M. Grishin, S.I. Khartsev, and S. Bonetti, "Low field driven latching-type $Bi_3Fe_5O_{12}/Gd_3Ga_5O_{12}$ magneto-optical display," *Appl. Phys. Lett.*, **88** [24] 242504/1-3 (2006).

117. C.R. Buhrer, "Faraday rotation and dichroism of bismuth calcium vanadium iron garnet," *J. Appl. Phys.*, **40** [11] 4500-2 (1969).

118. S.L. Morissette, J.A. Lewis, J. Cesarano III, D.B. Dimos, and T Baer, "Solid freeform fabrication of aqueous alumina–poly(vinyl alcohol) gelcasting suspensions," *J. Am. Ceram. Soc.*, **83** [10] 2409-16 (2000).

119. J.E. Smay, J. Cesarano, and J.A. Lewis, "Colloidal Inks for Directed Assembly of 3-D Periodic Structures," *Langmuir*, **18** [14] 5429-37 (2002).

120. J.E. Smay, G.M. Gratson, R.F. Shepherd, J Cesarano III, and J.A. Lewis, "Directed colloidal assembly of 3D periodic structures," *Adv. Mater.*, **14** [18] 1279-83 (2002).

121. S.S. Nadkarni and J.E. Smay, "Concentrated barium titanate colloidal gels prepared by bridging flocculation for use in solid freeform fabrication," *J. Am. Ceram. Soc.*, **89** [1] 96-103 (2006).

122. X. Zhao, J.R.G. Evans, and M.J. Edirisinghe, "Direct ink-jet printing of vertical walls", *J. Am. Ceram. Soc.*, **85** [8] 2113-25 (2002).

123. A. Ditsch, P.E. Laibinis, D.I.C. Wang, and T.A. Hatton, "Controlled clustering and enhanced stability of polymer-coated magnetic nanoparticles," *Langmuir*, **21** 600-18 (2005).

124. M. Lanttuada and T.A. Hatton, "Functionalization of monodisper magnetic nanoparticles," *Langmuir*, **23** 2158-68 (2007).

125. R.E. Mistler, *Tape casting, theory and practice*, the American Ceramic Society, Westerville, 2000. ISBN: 1-57498-029-7.

126. Y. Zeng, D. Jiang and P. Greil, "Tape casting of aqueous Al_2O_3 slurries," *J. Eur. Ceram. Soc.*, **20** 1691-7 (2000).

APPENDIX A

TAPE-CASTING OF α-AL_2O_3 AND TIO_2

The fabrication of α-Al_2O_3 or TiO_2 platelets includes tape casting [125], step-wise de-bindering and sintering. A water based recipe for a 200 g batch was adapted from [56,126] and listed in table A.1. The processing steps are as follows:

- dilute 3 ml dispersant with 30 g water in a 500 ml milling jar, and add 110 g of ceramic powders,
- fill ⅓ of the jar volume with cylindrical ZrO_2 milling media, followed by ball milling at 70 rpm for 24 hours,
- dissolve glycerin and PEG600 in 15 g water, followed by adding it into the mixture and ball milling for 1 hour,
- pre-dissolve PVA in 37 g water in an oil bath at 90ºC, followed by adding the cooled down solution into the mixture and ball milling at 20-30 rpm for 6 hours,
- at the end of ball-milling, add a defoaming agent DEFO215 (Ultra Adhesives) in an amount of ~0.1 wt% of the total slurry (this reduces the slurry viscosity and facilitates screening),
- filter the slurry through a 53 μm nylon mesh (Spectrum Inc.) to remove large bubbles and/or agglomerates,
- pour the slurry into the reservoir of the doctor blade container (Richard E. Mistler, Inc.), of which the blade gap is set to ~1.5 mm to obtain sheets with a sintered thickness of ~0.5 mm,
- adjust the casting speed (Model TTC-1000, Richard E. Mistler Inc.) to 30 cm/min to maintain a steady flow under the blade,

- dry the tape in open air at r.t for one day;
- remove the tape from the plastic carrier, trim off wavy edges and cut into proper shapes and sizes for sintering,
- apply a step-wise sintering program: 2ºC/min heating from r.t. to 100ºC, 0.2ºC/min from 100ºC to 400ºC, 2ºC/min from 400ºC to 1300ºC, 3 hours dwelling, and 2ºC/min cooling down to r.t.

	Material	**Conc. (wt%)**	**Actual amount**
Powder	TiO_2 or AKP30	55	110 g
Dispersant	1 wt% aqueous Aluminon solution, and aqueous $NH_3 \cdot H_2O$ (2M)	1.5	2 ml, and 1 ml
Solvent	Water	35	67 g
Binder	PVA, M.W. = 72,000	4	8 g
Plasticizer	Glycerin	4	8 g
Plasticizer	PEG 600	2	4 g
Defoamer	DEFO215	0.1	0.2 g

Table A.1: Tape casting recipe for an aqueous processing [56,126] and the actual amounts of dispersion components in a 200 g batch.

DISTRIBUTION LIST

Professor Hendrik Verweij

Professor Morgan Y. Liu

Professor Nitin Padture

Professor John L. Volakis

Professor Wolfgang Windl

Graduate School

The Ohio State University